

# Simulation of a phase-grating Moiré Interferometer for light and matter waves and its application to precision measurements

Roger Serrat i Guevara

June 2021

## Bachelor's Final Thesis

Submitted to the faculties of

Escola Tècnica Superior d'Enginyeria de Telecomunicació de  
Barcelona (ETSETB)  
Facultat d'Informàtica de Barcelona (FIB)

of

Universitat Politècnica de Catalunya - BarcelonaTech (UPC)

In partial fulfillment of the requirements for the

**Bachelor's Degree in Engineering Physics**  
and  
**Bachelor's Degree in Informatics Engineering**

Directed by

Dr. Dmitry Pushin, IQC  
Dr. Jordi Boronat Medico, UPC

[This page is intentionally left blank.]

## Abstract

Quantum mechanics describes matter behaviour by means of a wave function. This description allows for quantum particles to exhibit interference and diffraction effects similar to optical and other waves. These effects have been demonstrated with particles such as electrons, neutrons, atoms and even large molecules. Some interferometers have been designed employing phase gratings, like the phase-grating Mach-Zehnder interferometer, while others make use of absorption gratings, for instance to implement Talbot-Lau interferometers. Optical and matter wave interferometers are widely used in a variety of applications where precision and high resolution play important roles.

Recently a three phase-grating moiré neutron interferometer was demonstrated. Due to their neutral electric charge, neutrons are ideal probes of matter and their interactions. For example, the first demonstration of gravitational effects on a quantum particle was achieved using a perfect crystal interferometer in 1971. However, its very low neutron acceptance, and thus statistics, resulted in a relatively low precision. The larger area and wide range of wavelength acceptance of the phase-grating moiré interferometer makes precision measurements of gravity with neutrons possible. Nonetheless, such measurements require accurate methods of modeling and estimations of possible systematic errors.

In this thesis we present a numerical model based on scalar diffraction theory, and apply it to the simulation of the Talbot-Lau interferometer for visible light as well as the phase-grating moiré interferometer using both neutron and optical waves. This model describes well published experimental results. In addition, we verify it with optical experiments in the near-infrared region of the spectrum. Furthermore, the model can be adapted for further research of other interactions and studies of modern materials.

**Keywords:** Talbot effect, moiré effect, neutron interferometry, precision measurements, gravitational constant

## Resum

La mecànica quàntica descriu el comportament de la matèria mitjançant una funció d'ona. Aquesta descripció permet que les partícules quàntiques presentin efectes d'interferència i difració de manera similar a altres ones, com ara les ones òptiques. Aquests efectes s'han demostrat amb partícules com electrons, neutrons, àtoms i fins i tot molècules grans. S'han dissenyat alguns interferòmetres emprant xarxes de difracció de fase, com l'interferòmetre de Mach-Zehnder amb xarxes de fase, mentre que d'altres fan servir xarxes d'absorció, per exemple per implementar interferòmetres de Talbot-Lau. Tant els interferòmetres òptics com els d'ones de matèria són àmpliament utilitzats en diverses aplicacions on la precisió i l'alta resolució tenen un paper important.

Recentment un interferòmetre de moiré amb tres xarxes de fase ha estat demostrat per a neutrons. Degut a la seva càrrega elèctrica neutra, els neutrons són sondes ideals de la matèria i les seves interaccions. N'és un bon exemple el fet que la primera demostració d'efectes gravitacionals en una partícula quàntica es va realitzar utilitzant un interferòmetre de cristalls perfectes l'any 1971. Tanmateix, la seva escassa acceptació de neutrons, i per tant les seves baixes estadístiques, van resultar en una precisió relativament baixa. L'interferòmetre de moiré amb xarxes de fase ofereix una àrea més gran i accepta una gamma més àmplia de longituds d'ona, permetent així la realització de mesures de precisió de la gravetat mitjançant neutrons. No obstant, aquestes mesures requereixen mètodes precisos de modelatge i estimacions de possibles errors sistemàtica.

En aquesta tesi presentem un model numèric basat en la teoria escalar de la difracció, i l'apliquem a la simulació de l'interferòmetre de Talbot-Lau per a llum visible, així com a l'interferòmetre de moiré amb xarxes de fase utilitzant tant neutrons com ones òptiques. Aquest model descriu adequadament resultats experimentals publicats. També el verifiquem amb experiments òptics en la regió de l'espectre de l'infraroig proper. A més, el model pot ser adaptat per a futures investigacions d'altres interaccions i estudis de materials moderns.

**Paraules clau:** efecte Talbot, efecte moiré, interferometria de neutrons, mesures de precisió, constant gravitatòria

## Resumen

La mecánica cuántica describe el comportamiento de la materia mediante una función de onda. Esta descripción permite que las partículas cuánticas exhiban efectos de interferencia y difracción similares a los de ondas ópticas y otros tipos de ondas. Estos efectos se han demostrado con partículas como electrones, neutrones, átomos e incluso moléculas grandes. Se han diseñado algunos interferómetros empleando redes de difracción de fase, como el interferómetro de Mach-Zehnder con rejillas de fase, mientras que otros usan redes de absorción, por ejemplo, para implementar interferómetros de Talbot-Lau. Los interferómetros ópticos y de ondas de materia son ampliamente utilizados en diversas aplicaciones donde la precisión y la alta resolución juegan un papel importante.

Recientemente un interferómetro de moiré con tres rejillas de fase ha sido demostrado para neutrones. Debido a su carga eléctrica neutra, los neutrones son sondas ideales de la materia y sus interacciones. Un buen ejemplo es el hecho que la primera demostración de efectos gravitacionales en una partícula cuántica se logró utilizando un interferómetro de cristales perfectos en 1971. Sin embargo, su muy baja aceptación de neutrones, y por lo tanto sus bajas estadísticas, dieron como resultado una precisión relativamente baja. El interferómetro de moiré con tres rejillas de fase ofrece un área más grande y acepta un rango mas amplio de longitudes de onda, lo cual hace posible mediciones de precisión de la gravedad mediante neutrones. No obstante, tales mediciones requieren métodos precisos de modelado y estimaciones de posibles errores sistemáticos.

En esta tesis presentamos un modelo numérico basado en la teoría escalar de la difracción, y lo aplicamos a la simulación del interferómetro de Talbot-Lau para luz visible, así como al interferómetro de moiré con rejillas de fase utilizando tanto neutrones como ondas ópticas. El modelo describe adecuadamente resultados experimentales publicados. Asimismo, lo verificamos con experimentos ópticos en la región del espectro del infrarrojo cercano. Además, el modelo se puede adaptar para futuras investigaciones de otras interacciones y estudios de materiales modernos.

**Palabras clave:** efecto Talbot, efecto moiré, interferometría de neutrones, mediciones de precisión, constante gravitatoria

# Table of Contents

<b>List of Figures</b>	viii
<b>1 Introduction</b>	1
<b>2 Diffraction of optical waves</b>	3
2.1 Scalar diffraction formulas . . . . .	3
2.1.1 Angular Spectrum representation . . . . .	3
2.1.2 Rayleigh-Sommerfeld theory . . . . .	5
2.1.3 Fresnel diffraction . . . . .	6
2.1.4 Fraunhofer diffraction . . . . .	8
2.2 Sampling conditions . . . . .	8
2.2.1 Fresnel and Fraunhofer direct integration . . . . .	9
2.2.2 Fresnel convolution . . . . .	9
2.2.3 Rayleigh-Sommerfeld . . . . .	10
2.2.4 Angular Spectrum . . . . .	11
2.3 Methods to increase accuracy . . . . .	12
2.3.1 Zero-padding . . . . .	12
2.3.2 Simpson's rule . . . . .	13
2.3.3 Band-limited Angular Spectrum . . . . .	14
2.4 Simulation test: diffraction from a slit . . . . .	17
<b>3 Self-imaging effects for amplitude and phase gratings</b>	22
3.1 Talbot effect . . . . .	22
3.1.1 Theoretical development . . . . .	23
3.1.2 Amplitude gratings . . . . .	25
3.1.3 Phase gratings . . . . .	28
3.1.4 Lau effect . . . . .	32
3.2 Near and far-field diffraction of a Gaussian beam . . . . .	34
3.2.1 Theoretical description of self-images . . . . .	34
3.2.2 Simulation results . . . . .	36
3.3 Cone beam and experimental images . . . . .	38
<b>4 Optical wave interferometry</b>	42
4.1 Talbot interferometer . . . . .	42
4.2 Two phase-grating moiré interferometer . . . . .	47
4.2.1 Theoretical description . . . . .	48
4.2.2 Experimental and simulation results . . . . .	49
4.3 Three phase-grating moiré interferometer . . . . .	54

<b>5 Neutron matter waves</b>	<b>57</b>
5.1 Free-space propagation . . . . .	57
5.2 Quantum phase . . . . .	60
5.3 Sampling conditions . . . . .	61
5.4 Phase-grating moiré interferometer . . . . .	65
5.4.1 Two phase-grating interferometer . . . . .	65
5.4.2 Three phase-grating interferometer . . . . .	67
5.5 Gravitational potential . . . . .	70
<b>6 Conclusion</b>	<b>74</b>
<b>Appendices</b>	<b>76</b>
<b>A Diffraction of a Gaussian beam from a periodic object</b>	<b>77</b>
A.1 Fresnel integral . . . . .	78
A.1.1 Integral solution . . . . .	78
A.1.2 Intermediate relations . . . . .	80
A.2 Localization and magnification of images . . . . .	82
A.2.1 Object placed at beam waist . . . . .	82
A.2.2 Spherical wavefront illumination . . . . .	83
A.2.3 Plane-wave illumination . . . . .	83
A.3 Beam expression in 1D . . . . .	83
<b>B Contrast calculation</b>	<b>86</b>
<b>C Theoretical considerations of the moiré interferometer</b>	<b>88</b>
C.1 Two-grating system . . . . .	89
C.1.1 Field at the observation plane . . . . .	89
C.1.2 moiré fringes . . . . .	94
C.2 Three-grating system . . . . .	97
<b>D Schrödinger Equation for a linear potential</b>	<b>101</b>
<b>References</b>	<b>104</b>

# List of Figures

2.1	Model for the minimum bandwidth required for exact calculation of field propagation . . . . .	16
2.2	Fresnel diffraction pattern from a slit . . . . .	18
2.3	Diffraction pattern from a slit using the Angular Spectrum method .	19
2.4	Diffraction pattern from a slit using the band-limited Angular Spectrum method . . . . .	20
2.5	Diffraction pattern from a slit using the band-limited Angular Spectrum method with zero-padding . . . . .	20
3.1	Analytic Talbot carpet after a binary amplitude grating with a 50 % duty cycle . . . . .	25
3.2	Analytic Talbot carpet after a binary amplitude grating with a 10 % duty cycle . . . . .	26
3.3	Analytic Talbot self-image from a binary amplitude grating . . . . .	26
3.4	Talbot carpet after a binary amplitude grating with 10 % duty cycle, using the AS method . . . . .	27
3.5	Talbot self-image from a binary amplitude grating, simulated with the AS method . . . . .	28
3.6	Theoretical Talbot carpet after a $\pi/2$ -phase grating with 50 % duty cycle . . . . .	29
3.7	Lohmann image from a $\pi/2$ -phase grating with duty cycle 0.5 . . . . .	30
3.8	Theoretical Talbot carpet after a $\pi$ -phase grating with 50 % duty cycle .	30
3.9	Lohmann image from a $\pi$ -phase grating with duty cycle 0.5 . . . . .	31
3.10	Theoretical Talbot carpet after a $\pi$ -phase grating with duty cycle 0.25	31
3.11	Lohmann image from a $\pi$ -phase grating with duty cycle 0.25 . . . . .	32
3.12	Analytic self-image in the Lau configuration . . . . .	33
3.13	Intensity pattern at fractional Talbot distances in the Lau configuration	33
3.14	Lau carpet behind two amplitude gratings with duty cycle 0.1 . . . . .	34
3.15	Self-image of an amplitude grating under Gaussian beam illumination .	37
3.16	Far-field pattern from a Gaussian beam incident on a binary amplitude grating . . . . .	38
3.17	Full carpet after a phase grating under Gaussian beam illumination .	39
3.18	Carpet after a phase grating illuminated with a divergent Gaussian beam . . . . .	40
3.19	Experimental and 2D simulated images after a $\pi/2$ -phase grating illuminated by a cone beam . . . . .	41
4.1	Amplitude and duty cycle of the Talbot interferometer pattern for a linear-phase object . . . . .	44

4.2	Intensity pattern after the Talbot interferometer for a linear-phase object . . . . .	45
4.3	Phase of the object under test for the Talbot interferometer imaging system . . . . .	46
4.4	Intensity pattern at the focal plane of the lens in the Talbot interferometer imaging system . . . . .	46
4.5	Image of the object under test obtained with the Talbot interferometer imaging system . . . . .	47
4.6	Carpet after the second grating in the 2PGMI . . . . .	50
4.7	Experimental and 2D simulated after the 2PGMI . . . . .	51
4.8	Contrast and frequency of the moiré fringes in the 2PGMI for a coherent beam . . . . .	52
4.9	Spectrum used for the simulation of the 2PGMI for an incoherent beam	53
4.10	Contrast and frequency of the moiré fringes in the 2PGMI for an incoherent beam . . . . .	54
5.1	Contrast and frequency results for the neutron 2PGMI with a monochromatic beam . . . . .	66
5.2	Contrast and frequency results for the neutron 3PGMI with a monochromatic source . . . . .	68
5.3	Contrast and frequency results for the neutron 3PGMI with a polychromatic source following a Maxwell distribution . . . . .	69
5.4	Schematic of the paths inside the 3PGMI . . . . .	72
5.5	Phase of the pattern from the neutron 3PGMI with a gravitational potential as a function of the interferometer rotation . . . . .	73

# Chapter 1

## Introduction

Interferometers based on particle self-interference constitute remarkably sensitive devices for precision measurements [1, 2]. In this regard, neutrons constitute an ideal probe of matter interactions due to their neutral electric charge, large mass and wavelengths below the nanometer scale.

The first neutron interferometer was built by means of two prisms that caused Fresnel interference by means of wave front division [3]. With this device a path separation of only 60  $\mu\text{m}$  was obtained, which was later improved to a few centimeters with a perfect crystal Mach-Zehnder interferometer relying on Bragg diffraction [4]. This design allowed for a great number of investigations focusing on the neutron properties and interactions [5–10], but at the same time suffered some important drawbacks, including a low wavelength acceptance and the difficulty of fabrication [11–15].

Some of these challenges were overcome thanks to the advances in microfabrication of periodic structures, which allowed the demonstration of a Mach-Zehnder neutron interferometer employing reflection gratings [16] and, later, a three phase-grating Mach-Zehnder interferometer for cold neutrons [17–20]. Still, in many applications this interferometers were limited by the low intensities of cold neutrons and the need for a high degree of collimation.

As an alternative, the so-called Talbot-Lau interferometer was developed using both phase and amplitude gratings. According to the near-field Talbot effect [21], a self-image of a phase grating is generated, that is sensitive to the phase gradient of a sample placed in front of it. Such interferometer was first proposed for cold potassium ions and x-rays [22] and later implemented for neutrons [23]. However, the increase in the neutron flux due to the wider chromatic acceptance was effectively countered by the hard to manufacture absorption gratings. Moreover, a wider spectrum also caused the contrast of the images to be diminished.

Finally, a phase-grating interferometer based on the universal moiré effect was recently presented [24] and demonstrated for neutrons [25, 26]. This design eliminates the need for absorption gratings, and allows for a broader wavelength acceptance and a higher transmitted intensity. Moreover, it reduces significantly the alignment requirements with respect to the perfect crystal interferometer.

The goal of this thesis is to develop a numerical model capable of simulating optical systems that rely on diffraction effects, both with light and matter waves. In

particular, we will focus on the phase-grating moiré interferometer and, ultimately, on its implementation with neutrons. This model is required in order to correctly understand the systematics of the devices used for precision measurements before the introduction of experimental uncertainties.

For that purpose, this document is organized as follows. In Chapter 2 the numerical model based on the scalar theory of optical diffraction is presented. In Chapter 3 the self-imaging effects of amplitude and phase gratings are first introduced for plane wave illumination, and afterwards described for the more general case of a Gaussian beam. In Chapter 4 a couple of optical grating-based interferometer designs are studied, namely the Talbot interferometer as well as the two phase-grating and three phase-grating moiré interferometers. In Chapter 5 the model is extended to work with neutron matter waves and applied to the neutron moiré interferometer. Finally, in Chapter 6 some concluding remarks are discussed.

# Chapter 2

## Diffractionn of optical waves

Diffractionn is the effect that waves undergo when passing through an obstacle. In the regime that will be considered throughout this thesis, when the characteristic sizes of the objects and the distances between them are much larger than the wavelengths of the waves, it is accurately described by the classical diffraction theory. More specifically, its scalar approximation, which does not take into account the polarization of the field, is enough to predict outcome of the systems in question.

The aim of this chapter is to present the main formulas that are used to model diffractionn of optical waves, as well as to provide detail on the limits of the numerical methods used to calculate them. This formulas will be studied for the general case of a two-dimensional field propagating (by convention) in the  $z$  direction. Usually, the conversion to one dimension is trivial and differs only in a complex constant. If that were not the case, the 1D case will be explicitly considered.

### 2.1 Scalar diffraction formulas

There are several equivalent descriptions for scalar diffraction, depending on how they approach the solution to the wave equation that is derived from the fundamental Maxwell's equations. This section is not meant to be a full description of the scalar diffraction theory, but rather to provide a brief derivation of the main results that are obtained from it. A more detailed explanation can be found in ref. [27].

#### 2.1.1 Angular Spectrum representation

As a starting point, consider a medium that is homogeneous, isotropic, linear and source-free. Under these conditions, Maxwell's equations are reduced to the well-known Helmholtz equation:

$$\nabla^2 \mathbf{U}(\mathbf{r}, t) + k^2 \mathbf{U}(\mathbf{r}, t) = 0 \quad (2.1)$$

Usually  $\mathbf{U}$  is taken to be the electric field, although the equation is also valid for the magnetic field. In the scalar approximation, the electromagnetic wave is represented by

$$\mathbf{U}(\mathbf{r}, t) = \hat{e} U(x, y, z) e^{-i\omega t} \quad (2.2)$$

Therefore, the scalar field  $U(x, y, z)$  must satisfy the Helmholtz equation itself. The problem is to find a solution when the boundary condition  $U(x, y, 0)$  is known. Following the derivation proposed in ref. [28], a possible approach relies on the fact that the field can be written as a superposition of plane waves:

$$U(x, y, z) = \int_{-\infty}^{\infty} \tilde{U}(\mathbf{k}) e^{i\mathbf{k}\cdot\mathbf{r}} d\mathbf{k} \quad (2.3)$$

where the wave vector  $\mathbf{k}$  is defined as  $\mathbf{k} = (2\pi/\lambda)\hat{e}_k$ .

This constitutes the basis of the Angular Spectrum (AS) theory. Each term in the expression above denotes a plane wave with an amplitude given by  $\tilde{U}(\mathbf{k})$  in the direction  $\hat{e}_k = \cos \alpha \hat{i} + \cos \beta \hat{j} + \cos \gamma \hat{k}$ , where  $\alpha$ ,  $\beta$  and  $\gamma$  denote the angles formed between  $\mathbf{k}$  and the unit basis vectors  $\hat{i}$ ,  $\hat{j}$  and  $\hat{k}$ , respectively. The expression can be simplified by defining the so-called spatial frequencies:

$$u = \frac{\cos \alpha}{\lambda}; \quad v = \frac{\cos \beta}{\lambda}; \quad m = \frac{\cos \gamma}{\lambda} \quad (2.4)$$

Then, the field can be written as:

$$U(x, y, z) = \iiint \tilde{U}(u, v, m) e^{i2\pi(ux+vy+mz)} du dv dm \quad (2.5)$$

Plugging this expression into the Helmholtz equation results in the following condition that the spatial frequencies must satisfy:

$$\frac{1}{\lambda^2} = u^2 + v^2 + m^2 \quad (2.6)$$

Using this fact, one can reduce the expression of the field to just two integrals:

$$U(x, y, z) = \iint \tilde{U}(u, v) e^{i2\pi(ux+vy+mz)} du dv \quad (2.7)$$

with

$$m(u, v) = \begin{cases} \sqrt{\frac{1}{\lambda^2} - u^2 - v^2} & \text{if } \frac{1}{\lambda^2} > u^2 + v^2 \\ i\sqrt{u^2 + v^2 - \frac{1}{\lambda^2}} & \text{if } \frac{1}{\lambda^2} < u^2 + v^2 \end{cases} \quad (2.8)$$

The condition given by equation 2.6 defines a sphere in frequency space, which is seen on the  $uv$  plane as a disk limited by  $u^2 + v^2 = 1/\lambda^2$ . Spatial frequencies  $(u, v)$  that fall inside the disk, meaning that  $m$  is real, denote propagating waves. On the other hand, frequencies outside of it ( $m$  imaginary) cause evanescent waves, representing a loss of resolution of the original field during free-space propagation. By convention, only the positive square root for  $m$  is considered, because it represents

a wave travelling to positive values of  $z$ . The negative square root would denote waves travelling to the opposite direction, and the complete solution is in fact a superposition of the two.

Applying the boundary condition at  $z = 0$  to equation 2.7:

$$U(x, y, 0) = \iint \tilde{U}(u, v) e^{i2\pi(ux+vy)} dudv \quad (2.9)$$

or, equivalently,

$$\tilde{U}(u, v; 0) \equiv \tilde{U}(u, v) = \iint U(x, y, 0) e^{-i2\pi(ux+vy)} dxdy \quad (2.10)$$

The expression above can be clearly identified as the Fourier Transform of the initial field in the transverse plane. A slight change in notation has been conveniently introduced to relate the amplitudes in frequency space to the plane  $z$  to which they correspond. Analogously, the field at a distance  $z$  can also be written as a 2D (inverse) Fourier Transform:

$$U(x, y, z) = \iint \tilde{U}(u, v; z) e^{i2\pi(ux+vy)} dudv \quad (2.11)$$

Matching this expression with equation 2.7 one finds the Angular Spectrum diffraction formula in frequency space:

$$\tilde{U}(u, v; z) = \tilde{U}(u, v; 0) e^{i2\pi mz} \quad (2.12)$$

This expression shows that the field's frequency components at an arbitrary plane are related to the initial field components by the transfer function  $H = \exp(i2\pi mz)$ . The same formula translates into regular space coordinates as the convolution of the initial field with an impulse response that is obtained from the Fourier Transform of the transfer function:

$$h(x, y, z) = \iint e^{i2\pi mz} e^{i2\pi(ux+vy)} dxdy \quad (2.13)$$

### 2.1.2 Rayleigh-Sommerfeld theory

The Huygens-Fresnel principle states that each point of an optical wave front acts as a secondary source of spherical wave fronts of the same frequency (wavelet). Therefore, the field at any point after the wave front will be the result of the superposition of all previous wavelets. From this idea a general theory was developed by Kirchhoff, Rayleigh and Sommerfeld [27] by means of Green's theorem. Its main result gives the optical disturbance at a given point in space caused by the optical distribution at a previous plane, namely the Rayleigh-Sommerfeld (RS) diffraction formula.

It can be shown that both the AS (superposition of plane waves) and RS (superposition of spherical waves) approaches are equivalent. For instance, one can find the RS impulse response by taking the inverse Fourier Transform of the AS transfer

function [29]. An alternative derivation [30] can be performed using Weyl's identity [31], which accounts for the angular spectrum representation of an outgoing spherical wave:

$$\frac{\exp(ikr)}{r} = -\frac{i}{m} \iint e^{i2\pi(ux+vy+mz)} dudv \quad (2.14)$$

Differentiating both sides with respect to  $z$ :

$$\frac{\partial}{\partial z} \left[ \frac{\exp(ikr)}{r} \right] = -2\pi \iint e^{i2\pi(ux+vy+mz)} dudv \quad (2.15)$$

Notice that the right-hand side of this expression corresponds to  $-2\pi h(x, y, z)$ , being  $h(x, y, z)$  the impulse response of the angular spectrum formula (eq. 2.13). Therefore,

$$h(x, y, z) = -\frac{1}{2\pi} \frac{\partial}{\partial z} \left( \frac{\exp(ikr)}{r} \right) = -\frac{1}{2\pi} \frac{\partial}{\partial z} \left[ \frac{\exp(ikr)}{r} \right] \frac{\partial r}{\partial z} \quad (2.16)$$

with  $r = \sqrt{x^2 + y^2 + z^2}$ . Performing the derivatives, one obtains the impulse response in the RS framework:

$$h(x, y, z) = -\frac{1}{2\pi} \left[ ik - \frac{1}{r} \right] \frac{z}{r} \frac{e^{ikr}}{r} \quad (2.17)$$

where  $r = \sqrt{x^2 + y^2 + z^2}$ . Defining  $R = \sqrt{(x - x')^2 + (y - y')^2 + z^2}$  and assuming that  $R \gg \lambda$ , so  $[ik - 1/R] \approx ik$ , the Rayleigh-Sommerfeld formula is found:

$$U(x, y, z) = \frac{1}{i\lambda} \iint U(x', y', 0) \frac{z}{R} \cdot \frac{e^{ikR}}{R} dx' dy' \quad (2.18)$$

For the 1D case, the impulse response takes the following form [29]:

$$h(x, z) = \frac{ikz}{2r} H_1^{(1)}(kr) \quad (2.19)$$

where  $H_1^{(1)}$  is the first-kind first-order Hankel function and  $r = \sqrt{x^2 + z^2}$ .

### 2.1.3 Fresnel diffraction

The formulae given above can be simplified under some specific assumptions leading to Fresnel's and Fraunhofer's diffraction formulas, which are presented in this section and the next.

Consider the diffraction from a finite aperture or slit, of characteristic size  $\Sigma$ , illuminated by monochromatic light. In the thin mask approximation, transmission from the aperture, placed at  $z = 0$ , is given by

$$U(x', y', 0) = U_{inc}(x', y', 0) \cdot t(x', y') \quad (2.20)$$

where  $U_{inc}$  denotes the field incident on the aperture and  $t(x', y')$  is its transmission function.

The Fresnel approximation consists in considering only effects in the paraxial region, where the following conditions hold:

1. The observation plane is placed at distances  $z > \Sigma$
2. The observation region of interest in the plane  $z$  is close to the origin ( $x = 0$ ;  $y = 0$ )

Under these conditions,  $R$  is expanded as:

$$R = z \sqrt{1 + \frac{(x - x')^2 + (y - y')^2}{z^2}} \approx z \left( 1 + \frac{1}{2} \frac{(x - x')^2 + (y - y')^2}{z^2} + \dots \right) \quad (2.21)$$

It is sufficient to take the expansion up to first order for distances and up to second order for phase terms. Then, equation 2.18 becomes Fresnel's diffraction formula:

$$U(x, y, z) = \frac{e^{ikz}}{i\lambda z} \iint U(x', y', 0) e^{i\frac{k}{2z}[(x-x')^2+(y-y')^2]} dx' dy' \quad (2.22)$$

This integral can be performed in multiple ways [32]. First, expanding the quadratic phase term it becomes:

$$U(x, y, z) = \frac{e^{ikz}}{i\lambda z} e^{i\frac{k}{2z}(x^2+y^2)} \iint U(x', y', 0) e^{i\frac{k}{2z}(x'^2+y'^2)} e^{-i\frac{2\pi}{\lambda z}(xx'+yy')} dx' dy' \quad (2.23)$$

The expression above takes the form of a Fourier Transform of the field with a quadratic phase, where the spatial coordinates are given by  $u = x/\lambda z$  and  $v = y/\lambda z$ . Therefore, the integral can be directly solved by means of a single transform and an appropriate change of coordinates.

Second, notice that equation 2.22 is essentially a convolution, and thus can be written as such:

$$U(x, y, z) = U(x', y', 0) \otimes \left[ \frac{e^{ikz}}{i\lambda z} e^{i\frac{k}{2z}(x'^2+y'^2)} \right] \quad (2.24)$$

Using the convolution theorem, this formula can be transformed into the frequency domain. The impulse response has an analytical Fourier Transform, resulting in an equation analogous to the Angular Spectrum formula:

$$\tilde{U}(u, v; z) = \tilde{U}(u, v; 0) e^{ikz} e^{-i\pi\lambda z(u^2+v^2)} \quad (2.25)$$

### 2.1.4 Fraunhofer diffraction

Fresnel's formula can be simplified even further if the observation plane is located in the far field from the aperture, or Fraunhofer region, where an additional condition is imposed:

$$z \gg \frac{k(x'^2 + y'^2)_{max}}{2} \quad (2.26)$$

Here,  $(x'^2 + y'^2)_{max}$  refers to the maximum extension of the initial field distribution in the  $z = 0$  plane. In this region,  $\exp[ik(x'^2 + y'^2)/2z] \approx 1$  and equation 2.23 is reduced to Fraunhofer's diffraction formula:

$$U(x, y, z) = \frac{e^{i\left(kz + \frac{k(x^2 + y^2)}{2z}\right)}}{i\lambda z} \tilde{U}(u, v; 0) \Big|_{u=\frac{x}{\lambda z}, v=\frac{y}{\lambda z}} \quad (2.27)$$

## 2.2 Sampling conditions

Due to the nature of computers, numerical calculations of the formulas presented previously requires for them to be discretized, along with the fields under study. Since the equations are originally continuous, errors might appear if this process is not performed carefully. For this reason, in this section the limits for proper calculation of the proposed methods are explored, starting with the simpler formulas, namely Fraunhofer and Fresnel, and extending the results to the more general ones.

The analysis of the sampling requirements is based on the Nyquist theorem [33]. For simplicity, consider first the one-dimensional Fresnel formula. Assuming that the initial field  $U_0(x)$  has a finite extent  $\Delta x_0$  and that its frequency content is negligible outside a band of extension  $\Delta u_0$  (that is, its maximum frequency is  $\Delta u_0/2$ ), a good sampling requires that the sampling period at the observation plane  $\delta_2$  fulfills

$$\delta_2 \leq \frac{1}{\Delta u_{z,max}} \equiv \frac{1}{\Delta u_0} \quad (2.28)$$

where it has been used that the frequency extent of the output signal  $\Delta u_z$  remains invariant while the pattern propagates. On another note, the physical extension of diffracted pattern enlarges with the distance:

$$\Delta x_z = \Delta x_0 + \lambda z \Delta u_0 \quad (2.29)$$

Therefore, an accurate evaluation of a propagated pattern requires an increasing number of sampling points  $N$  at the output plane.

As a side note, in the previous chapter it was seen that all the diffraction formulas are related to the Fourier Transform, either directly or as a way to calculate convolutions. For our purposes, the discrete Fourier Transforms (DFT) will be calculated with the Fast-Fourier Transform (FFT) algorithm. For this reason these two terms will be used as equivalent, even though fundamentally they are not.

### 2.2.1 Fresnel and Fraunhofer direct integration

Both the Fresnel and Fraunhofer formulas can be calculated by means of a single FFT, thus being the fastest methods presented here. However, the change of coordinates of the Fourier Transform implies a change in the spacing of the sampling points [32]:

$$\delta_2 = \frac{\lambda z}{N\delta_1} \quad (2.30)$$

where  $\delta_1$  and  $\delta_2$  are the sampling intervals at the source and observation planes, respectively. Therefore, the sampling period will inevitably increase with distance.

In the case of the Fresnel formula, assuming that the field right after the object  $U_0(x)$  has frequencies smaller than those in the quadratic phase factors, the main problem comes from an adequate sampling of the exponential functions. Considering the Nyquist limit, the range of distances that allow proper sampling is [33]:

$$z \geq \frac{\Delta x_0^2}{\lambda N} \quad (2.31)$$

This condition does not strictly apply to the Fraunhofer formula, but it is also limited to large distances by its own requirements. On the other hand, similar argument can be applied to the global phase factor, whose sampling condition is:

$$z \leq \frac{\Delta x_0^2}{\lambda N} \quad (2.32)$$

A good sampling is accomplished only if the equality is assumed in both conditions. For large  $z$ , this algorithm provides the whole extent of the final diffraction pattern, but this result is only compatible with the first condition. Diffraction patterns present rapid variations in phase that lead to strong aliasing effects, but generally the intensity profiles have soft variations. Consequently, this method is valid just for far-field amplitude evaluation.

### 2.2.2 Fresnel convolution

As it has already been said, the Fresnel integral can be written as a convolution of the field and a certain function. One can use the convolution theorem to perform the calculation:

$$U(x, y) = \mathcal{F}^{-1} \{ \mathcal{F} \{ U(x', y') \} H_F(u, v) \} \quad (2.33)$$

where, as stated previously,  $H_F$  can either be calculated from the function in the spatial domain as

$$H_F(u, v) = \mathcal{F} \left\{ \frac{e^{ikz}}{i\lambda z} e^{\frac{ik}{2z}(x^2+y^2)} \right\} \quad (2.34)$$

or it can be written directly in frequency coordinates:

$$H_F(u, v) = e^{ikz[1 - \frac{\lambda^2}{2}(u^2 + v^2)]} \quad (2.35)$$

In order to find the sampling limit, it must be noted that neither function has a limited bandwidth, and therefore it is impossible to make the calculation meet the Nyquist sampling theorem even if the object function is band-limited. However, the FFT calculation is thought to meet the Nyquist requirement approximately if there are at least two sampling points in the value region where the function once changes a  $2\pi$  period [34].

In spatial domain, the largest phase-change rate occurs when  $x, y = L/2$ , where  $L$  is the width of the field. Then, the sampling condition is given by

$$\left| \frac{\partial}{\partial x} \frac{\pi}{\lambda z} (x^2 + y^2) \right|_{x,y=\frac{L}{2}} \times \delta_x \leq \pi \Rightarrow \delta_x \leq \frac{\lambda z}{L} \quad (2.36)$$

In frequency domain, the discrete form of equation 2.35 can be written as

$$H_F(m\delta_u, n\delta_v) = e^{ikz[1 - \frac{\lambda^2}{2}((m\delta_u)^2 + (n\delta_v)^2)]} \quad (2.37)$$

where  $m, n = -N/2, -N/2 + 1, \dots, N/2 - 1$ . Its largest phase-change rate happens when  $m, n = \pm N/2$ , so the sampling requirement can be found with

$$\left| \frac{\partial}{\partial m} \frac{2\pi}{\lambda} z \left[ 1 - \frac{\lambda^2}{2} ((m\delta_u)^2 + (n\delta_v)^2) \right] \right|_{m,n=N/2} \leq \pi \quad (2.38)$$

which leads, applying that  $\delta_u = 1/L$  and  $L = \delta_x N$ , to the following condition:

$$\delta_x \geq \sqrt{\frac{\lambda z}{N}} \quad (2.39)$$

Notice that this condition is exactly opposite to the previous one (eq. 2.36). This last condition might seem easier to satisfy, but one must keep in mind that the sampling interval cannot be extended infinitely, since sampling of the object function still has to fulfill the requirements in regular space.

### 2.2.3 Rayleigh-Sommerfeld

The procedure explained in the previous section can also be applied to the Rayleigh-Sommerfeld formula. By means of the convolution theorem, equation 2.18 can be written as follows:

$$U(x, y) = \mathcal{F}^{-1} \{ \mathcal{F} \{ U(x', y') \} H_R(u, v) \} \quad (2.40)$$

where the transfer function  $H_R$  is calculated from the RS impulse response:

$$H_R(u, v) = \mathcal{F} \left\{ z \frac{e^{ik\sqrt{z^2 + x^2 + y^2}}}{i\lambda(z^2 + x^2 + y^2)} \right\} \quad (2.41)$$

Since the spatial change rate of the exponential term is much higher than the other terms, only its phase needs to be considered. Following the same reasoning as for the Fresnel method in the spatial domain, the sampling requirement is found to be

$$\delta_x \leq \frac{\lambda \sqrt{z^2 + \frac{L^2}{2}}}{L} \quad (2.42)$$

An alternative approach [29] suggests that the oscillation period of the impulse response can be estimated by calculating the interval  $\Delta\rho$  between points on the observation plane with a  $2\pi$  phase difference:

$$k\sqrt{(\rho + \Delta\rho)^2 + z^2} - k\sqrt{\rho^2 + z^2} = 2\pi \quad (2.43)$$

where  $\rho = \sqrt{x^2 + y^2}$  is the offset of a point from the optical axis. Isolating the interval  $\Delta\rho$  in the equation above:

$$\Delta\rho = \sqrt{\lambda^2 + \rho^2 + 2\lambda\sqrt{\rho^2 + z^2}} - \rho \quad (2.44)$$

For a light diffraction problem to be solved properly, the minimum propagation distance  $z_{min}$  and the maximum offset from the optical axis  $\rho_{max}$  can be substituted into this equation to yield a minimum  $\Delta\rho_{min}$ . The sampling intervals on the  $xy$  plane should be less than  $\Delta\rho_{min}/2$  in order to reduce aliasing errors.

## 2.2.4 Angular Spectrum

Recall the AS formula in the frequency domain (eq. 2.25). Applying the inverse Fourier Transform to both sides, this equation now returns the field in spatial coordinates:

$$U(x, y) = \mathcal{F}^{-1} \{ \mathcal{F} \{ U(x', y') \} H_B(u, v) \} \quad (2.45)$$

with  $H_B$  the AS transfer function:

$$H_B(u, v) = e^{ikz\sqrt{1-(\lambda u)^2-(\lambda v)^2}} \quad (2.46)$$

Considering an object plane width of  $L$  and a grid size  $N \times N$ , the discretization of this formula is given by [34]:

$$U(p\delta_x, q\delta_y) = IFFT \left\{ FFT \{ U(r\delta_x, s\delta_y) \} e^{ikz\sqrt{1-(\lambda m\delta_u)^2-(\lambda n\delta_v)^2}} \right\} \quad (2.47)$$

where  $p, q, r, s, m, n = -N/2, -N/2+1, \dots, N/2-1$ . Similarly to the Fresnel formula in frequency space, the sampling condition of the transfer function is obtained with:

$$\left| \frac{\partial}{\partial m} kz\sqrt{1 - (\lambda m\delta_u)^2 - (\lambda n\delta_v)^2} \right|_{m,n=N/2} \leq \pi \quad (2.48)$$

Since  $\delta_u = \delta_v = 1/L$  and  $k = 2\pi/\lambda$ , the resulting sampling condition is

$$\frac{\lambda z N}{L \sqrt{L^2 - 2 \left(\frac{\lambda N}{2}\right)^2}} \leq 1 \quad (2.49)$$

Notice that in the case when  $L^2 \gg 2(\lambda N/2)^2$  this condition becomes

$$L \geq \sqrt{N \lambda z} \Rightarrow \delta_x \geq \sqrt{\frac{\lambda z}{N}} \quad (2.50)$$

which is the same result that was obtained for Fresnel diffraction.

## 2.3 Methods to increase accuracy

Sampling is not the only issue that one encounters when trying to calculate diffraction patterns numerically. In this section we present some techniques that allow to reduce numerical errors and increase the accuracy of the aforementioned methods. For simplicity, all the algorithms will be shown for one-dimensional calculations. Their extension to the two-dimensional case is straightforward, although some comments on it are added when necessary.

### 2.3.1 Zero-padding

The convolution calculation for 1D diffraction can be performed with the FFT as follows [35]:

$$S = IFFT[FFT(U) \cdot \times FFT(H)] \cdot \delta_x \quad (2.51)$$

where  $\cdot \times$  denotes element-by-element multiplication. The  $\delta_x$  factor comes from the fact that the FFT algorithm requires the result to be multiplied by the sampling interval in order for it to have the same magnitude as one would expect from the continuous Fourier Transform. This is not done in most FFT implementations. Furthermore, the IFFT would need to be normalized with  $\delta_u = 1/(\delta_x N)$ , but most implementations already apply the  $1/N$  factor by default.

Since, by construction, the FFT assumes that the underlying sequence is periodic, direct application of the formula above results in a circular (or periodic) convolution of  $U$  and  $H$ , while a linear convolution is needed. This causes aliasing effects to appear at the edges of the computation window. The solution to this problem is simply to zero-pad the input field [29], that is, to add zeros at the end to make its total size  $2N - 1$ . Additionally, the computational domain must be doubled. Then, the modified  $U$  and  $H$  arrays are:

$$U = [U(x'_1, 0) \ U(x'_2, 0) \ \dots \ U(x'_N, 0) \ 0 \ \dots \ 0]_{2N-1} \quad (2.52)$$

$$H = [h(\xi_1) \ \dots \ h(\xi_{2N-1})]_{2N-1} \quad (2.53)$$

being  $h(\xi_j)$  the impulse response (in our case, either Fresnel or RS) evaluated at

$$\xi_j = \begin{cases} x_1 - x'_{N+1-j} : j = 1, \dots, N-1 \\ x_{j-N+1} - x'_1 : j = N, \dots, 2N-1 \end{cases} \quad (2.54)$$

Finally, the desired output field is then given by  $S(N : 2N-1)$ , which corresponds to the right half of the output array.

The issue explained here also occurs when the transfer function is directly given in the frequency domain. In that case, the field must be zero-padded in the same way, while the transfer function has to be evaluated at the proper frequencies, which are obtained by keeping the maximum frequency the same and dividing in half the sampling interval (thus doubling the total number of points). No normalization factor should be applied since the one from the single FFT cancels out with that of the inverse transform. Also, the output field might be in the left half of  $S$  instead of the right one, depending on how this process is implemented.

Regarding two-dimensional convolution, both coordinates should be extended in the same way, therefore multiplying by four the matrix size. The normalization factor, if needed, becomes  $\delta_x\delta_y$ , and the output field is found either in the top-left or bottom-right corner.

### 2.3.2 Simpson's rule

Another consequence of using equation 2.51 for the calculation of the convolution, no matter if zero-padding is used, is that it is essentially equivalent as using the trapezoid rule for numerical integration. Therefore, the accuracy of the calculation could be improved by using a higher-order quadrature rule, as is detailed in ref. [36] and summarized below.

Consider two arbitrary one-dimensional functions  $G$  and  $\rho$ , which in our case could correspond to the impulse response of a certain propagation method and the input field, respectively. The convolution between them is defined as:

$$I(x) = \int_0^L G(x - x')\rho(x')dx' \quad (2.55)$$

According to the extended (or composite) Simpson's rule, the integral above can be approximated as

$$\tilde{I}(x) = \frac{h}{3} \left( f_1 + 4 \sum_{j=1}^M f_{2j} + 2 \sum_{j=2}^{M-1} f_{2j-1} + f_N \right) \quad (2.56)$$

This formula offers an accuracy of order  $O(h^4)$  in the step length  $h$ , that is, the distance between the equally-space grid points. As suggested by the reference, the total number of points ought to be  $N = 2^n - 1$  and  $M = 2^{n-1} - 1$  in order to maximize the efficiency of the FFT (after adding an additional point to make the total a power of two). However, the method is valid as long as  $N$  is odd. The kernel function  $f$  is defined as

$$f(x, x') = G(x, x')\rho(x') \quad (2.57)$$

and  $f_j(x) = f(x, x'_j)$  correspond to the kernel function evaluated at the sampling points  $x'_j = (j - 1)h$ . One can now define a new function  $\tilde{\rho}$  such that

$$\tilde{\rho}(x_j) = \begin{cases} \rho(x_j) & : j = 1 \\ 4\rho(x_j) & : j = 2l \\ 2\rho(x_j) & : j = 2l - 1 \\ \rho(x_j) & : j = N \end{cases} \quad (2.58)$$

Then, applying equation 2.56 to grid point  $i$  and rewriting it in terms of this new function:

$$\tilde{I}(x_i) = \frac{h}{3} \sum_{j=1}^N G(x_i - x_j)\tilde{\rho}(x_j) \quad (2.59)$$

Direct calculation of this summation would require  $O(N)$  operations for each point  $x_i$ ,  $i = 1..N$ , which would result in a total of  $O(N^2)$  for all points in the convolution. However, recall that the discrete convolution is usually calculated with the Riemann sum

$$\tilde{I}'(x_i) = h \sum_{j=1}^N G(x_i - x_j)\rho(x_j) \quad (2.60)$$

This formula is similar, but not exactly equal, to the rectangle (or midpoint) and the trapezoidal rules, which provide an accuracy of  $O(h^2)$ . Additionally, it can be calculated by means of a few FFTs [37], thus reducing the cost to  $O(N \log N)$ . Notice that the only difference between the two is that a certain factor is applied to convert from  $\rho(x_j)$  to  $\tilde{\rho}(x_j)$ , which can be done in linear time. Consequently, the new method allows for a higher-quadrature calculation while maintaining the same computational cost. Zero-padding can still be applied in the exact same way (after the field coefficients are modified).

### 2.3.3 Band-limited Angular Spectrum

Consider the calculation of diffraction from an aperture with the different methods presented earlier. The accuracy of the RS method (and, similarly, the Fresnel convolution method) depends on the accuracy of the numerical integration, which can be improved simply by using a smaller sampling interval. Regarding the computation window, it suffices that it is, at least, the same size as the aperture. On the other hand, the AS method (and also the Fresnel-AS) requires that the size of the computation window is large enough that the light fields outside of it on the observation plane can be neglected for a given desired accuracy [29], while an oversampling of the same window will not bring any improvement. The need of computational

windows that are much larger than the aperture leads to high computational loads, and thus limits the application of the AS method to small apertures and near-field cases. Note that this is essentially a sampling issue, and therefore it occurs even if the convolution is linearized.

A possible solution that allows for long-distance propagation using the AS method is proposed in ref. [35], which avoids aliasing problems in the transfer function by limiting its bandwidth and removing unnecessary high-frequency signals in the input field. The derivation of this solution is presented for the AS method, although it can also be applied to the Fresnel-AS. Start by considering the AS transfer function, in one dimension:

$$H(u; z) = e^{i\phi(u)}, \quad \phi(x) = 2\pi z(\lambda^{-2} - u^2)^{1/2} \quad (2.61)$$

The local signal frequency of the function  $H(u; z)$  is given by

$$f_u = \frac{1}{2\pi} \frac{\partial \phi}{\partial u} = \frac{-uz}{[\lambda^{-2} - u^2]^{1/2}} \quad (2.62)$$

During discretization of the transfer function, it is sampled at intervals of  $\delta_u = (2S_x)^{-1}$ , or  $\delta_u = S_x^{-1}$  if the convolution is not linearized, being  $S_x$  the size of the computation window. To avoid aliasing error, the Nyquist theorem requires that  $\delta_u^{-1} \geq 2|f_u|$ . In practice, however, the sampling interval is often fixed, and therefore the maximum frequency that causes no aliasing errors is:

$$|u| \leq \frac{1}{[(2\delta_u z)^2 + 1]^{1/2} \lambda} \equiv u_{limit} \quad (2.63)$$

Consequently, only frequencies below this value ought to be considered in the transfer function. In other words, its bandwidth must be limited to  $2u_{limit}$ :

$$H'(u; z) = H(u; z) \cdot \text{rect}\left(\frac{u}{2u_{limit}}\right) \quad (2.64)$$

This new transfer function avoid aliasing issues caused by the sampling. However, this limit in the bandwidth will also be applied to the field, and therefore one must check whether it is compatible with the field's frequency requirements for an accurate calculation. In order to do that, consider the model depicted in figure 2.1. An aperture of size  $W_x$  is placed at the center of a sampling windows with size  $S_x$ . The highest spatial frequency may be given, for instance, by the field emitted from the lowest point of the aperture and observed at the upper end of the sampling window at the destination plane. Therefore, the maximum frequency is  $u_{max} = \sin \theta / \lambda$ .

If the cutting frequency  $u_{limit}$  is smaller than  $u_{max}$ , an error will be introduced since the source field will lose frequency components that are necessary for exact diffraction. From the geometry of the model, the minimum required bandwidth is found to be:

$$u_{need} \equiv 2u_{max} = 2 \left[ \left( \frac{2z}{W_x + S_x} \right)^2 + 1 \right]^{-1/2} \lambda^{-1} \quad (2.65)$$

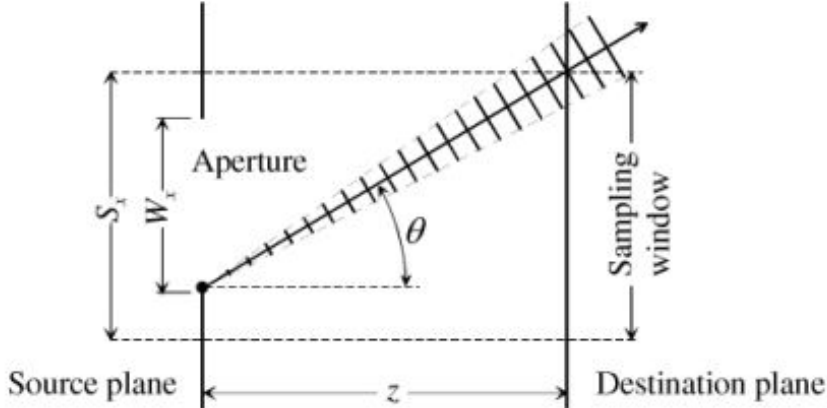


**Figure 2.1:** Model for the minimum bandwidth required for exact calculation of field propagation. Figure taken from ref. [35].

The maximum value of  $u_{need}$  is obtained when the aperture size is the same as that of the sampling window ( $W_x = S_x$ ), in which case it is equal to  $2u_{limit}$ . As a result, the bandwidth found with this method always satisfies the field's bandwidth requirement. This result is of great importance because of two main reasons. First, it allows to use a single method no matter the propagation distance instead of having to check the sampling requirements for each case to choose the appropriate one. Second, it provides a method to calculate far-field diffraction with only two FFTs rather than the three of the RS method, while also maintaining the size of the computation window and the sampling interval, as opposed to single-FFT direct integration.

The extension of this method to the two-dimensional case is performed in exactly the same way, but requires some specific comments. Starting again from the AS transfer function:

$$H(u, v; z) = e^{i\phi(u)}, \quad \phi(x) = 2\pi z(\lambda^{-2} - u^2 - v^2)^{1/2} \quad (2.66)$$

Its local signal frequency is:

$$f_u = \frac{1}{2\pi} \frac{\partial \phi}{\partial u} = \frac{uz}{[\lambda^{-2} - u^2 - v^2]^{1/2}} \quad (2.67)$$

$$f_v = \frac{1}{2\pi} \frac{\partial \phi}{\partial v} = \frac{vz}{[\lambda^{-2} - u^2 - v^2]^{1/2}} \quad (2.68)$$

To avoid aliasing the sampling condition has to be satisfied in both coordinates:  $\delta_u^{-1} \geq 2|f_u|$  and  $\delta_v^{-1} \geq 2|f_v|$ . Denoting by  $S_x$  and  $S_y$  the sampling window size in the  $x$  and  $y$  directions, then  $\delta_u = (2S_x)^{-1}$  and  $\delta_v = (2S_y)^{-1}$  provided that the field is zero-padded. Substituting  $f_u$  and  $f_v$  in these conditions, one obtains the region to which the sampled transfer function is limited:

$$\frac{u^2}{u_{limit}^2} + \frac{v^2}{\lambda^{-2}} \leq 1 \quad (2.69)$$

$$\frac{u^2}{\lambda^{-2}} + \frac{v^2}{v_{limit}^2} \leq 1 \quad (2.70)$$

where  $v_{limit} = [(2\Delta vz)^2 + 1]^{-1/2}\lambda^{-1}$ , analogously to how  $u_{limit}$  was defined previously (eq. 2.63). Both relations give ellipsoidal regions with a major radii  $a = 2\lambda^{-1}$  in the  $uv$  plane and a minor radii  $b = u_{limit}$  and  $b' = v_{limit}$ , respectively. The (second) eccentricity for the first ellipse is given by

$$e'_u = \sqrt{\frac{a^2}{b^2} - 1} = \sqrt{\frac{\lambda^{-2}}{\lambda^{-2}[(2\delta_u z)^2 + 1]^{-1}} - 1} = 2\delta_u z \quad (2.71)$$

Similarly,  $e'_v = 2\delta_v z$ . Note that the first of these ellipses is vertical while the second one is horizontal. The transfer function (and the spectrum of the wave field) must be limited within the common area of these ellipsoidal regions. If either ellipse is sufficiently flat, that is, if the eccentricity is greater enough than zero, then the region inside the ellipses can be approximated by a rectangle. One can adopt the criterion that the eccentricity must be greater than  $1/2$  and thus, assuming that zero-padding is used, the following approximations are obtained:

$$|u| \leq u_{limit} \quad \text{if } S_x \ll 2z \quad (2.72)$$

$$|v| \leq v_{limit} \quad \text{if } S_y \ll 2z \quad (2.73)$$

Consequently, if both conditions are satisfied the common region is a simple rectangle and the band-limited transfer function can be written similarly to the 1-dimensional case:

$$H'(u, v; z) = H(u, v; z) \cdot \text{rect}\left(\frac{u}{2u_{limit}}\right) \cdot \text{rect}\left(\frac{v}{2v_{limit}}\right) \quad (2.74)$$

It is important to keep in mind that in the near field, where the approximation may not hold, the sampling criteria for the AS formula might be satisfied, and then the limit in bandwidth would not be necessary.

## 2.4 Simulation test: diffraction from a slit

As an illustrative example, we performed a simple test for all the proposed methods, consisting in the calculation of the one-dimensional diffraction pattern, in particular the amplitude of the field, generated by a unit-amplitude plane wave incident on a single slit. The simulation was executed for all the diffraction formulas, and the additional methods were applied to ensure that the numerical errors that appeared were fixed. Only the more significant results are presented below.

The following parameters were used:

- Number of grid points:  $N = 1000$
- Total size of the grid:  $L = 4 \text{ mm}$
- Optical wavelength:  $\lambda = 1 \mu\text{m}$
- Aperture size:  $D = 0.5 \text{ mm}$
- Propagation distance:  $z = 0.1 \text{ m}$

The first method we consider is the calculation of Fraunhofer and Fresnel's diffraction formulas by means of a single FFT and a change of coordinates. The former was confirmed to give numerically correct results (at least qualitatively, a quantitative study of the error was not performed) as compared to the analytical solution in the Fraunhofer regime. However, the obtained pattern does not correspond to the actual diffraction pattern because for the given parameters the observation plane is not in the far field. On the other hand, since Fresnel's formula does not have this limitation it does return the proper output, which is shown in figure 2.2. The downside of this method, as it was mentioned earlier, is that the transverse axis is enlarged due to the change of coordinates, which in turn results in a loss of resolution. Therefore it is not suitable for performing consecutive propagations.

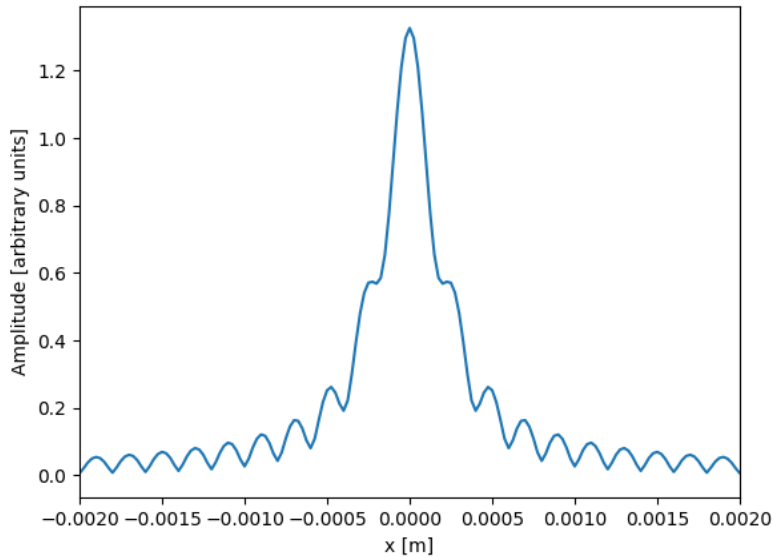


**Figure 2.2:** Fresnel diffraction pattern after a slit illuminated by a plane wave, calculated using direct integration via a single FFT. The horizontal axis has been enhanced to match the size of the original computation window.

Moving forward, the Rayleigh-Sommerfeld and Fresnel convolution methods are treated equally since they involve exactly the same calculations, only with a different impulse response. The same is true between the Angular Spectrum and the Fresnel Angular Spectrum methods, which only differ in the form of the impulse response. For this reason, in both cases the tests were performed using the most general method, that is, not considering the paraxial approximation. What is more, both the RS and AS methods identical results under the proper conditions, at least up to a certain degree of accuracy that is not discussed here. Therefore we will use the AS results as a reference to discuss both methods.

We repeated the test applying directly the AS formula, that is, performing the corresponding operations without making any modification to the field or the transfer function. The result is shown in figure 2.3. One can quickly see that there is some kind of ringing effect along the whole pattern. This is a consequence of the aliasing issues in the transfer function, since the sampling conditions of the Angular Spectrum formula are not fulfilled. As we found in the previous section, this ought to be fixed by simply deleting the higher-frequency components of the transfer function (and therefore the field) according to equation 2.64. For the given parameters, the maximum frequency is found to be  $u_{limit} \approx 2 \times 10^{-4}$  Hz.

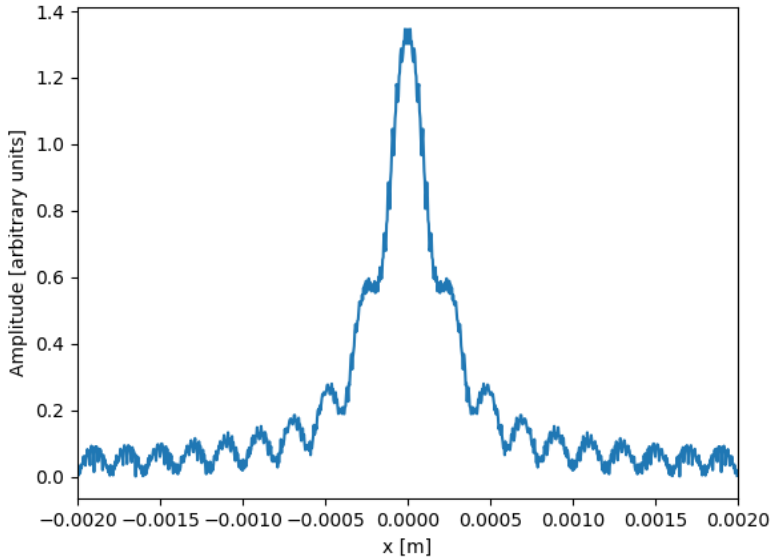


**Figure 2.3:** Diffraction pattern after a slit illuminated by a plane wave, calculated using the Angular Spectrum method. The ringing effect is due to the unfulfilment of the sampling requirements for the AS transfer function.

Note that the result of clipping the transfer function (fig. 2.4) is the same as if we had used the RS formula in the first place. This proves that, in principle, both methods can be used interchangeably in the far-field (in the sampling sense of the word, not to be confused with the Fraunhofer region). In spite of the improvement, the pattern still shows some ringing at the edges, but this was already expected since it is a consequence of the circular convolution. Applying zero padding (and changing the maximum frequency accordingly) we get the proper pattern, depicted in figure 2.5. Notice that it is practically the same that obtained by direct integration of Fresnel's formula, but with a much better resolution (in fact, the sampling remains the same as in the object plane). Finally, we can check that a very similar result is reached using Simpson's rule. In this particular case, the fact that we used an even number of points does not produce a noticeable effect, but in general an odd number of samples should be used to ensure that the results are as reliable as possible.

With these results we have proven that the numerical model discussed in this chapter allows to calculate efficiently the diffraction from a simple initial field. In particular, we have shown that we can avoid the numerical issues associated to the AS formula, and so it can be used regardless of the propagation distance as long as the field

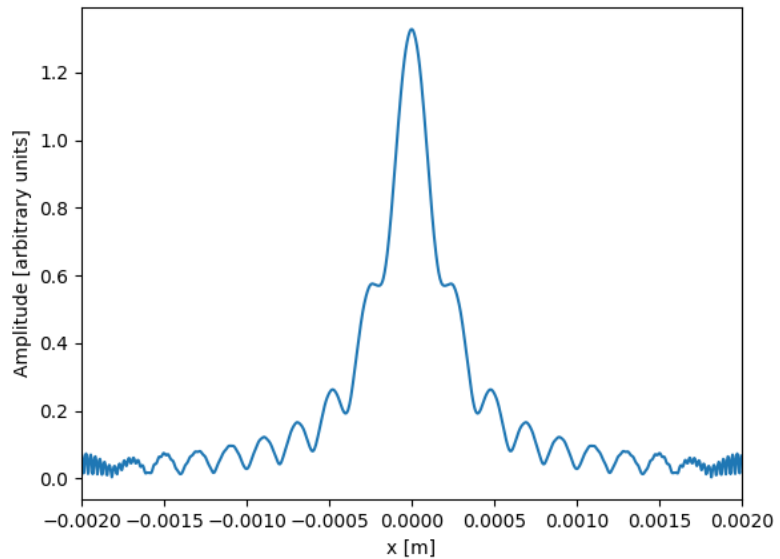


**Figure 2.4:** Diffraction pattern from a slit illuminated by a plane wave, calculated using the Angular Spectrum formula and applying with a limited bandwidth. The ringing effect at the edges is caused by the fact that the convolution has not been linearized.

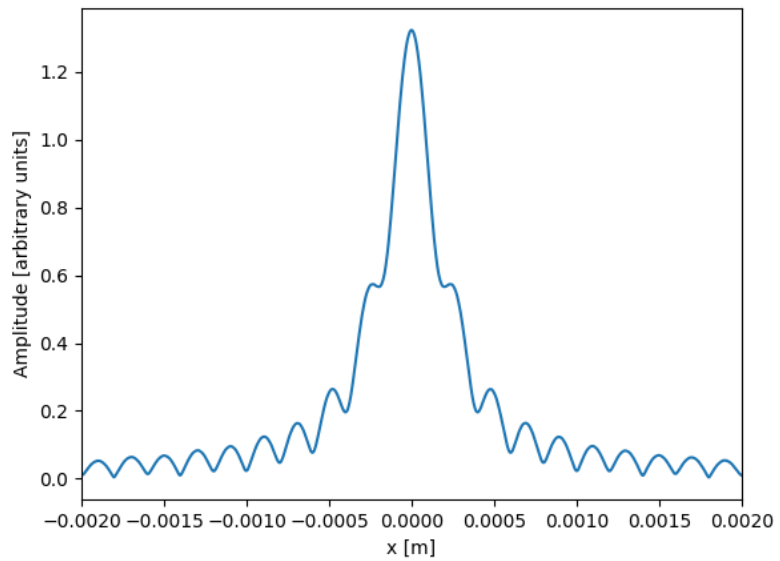


**Figure 2.5:** Diffraction pattern from a slit illuminated by a plane wave, calculated with the Angular Spectrum method using zero-padding as well as a limited bandwidth.

satisfies the sampling conditions. This model, and primarily the AS method, will be employed in the following chapters to perform the simulations of various systems, including images from single gratings as well as grating-based interferometers.

# Chapter 3

## Self-imaging effects for amplitude and phase gratings

Grating-based interferometers, as we will see in the following chapter, often rely on the gratings' capability to produce patterns in the near field that resemble the grating structure. For a transmission grating illuminated by a plane wave this effect is called the Talbot effect, or Lau effect if the beam is incoherent. Similarly, phase gratings can also be used to produce intensity patterns similar to their phase structure, which are called Lohmann images. In this chapter these effects are introduced for the case of plane wave illumination, and afterwards generalized to the case of Gaussian beams. Finally, experimental verification is obtained using a cone beam consisting of a Gaussian beam magnified by a lens.

### 3.1 Talbot effect

Discovered by Henry Fox Talbot in 1836 [21] and later explained by Lord Rayleigh in 1881 [38], the Talbot effect is a near-field diffraction effect according to which, when a periodic structure (i.e. grating) is illuminated with a coherent quasi-monochromatic plane wave, perfect images of the structure (usually referred to as self-images, or sometimes Fourier images) are replicated at regular distances. At fractional distances, sub-images having a multiple of the frequency can also be observed.

For a collimated beam and in the paraxial approximation (and assuming that the period  $P$  of the grating is large as compared to the wavelength  $\lambda$  of the beam), the standard Talbot distance (or Talbot length) is defined as:

$$Z_T = \frac{2P^2}{\lambda} \tag{3.1}$$

Alternatively, in the literature it is also common to find this definition but dropping the 2 factor [39], for reasons that will become apparent later on.

The Talbot effect occurs for both absorbing and phase objects. These constitute the two limit cases, while in reality objects act as a superposition of the two situations. For an amplitude grating, the image is repeated every half Talbot length (possibly with a half-period displacement), and the frequency of the pattern is doubled each

time the distance  $Z_T/2$  is divided by two. On the other hand, for a phase grating the behaviour depends on the phase shift induced by the structure. At an exact distance  $Z_T$  away from the periodic object, no contrast is observable, but an amplitude modulation is generated at fractions of the Talbot distance.

In order to differentiate planes where the same spatial frequency is observed, a fractional Talbot distance is defined [40]:

$$Z_{T_n} = \frac{n}{m} Z_T \quad (3.2)$$

with  $n$  and  $m$  some integers. For instance, for a  $\pi$ -phase-shift grating,  $m = 16$  and the fractional Talbot order  $n$  is defined by:  $Z_{T_n} = \frac{n P^2}{8\lambda}$ ,  $n = 1, 3, 5, \dots$ . At each distance  $Z_{T_n}$  a periodic pattern of frequency  $f = 2/P$  will be observable.

This self-image phenomenon can also be observed with incoherent light, as was described by E. Lau in 1948 [41], and it is now called the Lau or Talbot-Lau effect [42]. For this effect to take place, the wave has to be monochromatic but not necessarily collimated or transversely coherent. However, a second grating must be added to the system under a certain placement condition [43].

### 3.1.1 Theoretical development

To describe the Talbot effect more accurately the derivation in ref. [43] will now be reproduced. Consider a plane wave that is incident on a static grating placed at  $z = 0$ , which spans (infinitely) over the  $xy$  plane and has its periodic modulation in the  $x$  direction. The fact that the grating is static allows to factor out the time dependence of the wave. Therefore, it can be represented as  $\psi = e^{ik_\theta x}$  before it enters the grating, where  $k_\theta = k \sin \theta$  is the projection of the incident wave vector onto the  $x$ -axis and  $k = 2\pi/\lambda$ .

Denoting the transmission function of the grating as  $T(x)$ , the wave after the grating becomes

$$\psi(x, +0) = \psi(x, -0) \cdot T(x) = \sum_n A_n e^{i(k_\theta + nk_p)x} = \sum_n A_n e^{ik_{\perp,n}x} \quad (3.3)$$

where  $A_n$  represents the components of the Fourier series of  $T(x)$ . One can see that diffraction at a grating of period  $P$  adds multiples of  $k_p = 2\pi/P$  to the transverse wave vector of the incident plane wave.

This wave is now propagated an arbitrary distance along the  $z$  direction. As it can easily be checked with the Angular Spectrum formula, this propagation simply adds a phase of  $k_z z$  to the wave, where  $k_z = [k^2 - k_{\perp}^2]^{1/2}$  is the component of the wave vector parallel to the  $z$  axis. In the paraxial approximation ( $k_{\perp,n} \ll k$ ) the phase can be expanded to second order:

$$\psi(x, z) = \sum_n A_n \exp \left[ i(k_\theta + nk_p)x + i \left( k - \frac{(k_\theta + nk_p)^2}{2k} \right) z \right] \quad (3.4)$$

This expression will now be particularized for the Talbot effect, which occurs when the wave is normally incident onto the grating. For the Talbot-Lau case, averaging

the intensity  $I = \psi(x, z)\psi^*(x, z)$  over all non-zero angles of incidence  $\theta$  would be required, as will be mentioned briefly at the end of the section. Setting  $k_\theta = 0$ , the expression above becomes

$$\psi(x, z) = \sum_n A_n e^{ink_p x} e^{-in^2\pi(z/L_T)} \quad (3.5)$$

where the Talbot length has been defined here as  $L_T = P^2/\lambda$  and a global constant phase has been dropped.

When the observation plane is at an even multiple of the Talbot length from the grating, that is,  $z = 2nL_T$  with  $n$  a positive integer, the resulting wave is found to be exactly equal to the transmitted amplitude at the grating. One can then say that a self-image is generated. A similar reasoning can be applied when the observation plane is at an odd multiple,  $z = (2n + 1)L_T$ . In that case, since  $n$  odd implies that  $n^2$  is also odd and  $n$  even implies  $n^2$  even, and equation 3.4 reduces to:

$$\psi(x, z = L_T) = \sum_n A_n e^{ink_p x} e^{-in\pi} = \sum_n A_n e^{ink_d(x-d/2)} \quad (3.6)$$

With this expression the original pattern is recovered, except that it is displaced in  $x$  by half the grating period.

Other values of  $z$  can also give interesting results. When  $z$  is a rational multiple of  $L_T$ , the imaged field is a sum of shifted versions of the original grating pattern, each multiplied by a certain factor. The details are not discussed here, but can be found in the reference provided at the beginning of this. The conclusion that is reached is that for an integer multiple of  $L_T$ , the field contains a single copy of the original wave, for  $z = L_T/2$  it is a superposition of two waves, for  $z = L_T/3$  or  $z = 2L_T/3$  it is a superposition of three waves, and so on. In other words, fractional Talbot images appear at all rational multiples of  $L_T$ ,  $z = (r/q)L_T$  with  $r$  and  $q$  coprime integers and  $r < q$  [39]. These fractional images consist of  $q$  equally spaced copies of the transmission function of the grating, which superpose coherently as they overlap. This results in a detailed fractal pattern called the Talbot carpet [44].

Regarding the Talbot-Lau effect, the addition of a second grating at  $z = L_1$  is needed to refocus the waves and form a clear grating image, otherwise the overlaying self-images would spread out after the first grating. The calculation of the intensity after the two objects can be done by applying the same treatment as for the Talbot case (twice, since now there are two propagations), keeping the  $k_\theta$  term. To account for the spatial incoherence of the beam, one must sum over all the independent plane waves that originated from a different wave vector  $k_\theta$ :

$$I_{Lau} = \sum_\theta I_\theta \quad (3.7)$$

where  $I_\theta$  denotes the intensity due to the wave incident at an angle of  $\theta$ . In order for the resulting pattern to be well defined, the distance between the gratings and the distance between the second grating and the observation plane have to satisfy a certain relationship [45]. Originally, Lau chose to put the detector at an infinite distance, but one can also obtain a strong pattern by setting both distances equal.

### 3.1.2 Amplitude gratings

The results obtained in the previous section describe the expected behavior of the field after an arbitrary one-dimensional periodic object. In particular, equation 3.4 provides an analytical expression for the complex amplitude of the wave at any distance in the near-field of the object, where it can be assumed to extend infinitely. A significant case of interest is that of a binary amplitude grating with a filling factor  $f$ . For such a grating, its Fourier series coefficients are [43]:

$$\begin{cases} A_0 = f \\ A_n = \sin(n\pi f)/n\pi \end{cases} \quad (3.8)$$

For example, consider a grating of period  $P = 40 \mu\text{m}$ , upon which a plane of wavelength  $\lambda = 623.8 \text{ nm}$  is incident. The Talbot carpets generated by the grating when its filling factor is  $f = 0.5$  and  $f = 0.1$  are shown in figures 3.1 and 3.2, respectively. In the calculation of this carpets, the Fourier series of the grating has been truncated at an order of  $n = \pm 25$ , and the field has been calculated at distance steps of  $dz = 10 \mu\text{m}$ . Moreover, the intensity has been normalized independently at step for clarity purposes, and thus intensity at different distances should not be compared quantitatively. This will also be the case for the rest of the carpets presented in this section, unless explicitly stated otherwise.

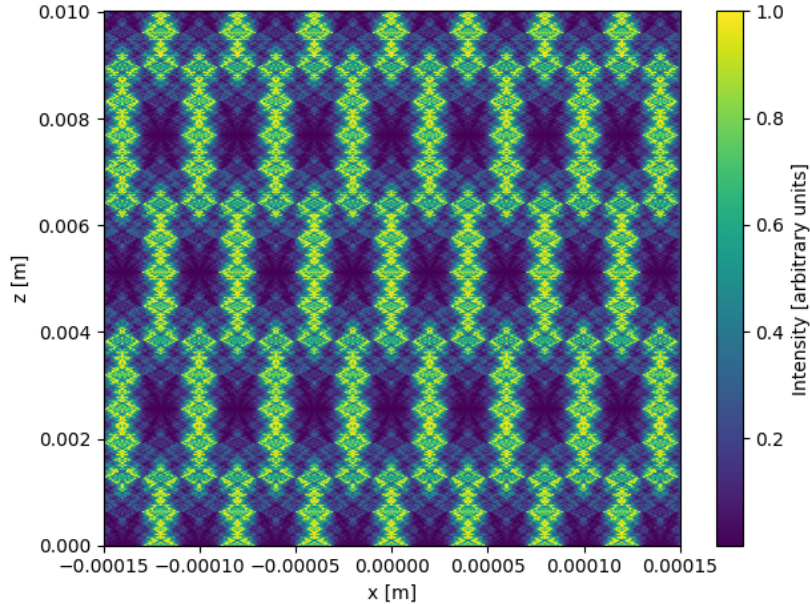


**Figure 3.1:** Talbot carpet generated by a binary amplitude grating with period  $P = 40 \mu\text{m}$  and duty cycle  $f = 0.5$  illuminated by a plane wave of wavelength  $\lambda = 623.8 \text{ nm}$ . The intensity at each distance step is obtained from the analytical expression of the wave.

Clearly, the pattern with the smallest duty cycle resembles more the fractal pattern that we expected. This is only a consequence of the coherent overlaps between the copies of the field, that occur more easily with a higher filling factor of the grating. Furthermore, we can check that in both cases the intensity pattern at the Talbot distance, which for our example is found to be  $Z_T \approx 5.13 \text{ mm}$ , does indeed reproduce the grating's structure, as can be appreciated in figure 3.3.

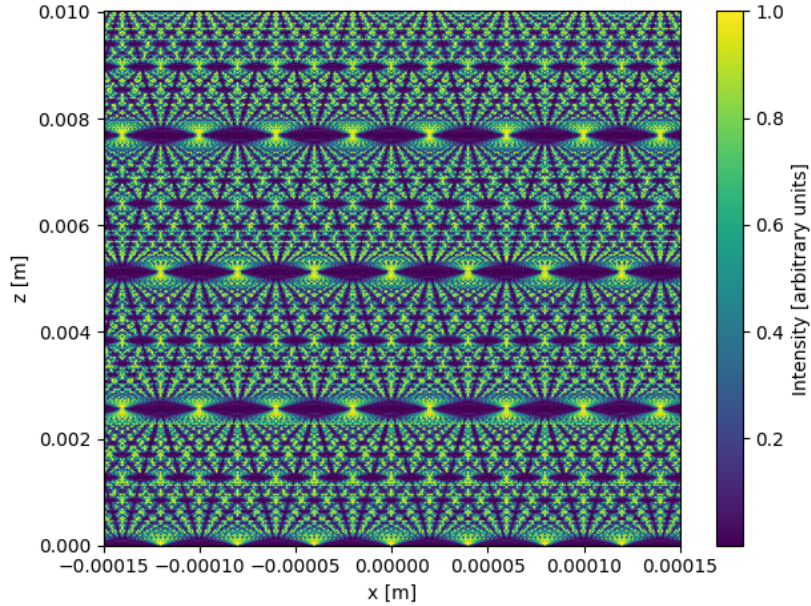


**Figure 3.2:** Talbot carpet generated by a binary amplitude grating with period  $P = 40 \mu\text{m}$  and duty cycle  $f = 0.1$  illuminated by a plane wave of wavelength  $\lambda = 623.8 \text{ nm}$ . The intensity at each distance step is obtained from the analytical expression of the wave.

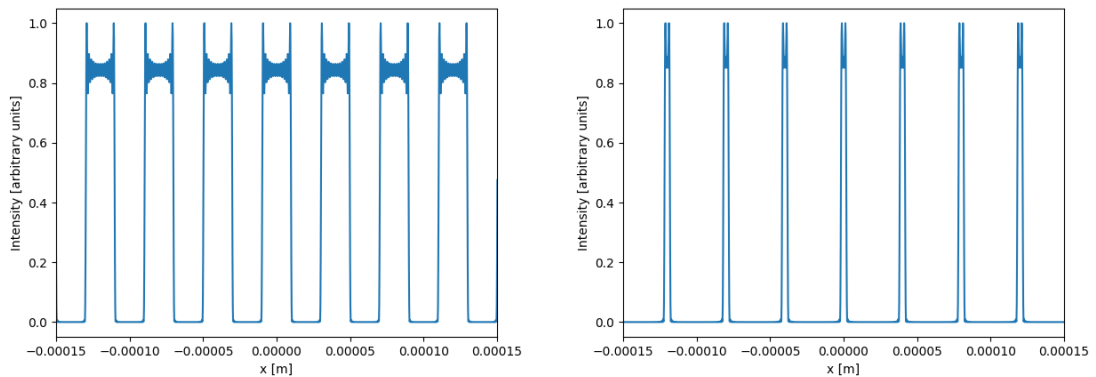


**Figure 3.3:** Analytic Talbot self-image from a binary grating with a duty cycle of  $f = 0.5$  (left) and  $f = 0.1$  (right), corresponding to the intensity pattern at the Talbot distance when the grating is illuminated by a plane wave. The wavelength is  $\lambda = 623.8 \text{ nm}$  and the grating period  $P = 40 \mu\text{m}$ . The Fourier series of the grating was taken up to an order of  $n \pm 25$ .

Once we know what we expect to see after the grating based on the analytical solution, we can attempt to reproduce the Talbot carpet by calculating the diffraction from the grating using the methods presented in the previous chapter. In particular, we use Angular Spectrum method. Note that we cannot consider an infinite grating anymore, so we (arbitrarily) limit its width to 2 mm. The carpet obtained for the 10 % duty cycle grating is shown in figure 3.4. We observe that the result is apparently the same, although the pattern becomes blurrier at the top. This can be attributed to the limited size of the grating. As distance increases, the field progressively loses the shape of the (finite) grating and turns into its Fraunhofer pattern.

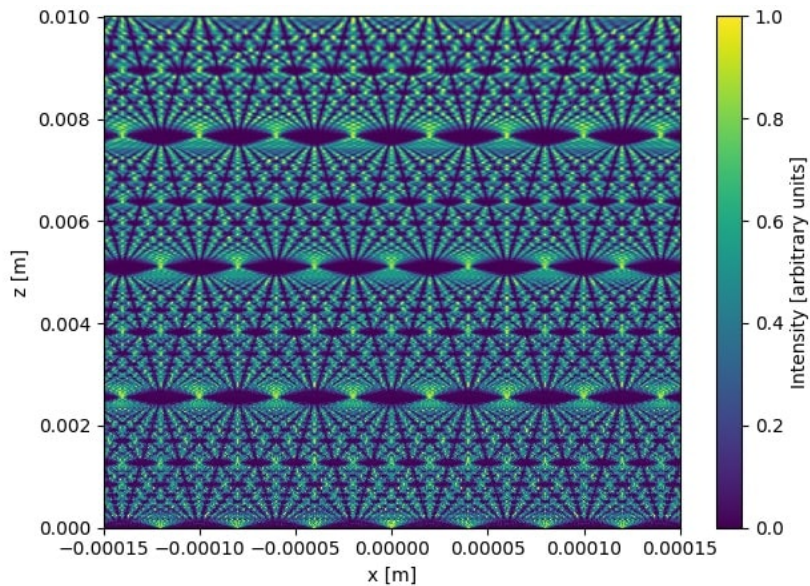


**Figure 3.4:** Talbot carpet after a binary amplitude grating with  $f = 0.1$ , simulated using the Angular Spectrum method. The grating has a period of  $P = 40 \mu\text{m}$  and is illuminated by a plane wave with wavelength  $\lambda = 623.8 \text{ nm}$ .

For clarity reasons, we choose again the 50 % duty cycle grating to check the pattern at the Talbot distance. The result of the corresponding simulation is shown on the left in figure 3.5. It is clear that the pattern resembles that of the grating, but not very accurately. According to ref. [46], the more slits are used for the grating, the closer the resulting pattern will be to its general form (i.e. a proper square wave). Our grating has a period of  $40 \mu\text{m}$  and a size of 2 mm, meaning that it has about 50 slits, which should be enough for that matter. However, as is also noted in the reference, the quality of the images cannot be improved indefinitely by using a wider grating. Recall that the Talbot effect is derived using the Fresnel approximation, and therefore it is only valid in the paraxial region. This imposes a limit on the width of the grating and, consequently, on the number of slits that effectively contribute to generate the image.

For comparison purposes, we can run the simulation again using the same parameters as in the experiment presented in ref. [43], which correspond to a wavelength of  $\lambda = 532 \text{ nm}$  and a grating period of  $P = 200 \mu\text{m}$ . The filling factor of the grating is set to  $f = 0.5$  and its size is limited to 20 mm. The pattern at the new Talbot distance, which is  $Z_T \approx 150 \text{ mm}$  is shown on the right in figure 3.5.

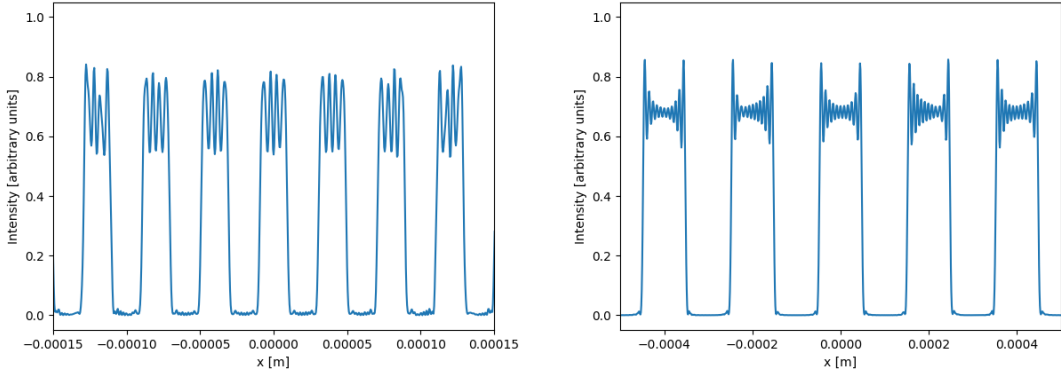


**Figure 3.5:** Talbot self-image from a binary grating with a duty cycle of  $f = 0.5$ , corresponding to the intensity pattern at the Talbot distance under plane wave illumination, simulated using the Angular Spectrum method. The grating period and wavelength are (left)  $P = 40 \mu\text{m}$  and  $\lambda = 623.8 \text{ nm}$ , and (right)  $P = 200 \mu\text{m}$  and  $\lambda = 532 \text{ nm}$ . Note that the Talbot distance is different in both cases.

### 3.1.3 Phase gratings

The transmission function for a binary phase grating can be written as

$$T(x) = e^{-i\phi G(x)} \quad (3.9)$$

where  $G(x)$  is the transmission function of a binary amplitude grating, which allows control over the grating's duty cycle  $f$ , and  $\phi$  is a constant phase shift. In reality, the phase function depends on the wavelength of the beam, the height (or profile) of the grating and the material with which it is fabricated.

From this definition, the coefficients of the grating's Fourier series are given by

$$\begin{cases} A_0 = 1 - f + fe^{-i\phi} \\ A_n = (e^{-i\phi} - 1) \frac{\sin(n\pi f)}{n\pi} \end{cases} \quad (3.10)$$

In this section we will focus on the cases of  $\phi = \pi/2$  and  $\phi = \pi$ , due to their particular characteristics and their importance in practical applications. The calculations will be performed in one of two different ways, each using a different set of parameters. On the one hand, the Talbot carpets will be generated using the analytical expression of the field, truncating the Fourier series at  $n = \pm 25$ . We will consider a plane wave with wavelength  $\lambda = 623.8 \text{ nm}$  incident on phase grating with an arbitrary phase shift, but fixed period  $P = 40 \mu\text{m}$  and width  $L = 2 \text{ mm}$ . This will allow to reduce the computational cost associated to the carpets, due to the shorter Talbot distance and the smaller number of points needed for each pattern. On the other hand, single patterns will be simulated using the Angular Spectrum method, unless explicitly stated otherwise. The parameters will be set to  $\lambda = 532 \text{ nm}$ ,  $P = 200 \mu\text{m}$  and  $L = 20 \text{ mm}$ . In spite of both sets being completely unrelated, the results can be explained relative to the Talbot distance for each case, that is to say, the same effects should be encountered at equal fractional distances of  $Z_T$ . Gratings with a filling

factor of  $f = 0.5$  will be considered at first; other values will be discussed at the end of the section.

We start with the  $\pi/2$ -phase grating. There are two special cases that can be extracted from its theoretical Talbot carpet, shown in figure 3.6. The first one is that the contrast is zero at every half-integer multiple of the Talbot distance, meaning that the pattern is (theoretically) constant. This is expected, since these are the distance at which the self-images of the grating are located according to the Talbot effect. The second case of interest is found at  $Z_T/4$ ,  $3Z_T/4$  and so on, where the intensity presents the same modulation as the phase of the grating. These particular modulations correspond to Lohmann images [47], which are defined as square-wave patterns arising from phase gratings that occur at fractions of the Talbot distance. Notice that, as opposed to the Talbot self-images, these are not true replications of the field immediately after the grating.

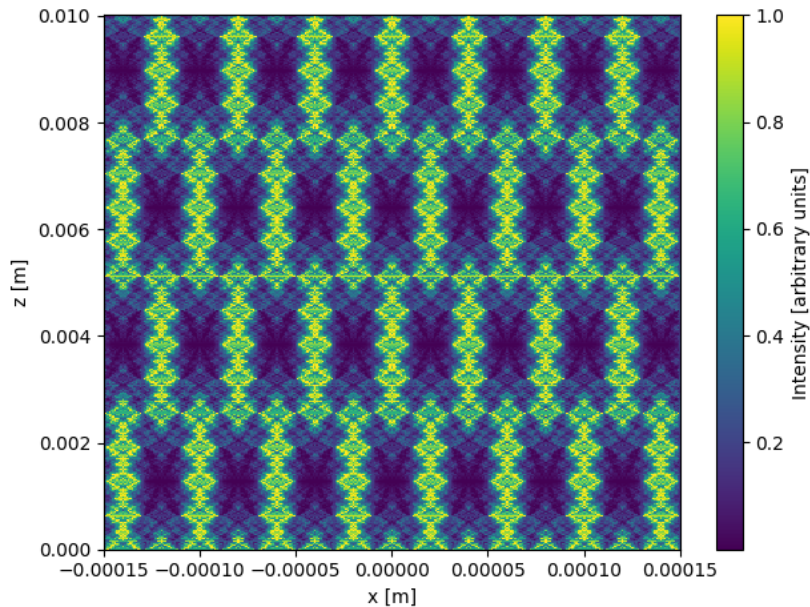


**Figure 3.6:** Theoretical Talbot carpet after a  $\pi/2$ -phase grating with period  $P = 40\text{ }\mu\text{m}$  and opening fraction  $f = 0.5$ , illuminated by a plane wave of wavelength  $\lambda = 623.8\text{ nm}$ .

The appearance of the aforementioned images at certain distances can be checked numerically, as in figure 3.7. Although the resulting pattern is not ideal, it clearly resembles the phase structure of the grating. In the figure, the result we get using the Fresnel transfer function is also included as a comparison to the one obtained with the AS method, which highlights the validity of the approximation.

Regarding the  $\pi$ -phase grating, from its Talbot carpet in figure 3.8 we can see that no contrast should be found at multiples of  $Z_T/8$ . On the other hand, Lohmann images like the one reproduced in figure 3.9 appear at odd multiples of  $Z_T/16$ .

As discussed in ref. [47], Lohmann images only appear for binary phase gratings with a certain filling factor. For instance, in the case of a  $\pi/2$ -phase grating, this phenomenon only occurs when the duty cycle of the grating is  $1/2$ . On the other hand, for a  $\pi$ -phase grating, it happens for an opening fraction of  $1/2$ , as well as  $1/4$  and  $3/4$ . In these last two cases, the images are seen at every odd multiple of

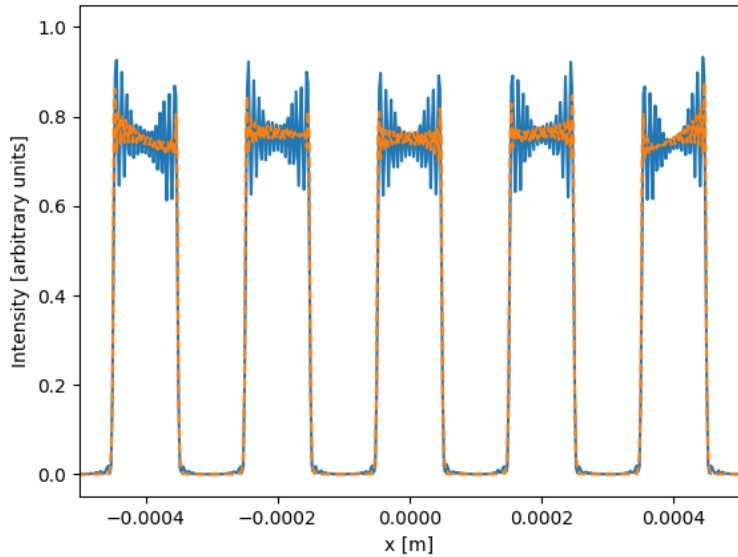


**Figure 3.7:** Lohmann image from a  $\pi/2$ -phase grating with opening fraction  $f = 0.5$ , corresponding to the intensity pattern at a distance  $z = 3Z_T/4$ . The grating period is  $P = 200 \mu\text{m}$ , and the wavelength of the incident plane wave  $\lambda = 532 \text{ nm}$ . The solid blue line corresponds to the simulation using the Angular Spectrum transfer function, while the dashed orange line was obtained with the Fresnel approximation. The Fresnel result is significantly closer to the perfect square pattern. The field is not normalized to 1 due to numerical effects that appear at the edges of the computation window, which are caused by its finite extension.

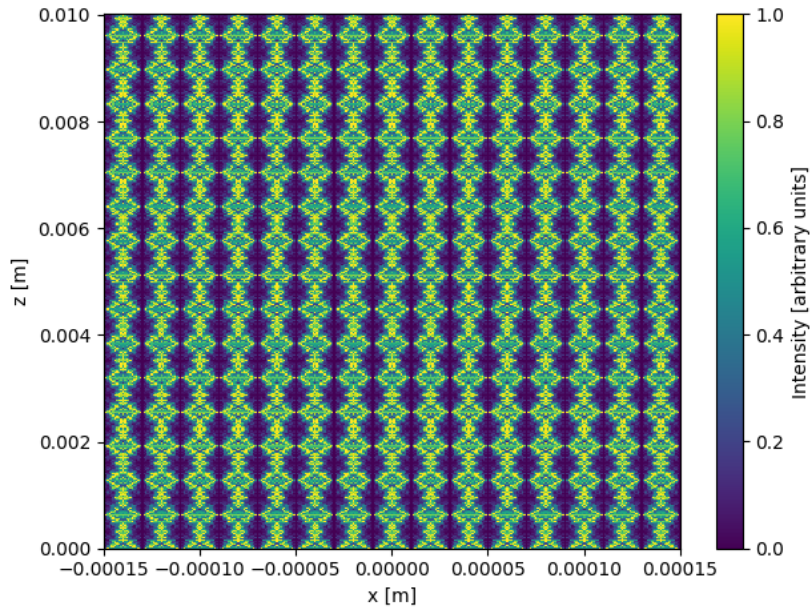


**Figure 3.8:** Theoretical Talbot carpet after a  $\pi$ -phase grating with period  $P = 40 \mu\text{m}$  and opening fraction  $f = 0.5$ , illuminated by a plane wave of wavelength  $\lambda = 623.8 \text{ nm}$ .

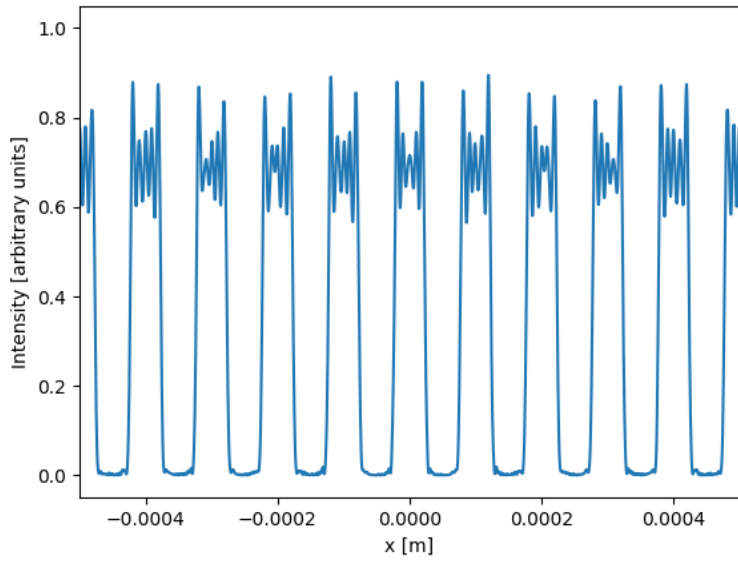


**Figure 3.9:** Lohmann image from a  $\pi$ -phase grating with duty cycle  $f = 0.5$ , corresponding to the intensity pattern at a distance  $z = 15Z_T/16$ . The grating period is  $P = 200 \mu\text{m}$ , and the wavelength of the incident plane wave  $\lambda = 532 \text{ nm}$ .

$Z_T/8$ . The theoretical Talbot carpet for a grating with  $f = 0.5$  and its simulated Lohmann image at  $z = 7Z_T/8$  are shown in figures 3.10 and 3.11, respectively.

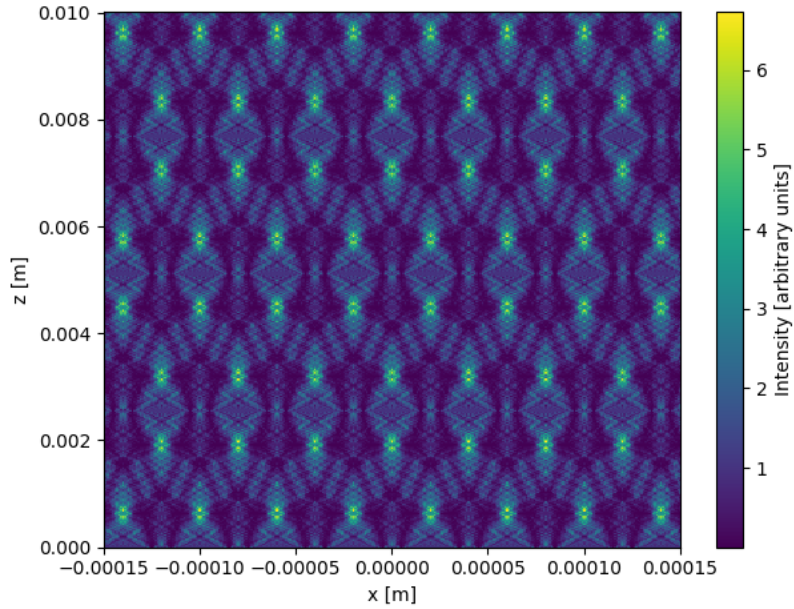


**Figure 3.10:** Theoretical Talbot carpet after a  $\pi$ -phase grating with a duty cycle of  $f = 0.25$ . The grating period is  $P = 40 \mu\text{m}$  and the incident plane wave has a wavelength of  $\lambda = 623.8 \text{ nm}$ . The intensity is not normalized.

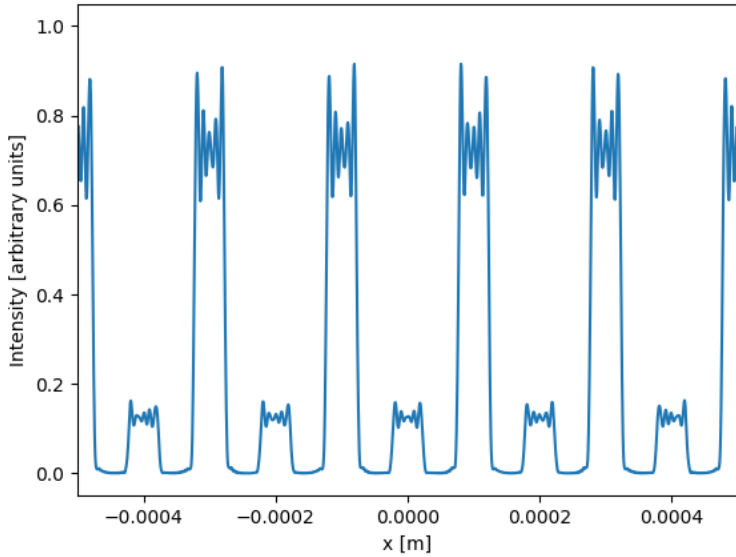


**Figure 3.11:** Lohmann image from a  $\pi$ -phase grating with a duty cycle of  $f = 0.25$ , corresponding to the intensity pattern at a distance  $z = 7Z_T/8$  from the grating. The grating period is  $P = 200 \mu\text{m}$ , and the wavelength of the incident plane wave  $\lambda = 532 \text{ nm}$ .

### 3.1.4 Lau effect

To complete this section, we will now briefly demonstrate the Lau effect. The system consists of two identical binary amplitude gratings, which are always separated by the same distance as there is between the second grating and the observation plane. These gratings are illuminated by an incoherent monochromatic source, which is modelled as a number of independent plane waves that have the same wavelength and amplitude but different angles of propagation. With this system we expect to obtain a pattern after the second grating fairly similar to the Talbot effect.

For the simulation the source waves are chosen to have  $N_\theta$  different angles, evenly spaced between  $\theta_{max} = -\theta_{min} = 0.05 \text{ rad}$ . Their wavelength is  $\lambda = 589 \text{ nm}$ . Regarding the gratings, they have a period  $P = 200 \mu\text{m}$ , and two different duty cycles are initially considered:  $f_1 = 0.4$  and  $f_2 = 0.1$ .

The analytical solution, considering the paraxial approximation, is obtained from the expression of the intensity given in [43]. For example, we can calculate the pattern for a total distance, from the first grating to the observation plane, of one full Talbot length, which for the given parameters is  $Z_T \approx 135 \text{ mm}$ . The resulting pattern is expected to somewhat resemble the grating's structure, as is shown in figure 3.12. The calculations have been performed considering the Fourier series of the gratings up to an order of  $n = \pm 20$ , and  $N_\theta = 51$  waves have been used for the source. In the figure we can clearly see that the peaks are actually wider than in the original pattern, that is, they are far from having a perfect square shape, especially in the higher duty cycle case.

The pattern at a specific distance can also be obtained by means of a simulation. For example, figure 3.13 shows the Lau pattern calculated using the Angular Spectrum method for amplitude gratings with a 10 % duty cycle, where the number of plane

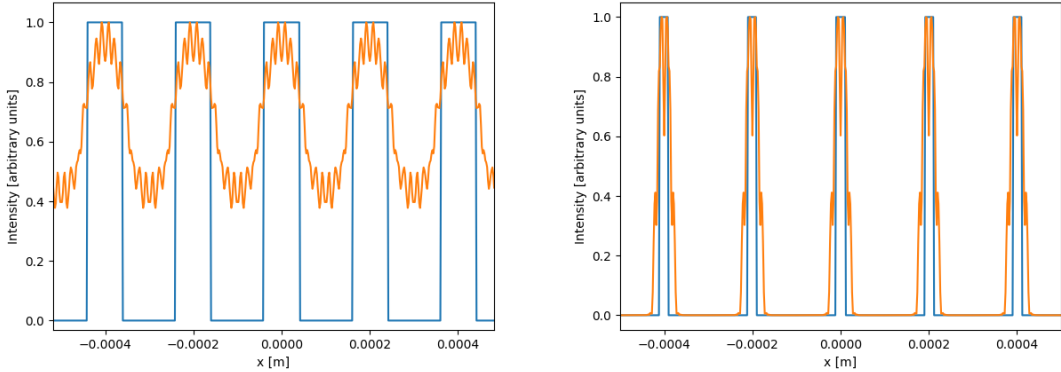


**Figure 3.12:** Analytic self-image in the Lau configuration (orange line), corresponding to the intensity pattern after two identical amplitude gratings with a period of  $P = 200 \mu\text{m}$  and a duty cycle of  $f_1 = 0.4$  (left) and  $f_2 = 0.1$  (right), at a distance of  $Z_T/2$  behind the second grating. The grating separation is also  $Z_T/2$ . The system is illuminated with an incoherent monochromatic beam ( $\lambda = 589 \text{ nm}$ ) composed of several plane waves propagating in different directions, with a maximum of  $0.05 \text{ rad}$  with respect to the normal of the gratings. As a reference, the blue line represents the gratings' transmission function.

waves has been increased to  $N_\theta = 101$ . The duty cycle is chosen so that the peaks do not overlap, and thus can be seen more clearly (recall its effect on the Talbot carpet, discussed previously in this chapter). The plots in the figure correspond to a grating separation of  $Z_T/2$  and  $Z_T/4$ . In the latter case, we see that the frequency of the image is actually doubled with respect to the gratings' transmission function.

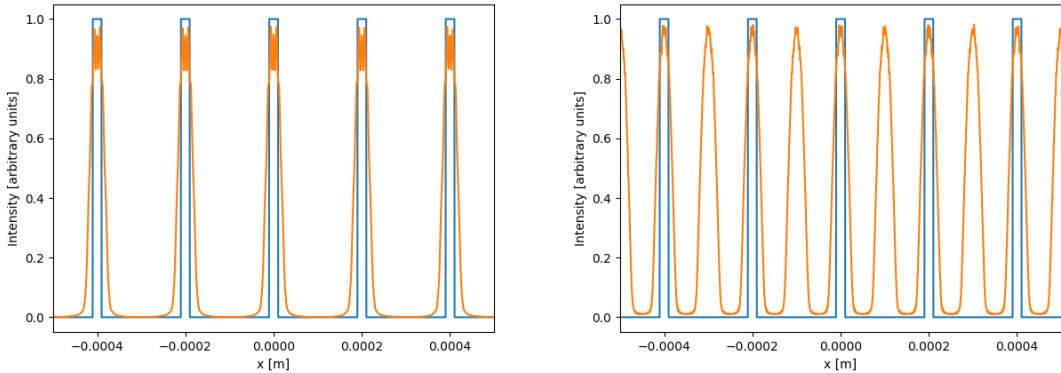


**Figure 3.13:** Intensity pattern (orange line) in the Lau configuration at distances  $Z_T/2$  (left) and  $Z_T/4$  (right) behind the second grating, which are also equal to the grating separation in the respective case. The gratings have a period of  $P = 200 \mu\text{m}$  and a duty cycle of  $f = 0.1$ . The system is illuminated by an incoherent monochromatic beam composed of several plane waves with an angle of propagation equally spaced between  $\pm 0.05 \text{ rad}$  and wavelength  $\lambda = 589 \text{ nm}$ . The blue line represents the transmission function of the gratings, which is included as a reference.

Finally, the carpet generated after the second grating can be plotted, analogously to the Talbot carpet. To do so, we calculate the diffracted field in steps of  $\Delta z = 0.1 \text{ mm}$ . We did not compute it using the analytical expression due to the elevated computational cost. However, the simulated carpet in figure 3.14 is in good agreement

with the one provided in ref. [43], which uses the same parameters, possibly with the exception of the source model, that is not specified in the reference.

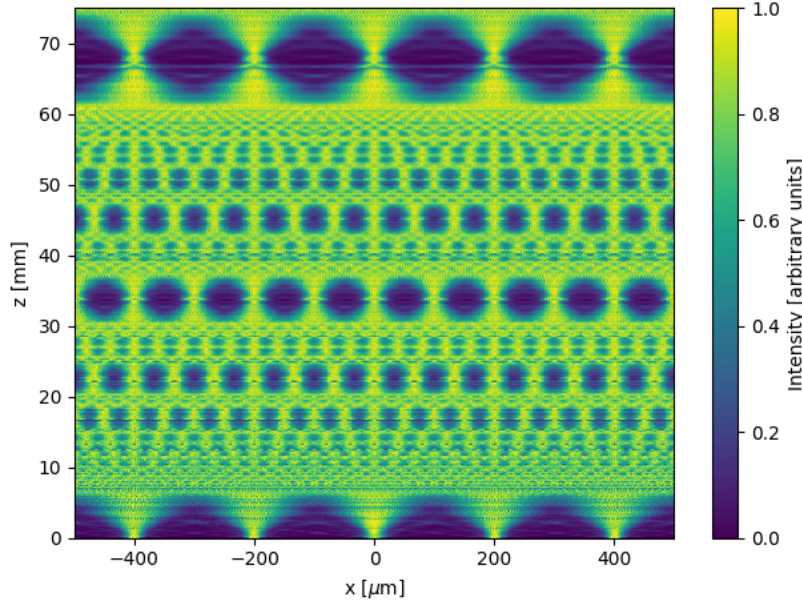


**Figure 3.14:** Lau carpet behind the second of two amplitude gratings with a duty cycle of  $f = 0.1$  placed in the Lau configuration. The vertical axis  $z$  corresponds to the distance from the second grating to the observation plane, which is equivalent to the separation between both gratings. The grating period is set to  $P = 200 \mu\text{m}$ , and the initial beam is composed of several plane waves that share the same wavelength  $\lambda = 589 \text{ nm}$ , each propagating at a different angle with a maximum of  $\theta_{max} = 0.05 \text{ rad}$ .

## 3.2 Near and far-field diffraction of a Gaussian beam

The self-imaging effect described previously can be generalized to work with Gaussian beams. In this section, a brief derivation of such effect is provided, along with a few simulations that demonstrate it in the near field. Additionally, diffraction in the far field is also explored numerically.

### 3.2.1 Theoretical description of self-images

Following the derivation provided in ref. [48], a Gaussian beam is defined as:

$$U(x, y, z) = A \frac{\omega_0}{\omega} e^{-\frac{\rho^2}{\omega^2}} e^{i\left(\frac{k\rho^2}{2R} - \varphi(\gamma)\right)} e^{ik\gamma} \quad (3.11)$$

where  $A$  is the maximum beam amplitude,  $\gamma$  the distance from the beam waist plane,  $\rho = \sqrt{x^2 + y^2}$  the distance to the  $z$  axis,  $\omega_0$  the beam waist radius,  $\omega$  the beam radius at plane  $\gamma$ ,  $R$  the curvature of the wavefront and  $\varphi$  the so-called Gouy phase. The temporal dependence of the wave has been left out.

Defining the Rayleigh range as  $z_R = \pi\omega_0^2/\lambda$ , the following well-known relations are satisfied:

$$\omega^2 = \omega_0^2 \left[ 1 + \left( \frac{\gamma}{z_R} \right)^2 \right] \quad (3.12)$$

$$R = \gamma \left[ 1 + \left( \frac{z_R}{\gamma} \right)^2 \right] \quad (3.13)$$

$$\varphi = \arctan \left( \frac{\gamma}{z_R} \right) \quad (3.14)$$

Consider also a one-dimensional periodic object of period  $P$ , whose transmission function  $T(x)$  can be described as a Fourier series:

$$T(x) = \sum_n a_n e^{i \frac{2\pi n}{P} x} \quad (3.15)$$

Assuming that the transmission function above acts multiplicatively on the field, the Fresnel diffraction formula can be applied to calculate the field at a distance  $z$  after the object:

$$U_G(x, y, z) \propto \frac{1}{i\lambda z} \iint_{-\infty}^{\infty} e^{-\frac{x'^2+y'^2}{\omega^2}} T(x') e^{i \frac{k(x'^2+y'^2)}{2R}} e^{ik\mathcal{R}} dx' dy' \quad (3.16)$$

where

$$e^{ik\mathcal{R}} = e^{ik \left[ z + \frac{x^2+y^2}{2z} - \frac{1}{z}(xx'+yy') + \frac{x'^2+y'^2}{2z} \right]} \quad (3.17)$$

Here,  $(x', y')$  are the coordinates in the object plane and  $(x, y)$  the coordinates in the observation plane. The full calculation of this integral is given in section A.1 of the appendix. The result is found to be

$$U_G(x, y, z) \propto \sum_n a_n e^{-\frac{4\pi^2 n^2}{k^2 P^2} \cdot \frac{z^2}{\omega_z^2}} e^{\frac{4\pi n}{kP} \cdot \frac{zx}{\omega_z^2}} e^{-i\pi\lambda \frac{n^2}{P^2} M_u z \frac{\omega^2}{\omega_z^2}} e^{i \frac{2\pi n x}{P} M_u \frac{\omega^2}{\omega_z^2}} \quad (3.18)$$

where  $\omega_z$  is the beam radius at the observation plane and

$$M_u = \frac{R+z}{R} \quad (3.19)$$

The first two exponential terms denote amplitude changes along the axial and lateral direction imposed by the object's diffraction orders, and they are not responsible for diffraction image formation. The third exponential, called the localization term, describes the phase changes of diffraction orders with the axial distance  $z$ . Analogously to the condition found in section 3.1 for the Talbot effect, self-images of the periodic object are formed when the following relation is fulfilled:

$$\nu \frac{P^2}{\lambda} = z M_u \frac{\omega^2}{\omega_z^2} \quad (3.20)$$

with  $\nu$  a positive integer, called the self-image number. Note that when  $\nu$  is odd the self-image is shifted laterally by half the object period.

The last exponential term, or magnification term, accounts for the lateral magnification  $M_G$  of the image, which is

$$M_G = \frac{\omega_z^2}{\omega^2} M_u^{-1} \quad (3.21)$$

An interesting special case occurs when the periodic object is located at the beam waist plane ( $\gamma = 0$ ,  $\omega = \omega_0$ ). In this case,  $R \rightarrow \infty$  and the localization and magnification relations become, respectively,

$$z = \nu \frac{P^2}{\lambda} \left( \frac{\omega_z}{\omega_0} \right)^2 \quad (3.22)$$

and

$$M_{G0} = \left( \frac{\omega_z}{\omega_0} \right)^2 \quad (3.23)$$

From the general case one can also find the conditions for uniform illumination, as described in section A.2 of the appendix, and recover the expression of the Talbot effect for plane waves. The difference between self-images under plane-wave and Gaussian beam illumination is that in the latter there exists a lateral magnification due to the properties of the Gaussian beam [39]. Also, for a Gaussian beam the self-image locations and the lateral magnification are dependent on  $z$ , and not in a linear manner.

### 3.2.2 Simulation results

To verify the described effect, we consider a one-dimensional Gaussian beam (see section A.3 in the appendix for its analytical expression) with wavelength of  $\lambda = 623.8 \text{ nm}$  and a beam waist radius of  $\omega_0 = 150 \mu\text{m}$ . This beam is normally incident on a binary amplitude grating of period  $P = 15 \mu\text{m}$  and a 50 % duty cycle, located at the same plane as the beam waist. Figure 3.15 clearly shows that self-imaging occurs at  $\nu = 1$ , including the fact that at this distance the pattern is inverted with respect to the grating's transmission function. No magnification is observed because, for the given parameters,  $M_u \approx 1$ . A comparison between the AS and the Fresnel propagation methods is shown on the right in the same figure, highlighting that in the paraxial approximation the pattern is closer to the square shape of the grating.

As distance increases, the periods lose their square shape and become rounded peaks. Moreover, other terms of the field expression become more significant and separated orders of diffraction appear. As an example, figure 3.16 shows the intensity pattern

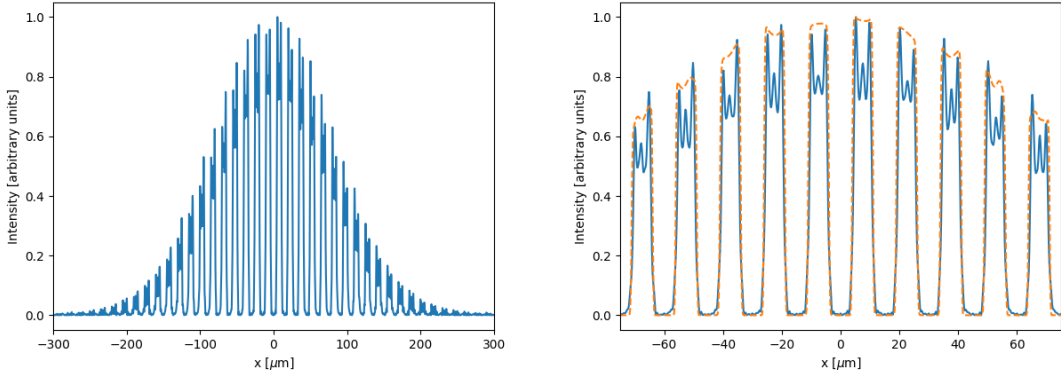


**Figure 3.15:** Self-image of a binary amplitude grating, with period  $P = 15 \mu\text{m}$ , at a distance corresponding to the first self-image plane ( $\nu = 1$ ) from the object, when the grating is placed at the beam waist plane of a Gaussian beam with a wavelength of  $\lambda = 623.8 \text{ nm}$  and a waist radius  $\omega_0 = 150 \mu\text{m}$ . The figure on the right is an amplification of the central region. The field calculated with the Angular Spectrum method (blue) is shown along with the one obtained with the Fresnel approximation (orange). Both patterns have been normalized independently, so their magnitude cannot be compared directly.

at a distance of 10 mm from the grating (for reference, note that the distance that corresponds to  $\nu = 1$  is around 0.36 mm). It is interesting to notice that the ringing that can be observed between the different diffraction orders has the same period as the grating, or more specifically as the expected self-images (this can be checked with the  $\pi$ -phase grating, whose self-images have half the period of the grating). Consequently, this suggests that this ringing is due to the presence of the periodic object and not a numerical issue. Besides, this effect vanishes when the propagation distance is increased, which is consistent with the fact that the exponential terms that affect the amplitude due to diffraction orders gain importance with respect to the terms that account for self-imaging.

As in the case of plane-wave illumination, a similar effect can be seen for phase gratings. When  $\nu$  takes an integer value, the original field intensity is observed, whereas square images occur at fractional values of  $\nu$  according the phase shift and filling factor of the grating. Furthermore, the pattern in the far field for a  $\pi/2$ -phase grating is the same as for the amplitude grating, while for a  $\pi$ -phase grating the zeroth diffraction order is null. The full carpets produced by the field after such gratings is shown in figure 3.17. The parameters used to create this figure have been changed with respect to the ones considered for the amplitude grating, in order to match the resources available at the lab, which will be used to get experimental images in the next section. The new setup consists of a near infrared laser operating at a wavelength  $\lambda = 1.55 \mu\text{m}$ , with a beam waist of  $\omega_0 = 1.6 \text{ mm}$  located at a distance of  $z_0 = 7.26 \text{ mm}$  from the output. The gratings have a period of  $P = 180 \mu\text{m}$  and a 50% duty cycle, and are placed at a distance of 19 cm from the source.

At the near-field, the carpets resemble those obtained with a plane wave as far as the location of the images and their magnification are concerned. The only appreciable difference is the Gaussian modulation. This can be understood by the fact that the

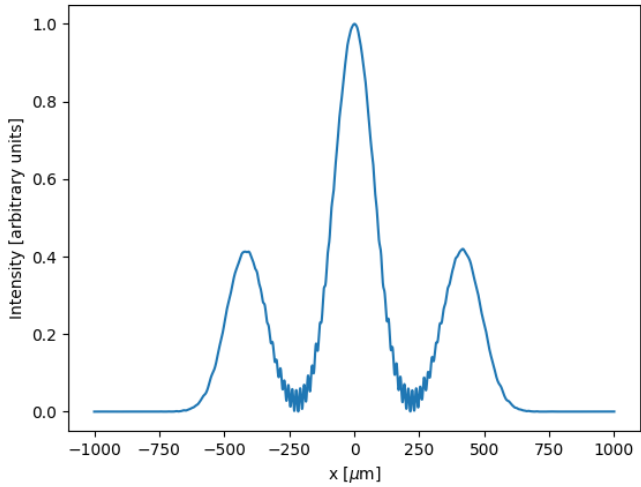


**Figure 3.16:** Intensity pattern in the far-field, at a distance  $z = 10$  mm, from a binary amplitude grating of period  $P = 15 \mu\text{m}$  and duty cycle  $f = 0.5$ , which is illuminated by a Gaussian beam with a wavelength of  $\lambda = 623.8 \text{ nm}$  and a waist radius  $\omega_0 = 150 \mu\text{m}$ .

Rayleigh range of the beam, that is, the distance at which its radius is increased by a factor  $\sqrt{2}$  with respect to the beam waist, is around 5 m, much larger than the distances we are considering. Therefore, the magnification is practically 1. As long as at least three orders interfere, there is still a succession of shifted and non-shifted degenerated Lohmann images. When only two diffraction orders interfere, this effect disappears and a sinusoidal pattern is left. The period of the fringes between the zeroth and first orders in the  $\pi/2$  case is found to be equal to the grating period, whereas for the case of the +1 and -1 orders of the  $\pi$  grating it is half the grating period. This pattern also vanishes eventually and the orders of diffraction become completely separated, leading to the Fraunhofer pattern of the field.

### 3.3 Cone beam and experimental images

We define a cone beam as any beam that expands significantly in the transverse direction as it propagates. In practice, a beam of this kind can be obtained either with an incoherent source or, as we will do in this section, by placing a diverging lens in front of the laser. Recall the setup described towards the end of the previous section, that was used to obtain figure 3.17. Leaving the gratings at the same distance, we place a lens with focal length  $f = -25 \text{ mm}$  at a distance of 4 cm from the laser output. To avoid confusion, from now on the symbol  $f$  will be used to denote the focal distance of a lens and not the duty cycle, which will be assumed to be 50 % unless another value is given explicitly.

Focusing on the near field, the carpets generated by this cone beam are shown in figure 3.18. The main difference between these carpets and the non-diverging case is that the self-images are now found at a further distance than the Talbot length, and the distance between consecutive self-images is not constant [49]. A clear example of this is the fact that the second zero-contrast plane for the  $\pi/2$ -phase grating does not appear in the figure even though it should be found at the

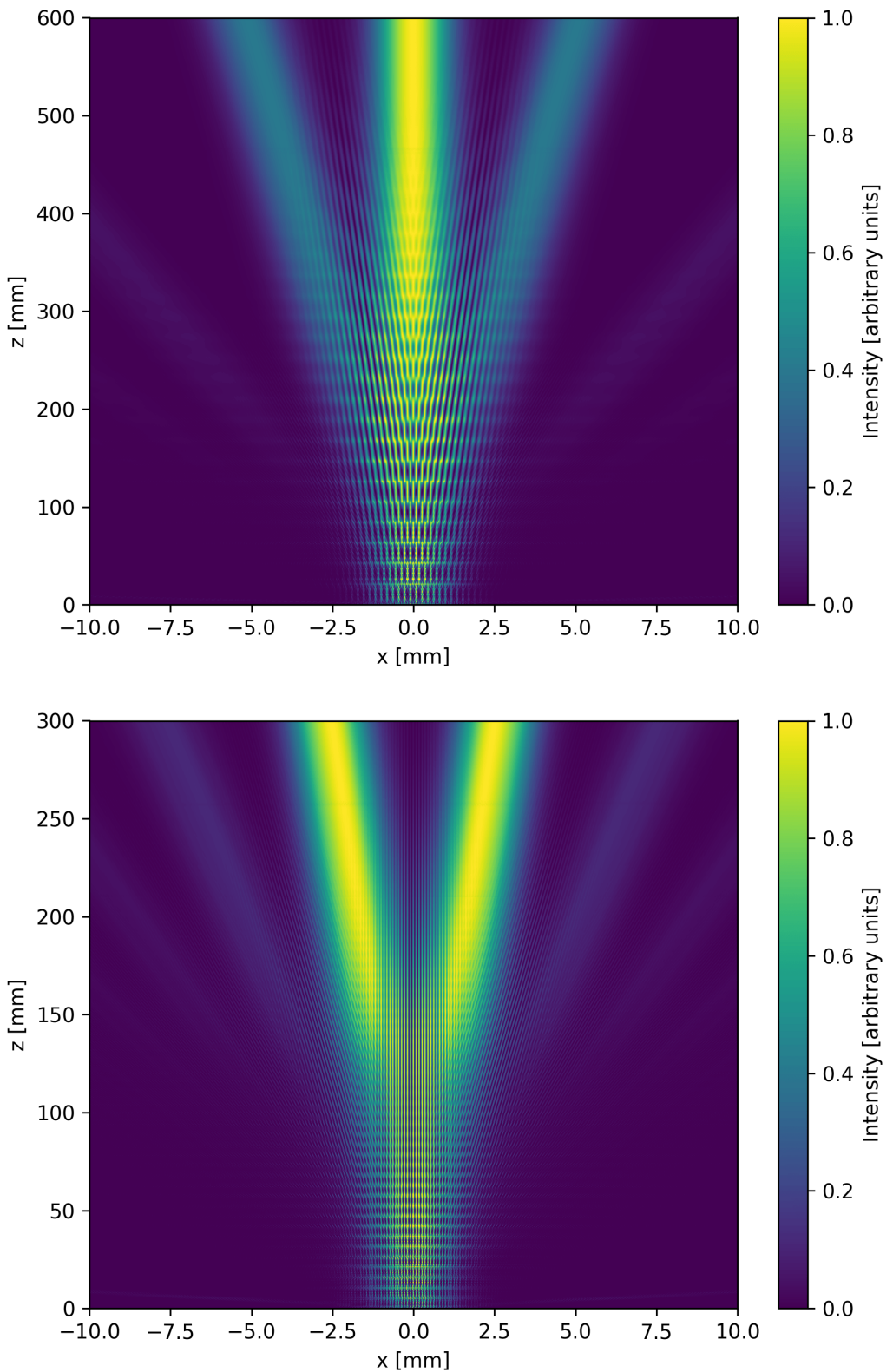


**Figure 3.17:** Full carpet, including near and far-field, after a  $\pi/2$  (top) and a  $\pi$  (bottom) phase-gratings under Gaussian beam illumination. The gratings' period is  $P = 180\text{ }\mu\text{m}$  and their duty cycle  $f = 0.5$ . They are placed at a distance of 19.7 cm from the waist plane of a beam with a wavelength of  $\lambda = 1.55\text{ }\mu\text{m}$  and a waist radius of  $\omega_0 = 1.6\text{ mm}$ .

Talbot distance, which is approximately  $Z_T = 41$  mm. Furthermore, the period of the Lohmann images also increases with the propagation distance after the grating. Another interesting conclusion that is extracted from the simulations is that there is no sign of order separation effects for this particular beam. This was checked considering a computation window of 60 mm around the center of the beam, and a maximum distance from the grating of 1 m.

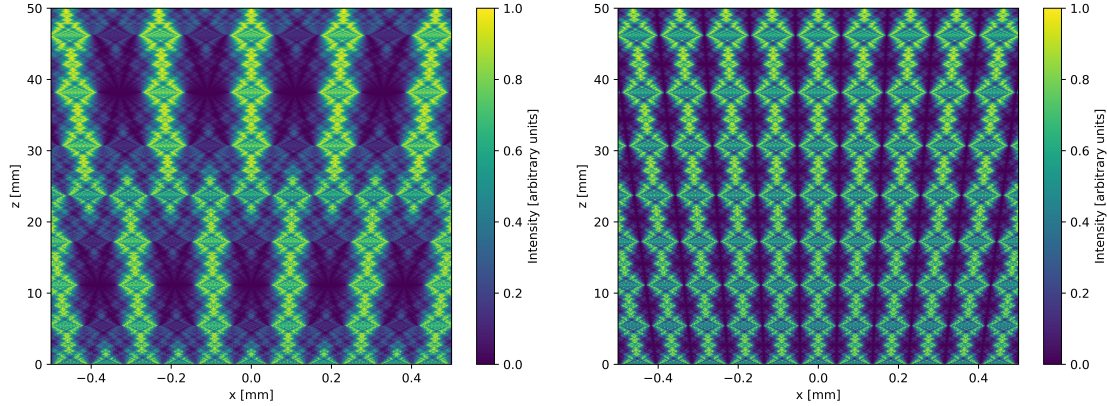


**Figure 3.18:** Carpet produced by the field after a  $\pi/2$  (left) and a  $\pi$  (right) phase gratings illuminated with a divergent Gaussian beam. The beam is generated with a near infrared laser ( $\lambda = 1.55 \mu\text{m}$ ), and then goes through a diverging lens with focal distance  $f = -25 \text{ mm}$  placed 4 cm behind the source. The corresponding grating, whose period is  $P = 180 \mu\text{m}$  in both cases, is located at a distance of 15 cm from the lens.

The setup was built at the lab, using as a detector a  $1296 \times 964$  pixel camera with a pixel size of  $3.75 \mu\text{m}$ , which corresponds to a total camera size of  $4.86 \text{ mm} \times 3.615 \text{ mm}$ . The pattern at the camera was obtained for various distances from the grating, while keeping the distance between the lens and the grating constant at 15 cm. A couple of examples using a  $\pi/2$ -phase grating are shown in figure 3.19, along with the corresponding two-dimensional simulated images. The self-imaging phenomenon was also verified for a  $\pi$ -phase grating.

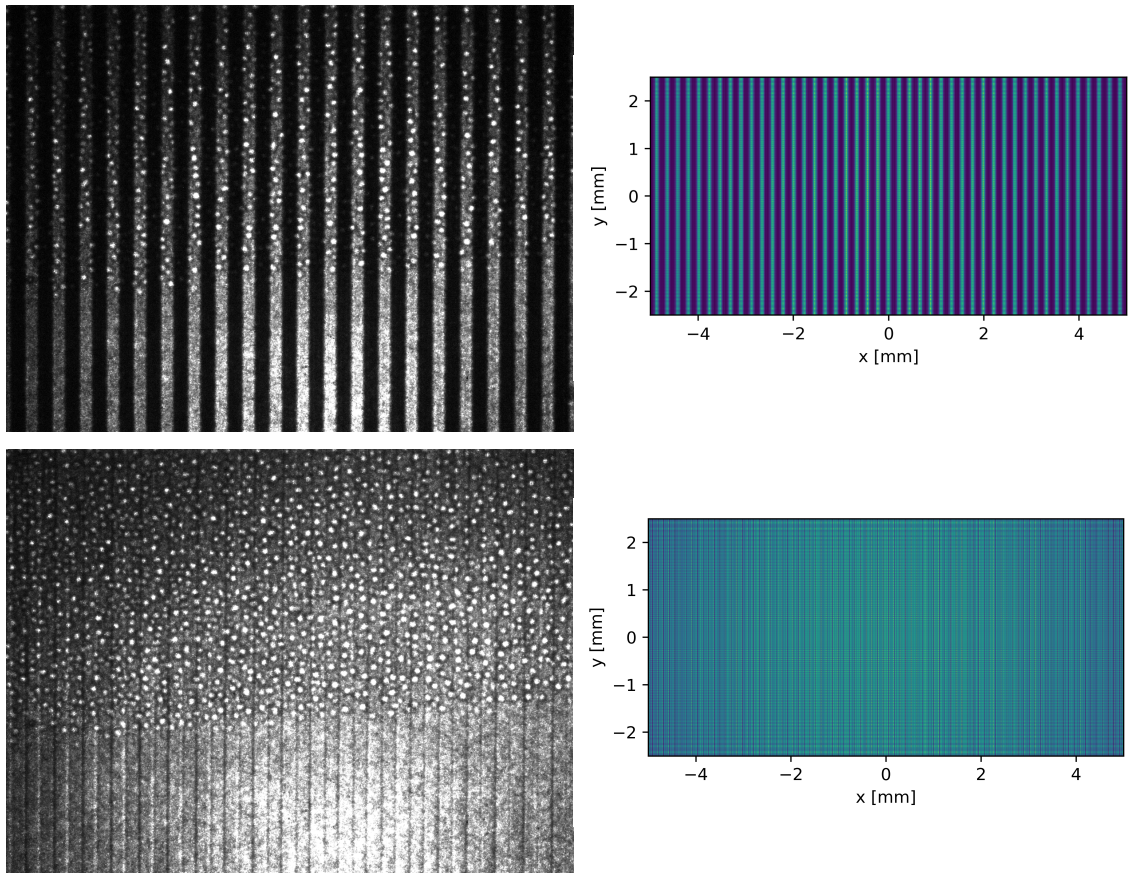


**Figure 3.19:** Experimental (left) and two-dimensional simulated images (right) after a  $\pi/2$ -phase grating illuminated by a cone beam. The images correspond to a distance from the grating of 4 cm (top) and 5.5 cm (bottom). The grating period is  $180 \mu\text{m}$ , and the beam is a Gaussian beam with a wavelength of  $\lambda = 1.55 \mu\text{m}$  magnified by a diverging lens of focal  $f = -25 \text{ mm}$ . In the experimental images, brighter areas correspond to a higher field intensity, although the camera's response is not linear with intensity. The white dots in the experimental images are due to an issue in the sensor and thus should be ignored. Even though the images are not to scale, it was verified that their periods match.

# Chapter 4

## Optical wave interferometry

The effects described in the previous chapter constitute the basis for grating interferometry. In this chapter, the basic design relying on the Talbot effect is introduced, and practical applications of the technique are briefly discussed. Next, a design based on the more general moiré effect between two gratings is presented, and later extended to the case of three gratings. This effect occurs when two transmission gratings with slightly different periods or orientation are overlapped. As a result, a wavelike interference pattern can be seen [50]. An analogous effect was demonstrated with two transparent phase masks [24], which allows for an interferometer design without the need for absorption gratings. We reproduce numerically published results using this design, as well as provide experimental evidence.

### 4.1 Talbot interferometer

A simple interferometer design based on the Talbot effect was presented by Lohmann and Silva [51] and, independently, by Yokozeki and Suzuki [50]. It consists of a collimated laser beam (which can be regarded as a plane wave) that is incident on an amplitude grating. Before or after this first grating a phase object is placed, which deforms the field. The displacement of the field is detected right after a second amplitude grating located ideally at a half-integer multiple of the Talbot length from the first one, where the fringes it produces have maximum contrast.

A modification of this design was proposed by Ibarra and Ojeda-Castañeda [52]. In their design, two identical amplitude gratings ( $G_1$  and  $G_2$ ) with a 50 % duty cycle are separated by a distance of  $Z_T/2$ , being  $Z_T$  the Talbot distance. The phase object is placed halfway between them, whereas the camera is set a fourth of the Talbot distance behind the second grating.

The fundamental idea is that an amplitude grating with a filling factor of 0.5 produces a constant field at a distance of  $Z_T/4$  behind it. Even if the grating's duty cycle is not ideal, the contrast will still be very low, so the object receives a practically uniform illumination. If no object is present, the second grating will completely block out the light, since it is placed at the distance where the shifted Talbot image of the first grating is formed. Similarly, in the absence of the first grating and an object, the second grating produces a uniform field at the detection plane.

When an object with a phase gradient is placed between the two gratings, the negative self-image of  $G_1$  will be laterally displaced and  $G_2$  will no longer block out the light. For a constant gradient, the displacement is also constant. Considering a displacement equal to  $\epsilon P$ , with  $0 \leq \epsilon \leq 1$  and  $P$  the period of the gratings, the intensity pattern of the field immediately after the second grating will resemble that of an amplitude grating with an opening ratio  $s$  given by

$$\begin{aligned} s &= \epsilon, && \text{if } 0 \leq \epsilon \leq 0.5 \\ s &= 1 - \epsilon, && \text{if } 0.5 \leq \epsilon \leq 1 \end{aligned} \quad (4.1)$$

Therefore, according to the Talbot effect the intensity pattern at the detection plane should also be that of a binary amplitude grating, as long as  $0 < \epsilon < 0.5$  and  $0.5 < \epsilon < 1$ . As for the remaining cases, one should see a uniform bright field if  $\epsilon = 0.5$  and a uniform dark field if either  $\epsilon = 0$  or  $\epsilon = 1$ .

In order to check this last statement, we will simulate the system for a plane wave with a wavelength of  $\lambda = 632.8 \text{ nm}$  and two gratings of period  $P = 317.5 \mu\text{m}$ . The Talbot distance for these parameters is  $Z_T = 31.86 \text{ cm}$ . Let us consider a transparent object with a constant phase gradient (i.e. a prism), whose transmission function is given by

$$T(x) = e^{-ix\phi} \quad (4.2)$$

where  $\phi$  is a constant. The beam angular deflection  $\alpha$  produced by this object is [53]:

$$\alpha = \frac{\lambda}{2\pi} \frac{\partial \varphi(x)}{\partial x} = -\frac{\lambda}{2\pi} \phi \quad (4.3)$$

From this expression we can easily find the distance by which the beam will be displaced when it reaches the second grating:

$$\epsilon P = \frac{Z_T}{4} \cdot \frac{\lambda}{2\pi} \phi \quad (4.4)$$

where we have considered that  $\phi \ll 1/\lambda$ , and therefore  $\tan(\alpha) = \alpha$ . Also, at this point the sign can be ignored since it only determines to which direction the beam is deflected. According to the Talbot effect, the pattern at the detector should be that of a binary transmission grating with a duty cycle of  $2s$ . Therefore, in principle, if we measure the duty cycle of the image we can recover  $\epsilon$  and relate it to  $\phi$ , thus allowing us to measure the phase gradient of the object.

To obtain the duty cycle of the intensity pattern at the detector, we can fit to it a rectangular pattern of the same period as the grating, where the free parameters to be optimized are its amplitude, duty cycle and lateral position. Notice that for this kind of function the gradient methods that are most commonly used for fitting purposes cannot be applied, since the derivative at the end of each half-period is infinite. As an alternative, we can use stochastic methods such as Differential Evolution [54]. The pattern amplitude and duty cycle obtained with this method for an object with a constant phase gradient is shown in figure 4.1.

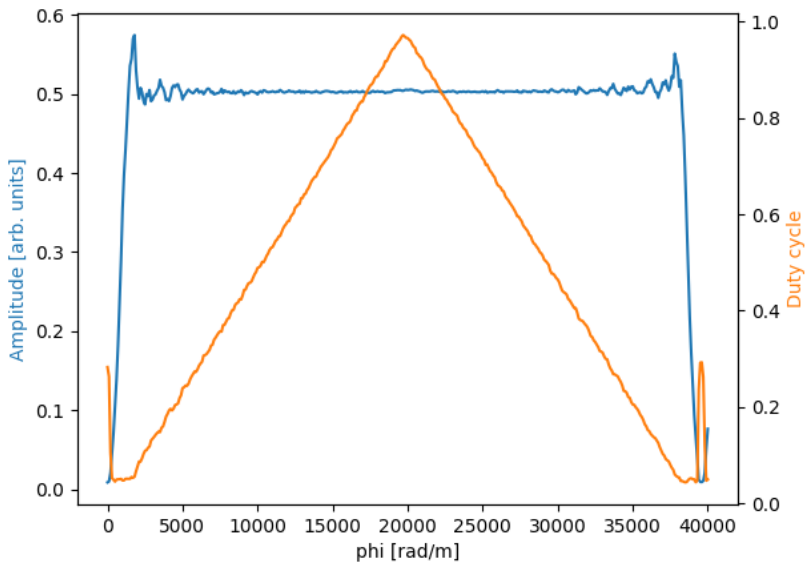


**Figure 4.1:** Amplitude and duty cycle of the intensity pattern after a Talbot interferometer, when an object with a linear phase is placed between the gratings. The horizontal axis corresponds to the constant phase gradient  $\phi$  of the object. The parameters are obtained by fitting a rectangular function to the intensity pattern at the observation plane. The system is composed of two identical binary transmission gratings, with period  $P = 317.5 \mu\text{m}$ , that are illuminated by a plane wave of wavelength  $\lambda = 632.8 \text{ nm}$ .

The linear relation between the pattern's duty cycle and the phase gradient is clearly rendered visible. However, some limitations of the method are also exposed. First, the duty cycle observed when no object is placed in the system is not zero, but rather its value is arbitrary due to the practically null amplitude. Even as the amplitude increases, the duty cycle does not increase linearly for low values of  $\phi$ . Second, the contrast when  $\epsilon = 0.5$  ( $\phi \approx 20\,000 \text{ rad/m}$ ) is low but not zero, and so the duty cycle does not quite reach the expected value of 1. Third, the patterns are not exactly rectangular, so the fit is not perfect. These issues arise from the fact that the theoretical analysis of this design considers an infinite plane wave in the Fresnel approximation, and neither of these are completely accurate.

To exemplify this, consider a phase object with  $\phi = 20\,000 \text{ rad/m}$ . With this gradient, the pattern at the detector should be approximately constant. The result is shown on the left in figure 4.2, where the fit returns a duty cycle of  $dc = 0.9652$ . If we use the Fresnel formula instead of the Angular Spectrum to perform the calculations, the new duty cycle is  $dc' = 0.9862$ . Furthermore, the fluctuations are greatly reduced.

Since we are particularly interested in applications for precision measurements, we can try use this interferometer to measure the phase gradient of the object. As an example, we will use an object with  $\phi = 5\,000 \text{ rad/m}$ , which produces the pattern in the detector shown on the right in figure 4.2. Assuming that we know that the displacement of the field is less than half the grating period, so  $s = \epsilon$  and  $dc = 2s$ , the gradient of the object is related to the duty cycle of the output pattern as follows:

$$\phi = \frac{4\pi P}{Z_T \lambda} \epsilon \quad (4.5)$$

We have run the simulation to obtain the intensity, and then fit the rectangular pattern to the result. Since the fitting is stochastic, it has been executed 10 times in order to minimize the statistical error. We have obtained that the duty cycle is  $dc = 0.2367$ , with a standard deviation of  $\sigma = 0.0005$ . From this value, the measured phase gradient from the object is found to be  $\phi' = 4684 \text{ rad/m}$ , hence giving a relative error from the actual value of 6.32 %. Notice that the fit itself is a possible cause for this error, since the pattern is not exactly square but rather slightly trapezoidal. Therefore, from this result we conclude that it is possible to recover the original phase, but not accurately, and certainly not if the phase gradient is small. Moreover, this requires certain assumption on the displacement of the field, which would have to be checked by other means.

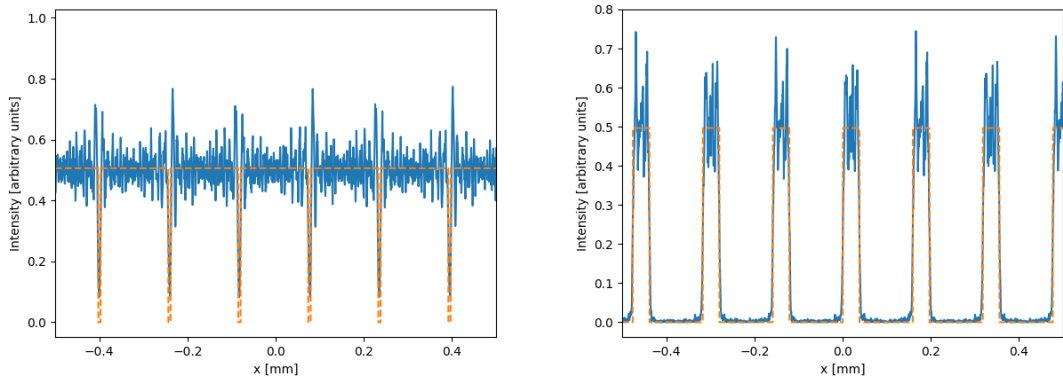


**Figure 4.2:** Intensity pattern (solid blue line) after the Talbot interferometer for a transparent object with a linear-phase object, with a constant phase gradient of  $\phi = 20000 \text{ rad/m}$  (left) and  $\phi = 5000 \text{ rad/m}$  (right). The dashed orange line shows the fitted square pattern. The period of the gratings is  $P = 317.5 \mu\text{m}$ , and the wavelength of the incident plane wave is  $\lambda = 632.8 \text{ nm}$ .

Another characteristic of this interferometer regarding practical applications is that it can be used together with an imaging system. This device, presented also in ref. [52], consists of a lens with a focal length  $f$  placed at a distance of  $2f$  from the object, which creates a sharp image of its phase structure. At the Fourier plane after the lens, which corresponds to its focal, a narrow slit acts as a spatial filter to select only one diffraction order from the gratings. This also allows to distinguish between phases that produce displacements more than one period apart.

As an example, consider an object with a linear phase in the central region, for instance a gradient of  $\phi = 10000 \text{ rad/m}$  between  $x = -2 \text{ cm}$  and  $x = 2 \text{ cm}$ , and a constant phase shift at the edges. Its phase profile is depicted in figure 4.3. Using a lens of  $f = 25 \text{ cm}$ , the pattern at its focal plane is shown in figure 4.4. The different peaks that are seen correspond to the contribution of the different diffraction orders from the lens. We select the higher peak by means of a slit with width  $w = 0.05 \text{ cm}$  centered at  $x_0 = -0.25 \text{ mm}$ .

The image obtained after this setup is shown in figure 4.5. As we expected, it shows a null intensity at the edges, where the phase of the object is constant, while in

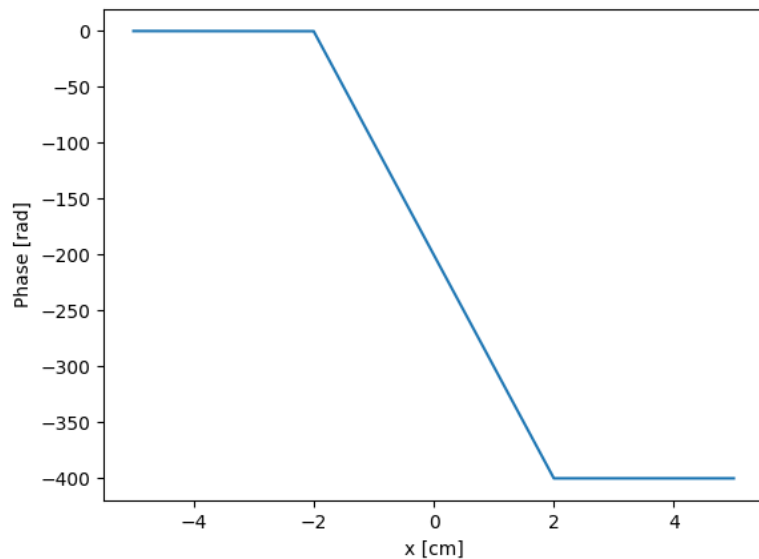


**Figure 4.3:** Phase profile of the object under test for the Talbot interferometer imaging device. The gradient in the central region of the object is constant and equal to  $\phi = 10\,000 \text{ rad/m}$ .

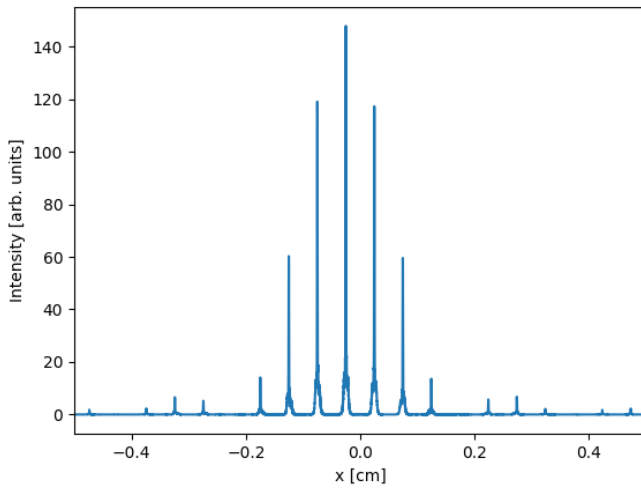


**Figure 4.4:** Intensity pattern produced by the object under test at the focal plane of the lens in the Talbot interferometer imaging system. The gratings that were used had a period of  $P = 317.5 \mu\text{m}$ , and were illuminated by a plane wave of wavelength  $\lambda = 632.8 \text{ nm}$ . The lens' focal length is  $f = 25 \text{ cm}$ .

the central region it remains constant at a certain value. The same pattern can be seen whatever the (constant) gradient of the object is, as long as the filter is placed accordingly and the displacement of the beam is not a multiple of the period. In the latter case, the light field would be completely blocked by the grating. With this example the basic idea behind this imaging system is demonstrated. Application to objects with a more complex phase structure is possible, according to the reference. However, it is not trivial and also not of great interest for this project, so we will not explore the idea further.

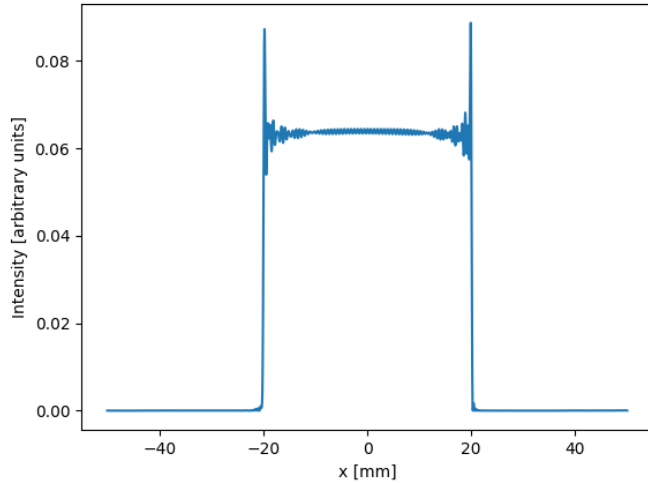


**Figure 4.5:** Image of the object under test obtained with the Talbot interferometer imaging system. The image corresponds to the intensity pattern at the observation plane, located at a distance of  $2f$  from the lens, being  $f$  its focal length. The system consists of two gratings with period  $P = 317.5 \mu\text{m}$ , illuminated by a plane wave of wavelength  $\lambda = 632.8 \text{ nm}$ . The output is filtered by means of a lens with  $f = 25 \text{ cm}$  and a slit of width  $w = 0.05 \text{ cm}$  properly placed to choose only the desired order of diffraction from the gratings.

The Talbot interferometer has been widely used in literature for imaging applications, with a special interest in the X-ray range. Some minor modifications have been applied, including the use of a phase grating instead of an absorption one for the first grating [55] and the so-called Talbot-Lau configuration [53, 56], which consists on adding an absorption grating in front of the source to reduce the coherence requirements. In either case images are usually obtained using phase stepping techniques [55]. Despite having proven useful in many situations, this design has some flaws when it comes to precision measurements of small phase gradients, so we need an interferometer with a higher sensitivity.

## 4.2 Two phase-grating moiré interferometer

The two phase-grating moiré interferometer (2PGMI) [24] is similar to the Talbot interferometer from a structural point of view, since it makes uses of two gratings that are placed close to each other. However, the working principle is different. Instead of having to match the (possibly fractional) self-image of the first grating in

order to analyze it, the period of the second grating is now required to be slightly larger (or smaller) than the period of the first one. Then, the pattern produced after the first grating interferes with the second grating and moiré fringes are generated. Alternatively, one can use a cone beam and two gratings with the same period, so that the pattern from the first grating is magnified at the plane of the second, and as a result their period is effectively different. This effect can be observed both with transmission and phase gratings, with different requirements. For practical reasons, the case of interest for us is that of two phase gratings.

#### 4.2.1 Theoretical description

A brief description of the fringes produced by the moiré effect is presented below, following the derivation in ref. [24]. The full theoretical development and additional considerations are provided in section C.1 of the appendix.

Consider two infinite periodic gratings  $G_1$  and  $G_2$ . Their transmission functions  $T_1$  and  $T_2$  can be written as a Fourier Series:

$$T_1(x_1) = \sum A_m e^{i2\pi m f_1 y_1} \quad (4.6)$$

$$T_2(x_2) = \sum B_n e^{i2\pi n f_2 y_2} \quad (4.7)$$

where  $y_1$  and  $y_2$  are the coordinates in the plane of  $G_1$  and  $G_2$ , respectively, and  $f_1$  and  $f_2$  the spatial frequencies of the gratings. Assuming that the source is a point source and considering only the paraxial region, the solution of the corresponding Fresnel integral is:

$$V(x) \propto e^{ikL/\cos\theta} \sum_{m,n} A_m B_n e^{i\phi_0(m,n) + i\phi_1(m,n)} \quad (4.8)$$

where  $\theta$  is the elevation angle of the line connecting the source to point  $y$  in the observation plane, and  $\phi_0$  and  $\phi_1$  are given by

$$\phi_0 = 2\pi m f_1 \left( \frac{L_1}{L} y + \frac{D+L_2}{L} y_s \right) + 2\pi n f_2 \left( \frac{L_1+D}{L} y + \frac{L_s}{L} y_s \right) \quad (4.9)$$

$$\phi_1 = -\frac{L}{2k} \left[ (2\pi m f_1)^2 \frac{L_1}{L} + (2\pi n f_2)^2 \frac{L_2}{L} - \left( 2\pi m f_1 \frac{L_1}{L} - 2\pi n f_2 \frac{L_2}{L} \right)^2 \right] \quad (4.10)$$

Considering the phase difference between the terms  $A_m B_n$  and  $A_{m+1} B_{n-1}$ , their contribution to the intensity distribution at the observation plane is then found to be:

$$H_1 \propto e^{i\left(\frac{2\pi y}{P_d} - \frac{2\pi y_s}{P_s}\right)} \sum_m A_m A_{m+1}^* e^{i2\pi(m+1/2)\delta_1} \sum_n B_n B_{n-1}^* e^{-i2\pi(n-1/2)\delta_2} \quad (4.11)$$

with

$$\delta_1 = \frac{\lambda}{L} f_1 L_1 [(f_1 - f_2)L_2 + f_1 D] \quad (4.12)$$

$$\delta_2 = \frac{\lambda}{L} f_2 L_2 [(f_2 - f_1)L_1 + f_2 D] \quad (4.13)$$

$$P_s = \frac{L}{(f_1 - f_2)L_2 + f_1 D} \quad (4.14)$$

$$P_d = \frac{L}{(f_2 - f_1)L_1 + f_2 D} \quad (4.15)$$

The coefficients  $\delta_j$  are the correlation distances for the  $j$  grating and  $P_s$  is the source period. The meaning of this coefficients is discussed in the appendix. As for the last one, the complex exponential  $\exp(i2\pi y/P_d)$  implies the existence of an achromatic oscillating pattern with period  $P_d$  in the observation plane, which corresponds to the moiré effect.

Furthermore, defining

$$\chi_1(\delta_1 P_1, f_1) = \sum_m A_m A_{m+1}^* e^{i2\pi(m+1/2)\delta_1} \quad (4.16)$$

$$\chi_2^*(\delta_2 P_2, f_2) = \sum_n B_n B_{n-1}^* e^{-i2\pi(n-1/2)\delta_2} \quad (4.17)$$

one can get a closed expression for the contrast of those fringes. Considering the case of a coherent, monochromatic beam, the contrast is given by:

$$C = 2 \frac{|\chi_1(\delta_1 P_1, f_1)|}{\langle T_1 T_1^* \rangle} \frac{|\chi_2^*(\delta_2 P_2, f_2)|}{\langle T_2 T_2^* \rangle} \quad (4.18)$$

where  $\langle T_j T_j^* \rangle$  is the intensity transmission of the grating  $j$ , which for a pure phase grating is equal to 1. The extension of this formula to extended and polychromatic sources is also discussed in the appendix (see section C.1.2).

## 4.2.2 Experimental and simulation results

### Coherent beam

To confirm the validity of our simulation, a moiré interferometer has been built in the lab using two phase gratings. The source system remains the same that was used to generate a cone beam in section 3.3: a Gaussian beam emitted by a near-infrared laser, which can be considered monochromatic at a wavelength of  $\lambda = 1.55 \mu\text{m}$ , is propagated a distance  $L_0 = 4 \text{ cm}$  to a diverging lens with focal length  $f = -25 \text{ mm}$ . The first grating is placed at a distance of  $L_1 = 15 \text{ cm}$  after the lens, and behind it we add a second grating. Both gratings are identical  $\pi/2$ -phase gratings with a period of  $P = 180 \mu\text{m}$ . For now, the grating separation is fixed at  $D = 20 \text{ mm}$ . The existence of the moiré fringes is clear from the carpet after the second grating, shown in figure 4.6.

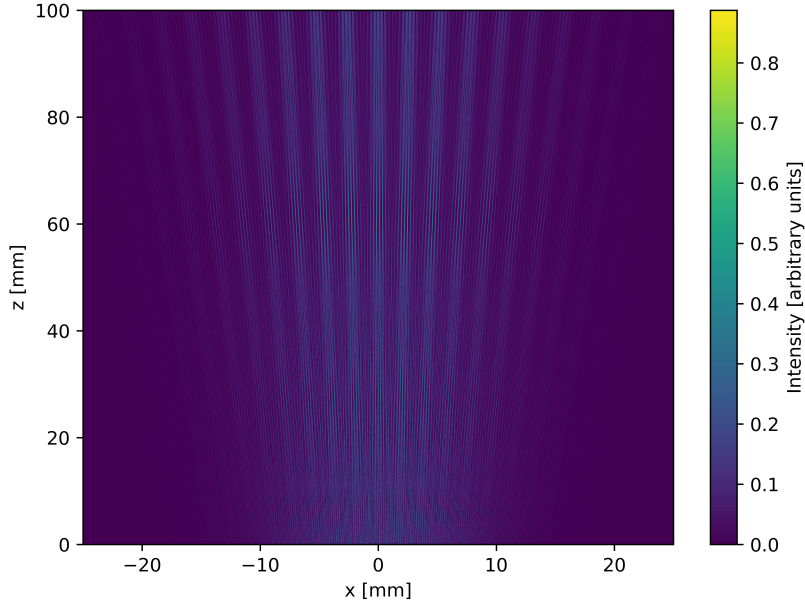


**Figure 4.6:** Carpet after the second grating in the 2PGMI. The simulated system consists of a Gaussian beam of wavelength  $\lambda = 1.55 \mu\text{m}$  that goes through a diverging lens of focal length  $f = -25 \text{ mm}$ . Two  $\pi/2$ -phase gratings are used, both with a period of  $P = 180 \mu\text{m}$ . The first one is placed at 15 cm from the lens, and the second 20 mm behind it. The  $z$  axis corresponds to the distance from the second grating.

Some images have been taken at various distances after the second grating, a couple of which are shown in figure 4.7 along with the corresponding two-dimensional simulations. One can clearly see the oscillating pattern caused by the moiré effect, whose period in this case is around  $P_d \approx 2.5 \text{ mm}$ , which is in agreement with the formula presented in the previous section. Notice that the moiré oscillations are not seen as clear sinusoidal fringes, but rather as a modulation of a more complex pattern consisting in different contributions from various frequency terms. Usually, the effective Talbot frequency from the first grating is the most dominant (as it occurs in the bottom images of the figure), although sometimes other frequency terms also play an important role.

The main figure of merit in the 2PGMI is the contrast of the fringes at the camera, as well as their frequency, both of which greatly depend on the grating separation  $D$ . In order to check their relation, we will consider a new arrangement of the current setup. The laser source and the gratings remain the same, but now we use a lens with focal length  $f = -75 \text{ mm}$ . This lens is placed in front of the laser output, at a distance of  $L_0 = 11 \text{ cm}$ . The first grating is set at a distance of  $L_1 = 98 \text{ cm}$  after the lens, whereas the camera is fixed at  $L = 2 \text{ m}$  measuring also from the lens. The second grating will be translated along the propagation axis.

Due to the fact that the moiré fringes are not isolated, it can be quite complicated to extract their contrast and frequency, especially in low-contrast regions. In order to do that, we have tested a couple of different methods. Assuming that the pattern consists of some high-frequency fringes (coming from the first grating) modulated by a lower frequency oscillation (corresponding to the moiré effect), we can get this modulation by fitting a sinusoidal function to the peaks of the pattern. This fails

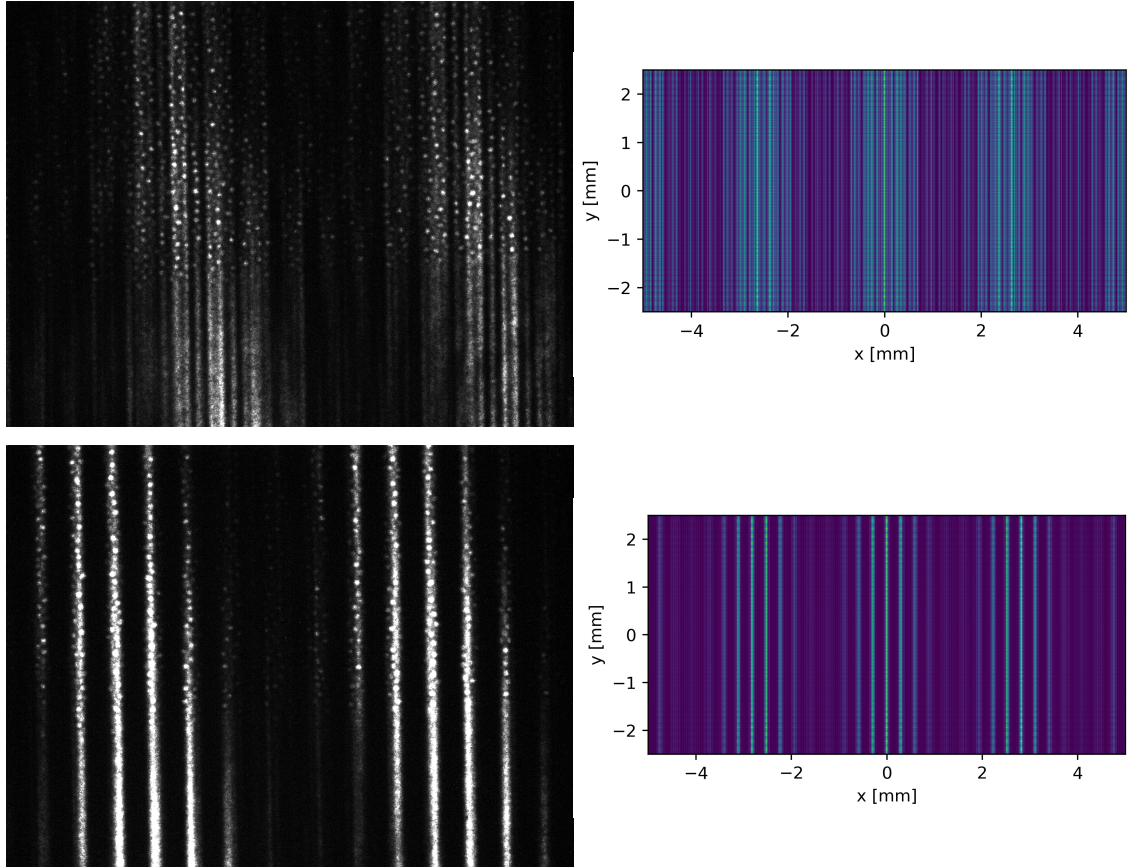


**Figure 4.7:** Experimental (left) and two-dimensional simulated images (right) after the 2PGMI, at a total distance from the source lens of 26 cm (top) and 28 cm (bottom). The setup consists of a near-infrared laser, operating at a wavelength of  $\lambda = 1.55 \mu\text{m}$ , whose output beam is magnified by a lens of focal length  $f = -25 \text{ mm}$ . Two  $\pi/2$ -phase gratings are placed 15 cm behind the lens, separated by a distance of 20 mm. A brighter color in the images means a higher intensity of the field. The white dots in the experimental images are due to an issue in the sensor and should be ignored. In the bottom images, the higher-frequency oscillations correspond to the effective Talbot frequency from the first grating.

easily if the pattern is not smooth enough, for example due to noise or when other frequency terms gain importance. An alternative is to use the Fourier Transform method, which is explained in appendix B. However, its accuracy is dependent on the sampling frequency space of the FFT, and therefore and the size of the measured field. For this reason, fit methods are preferred whenever possible.

The contrast of the recorded experimentally with this configuration is shown in figure 4.8, together with the analytical and numerical results. The contrast is calculated in the simulation via FFT, providing proper results except in low contrast regions. The error is, for the most part, directly related to the frequency resolution of the FFT. On the other hand, the experimental contrast is obtained by fitting the peaks of the pattern to a sine. The frequency is not shown, but it agrees reasonably well with the expected value, at least in the high contrast regions. In this case, the error can be attributed to multiple factors, including imperfect alignment of the gratings (and limited precision in the distance measurements), the non-linearity of the camera sensor with respect to the field intensity and, most importantly, the inaccuracy of the method used to measure contrast. However, we can see that the main peaks are properly defined, and the existence of the moiré effect is thus verified.

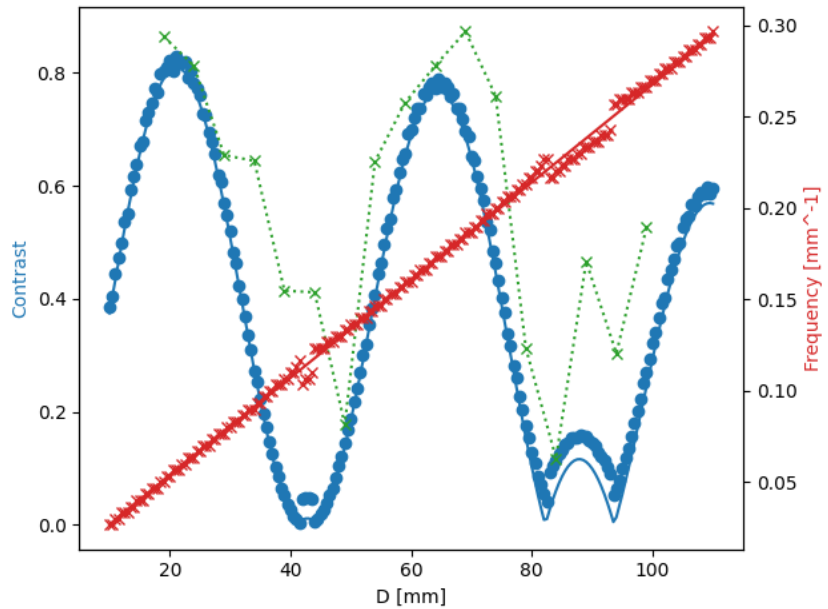


**Figure 4.8:** Contrast and frequency of the moiré fringes in the 2PGMI with respect to the grating separation, for a coherent beam. In red, the solid line is the analytical frequency, while the crosses are the simulation results. Analogously, the blue line is the theoretical contrast and blue dots are the contrast measure from the simulations. The green crosses show the experimental contrast result, and the dotted line that joins them is added for clarity. The images have been obtained using two  $\pi/2$ -phase gratings with a period of  $P = 180 \mu\text{m}$ , illuminated with a Gaussian beam emitted by a near-infrared laser at a wavelength of  $\lambda = 1.55 \mu\text{m}$  and later magnified by a diverging lens with focal length  $f = -75 \text{ mm}$ . The first grating and the camera are fixed at a distance of  $L_1 = 32 \text{ cm}$  and  $L = 2 \text{ m}$  from the lens, respectively. The second grating is translated along the propagation axis, with  $D$  being its separation from the first one.

## Incoherent beam

To test the interferometer design when an incoherent beam is used, we will reproduce numerically the results provided in ref. [24]. The system consists of two (approximately)  $\pi/2$ -phase gratings with period  $P = 14.3 \mu\text{m}$ . An extended, polychromatic source is set at a distance  $L = 20 \text{ cm}$  from the camera, while the gratings are placed midway between them. For the simulations we will consider that the first grating is fixed at  $L_1 = 10 \text{ cm}$  from the source, while the second grating is movable. The source size is  $s_w = 0.44 \text{ mm}$ .

The beam spectrum can be found in the *Supplementary information* of the reference. In broad terms, it consists of a narrow peak at a wavelength of 450 nm and a wider peak at 550 nm. Based on our simulations, we believe that the first peak was filtered out in the experiment, while we get the most similar results considering only the second peak. Therefore, we approximate the spectrum with the probability density function of a skewed normal distribution:

$$f(\lambda) = \frac{2}{\omega\sqrt{2\pi}} e^{-\frac{(\lambda-\xi)^2}{2\omega^2}} \int_{-\infty}^{\alpha(\frac{\lambda-\xi}{\omega})} \frac{1}{\sqrt{2\pi}} e^{-\frac{t^2}{2}} dt \quad (4.19)$$

where  $\xi$ ,  $\omega$  and  $\alpha$  are called the location, scale and shape parameters, respectively. In our case, we use  $\xi = 500 \text{ nm}$ ,  $\omega = 100 \text{ nm}$  and  $\alpha = 5$ , along with an appropriate global scaling factor. The spectrum resulting from this distribution is shown in fig. 4.9. Additionally, to account for the incoherence, the source is modelled as a set of plane waves propagating in different directions, limited by a slit of size  $s_w$ .

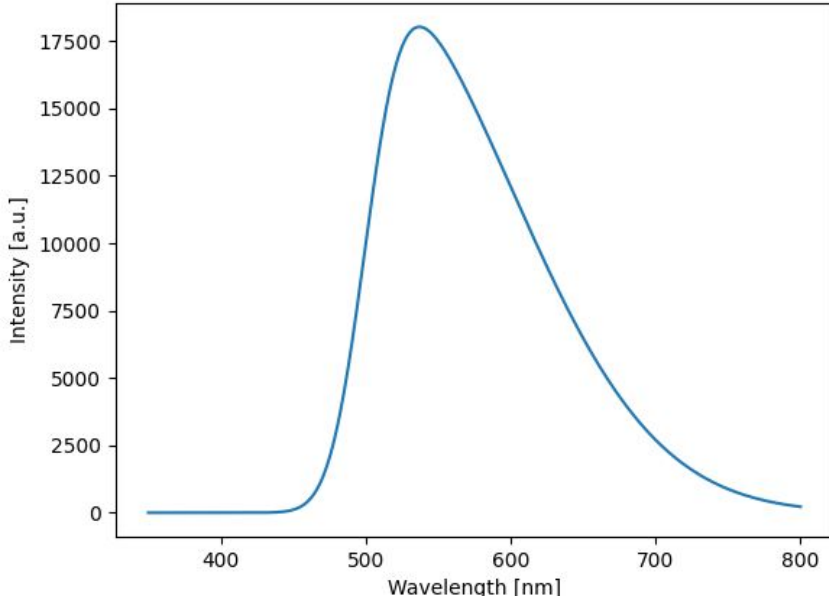


**Figure 4.9:** Spectrum used for the simulation of the 2PGMI for an incoherent beam

The results of the simulation can be found in figure 4.10 in terms of the contrast and frequency of the moiré fringes, compared to their analytical expected values. Opposite to what happened for the case of a coherent, monochromatic source, the patterns obtained at the observation plane do resemble sinusoidal functions, and therefore the measurements can be properly done by fitting a sine to the data.

Moreover, the simulations show that the decrease in contrast as  $D$  increases is caused by the extended size of the source, while the effect of the beam being polychromatic is that the amplitude of the contrast oscillation is reduced.

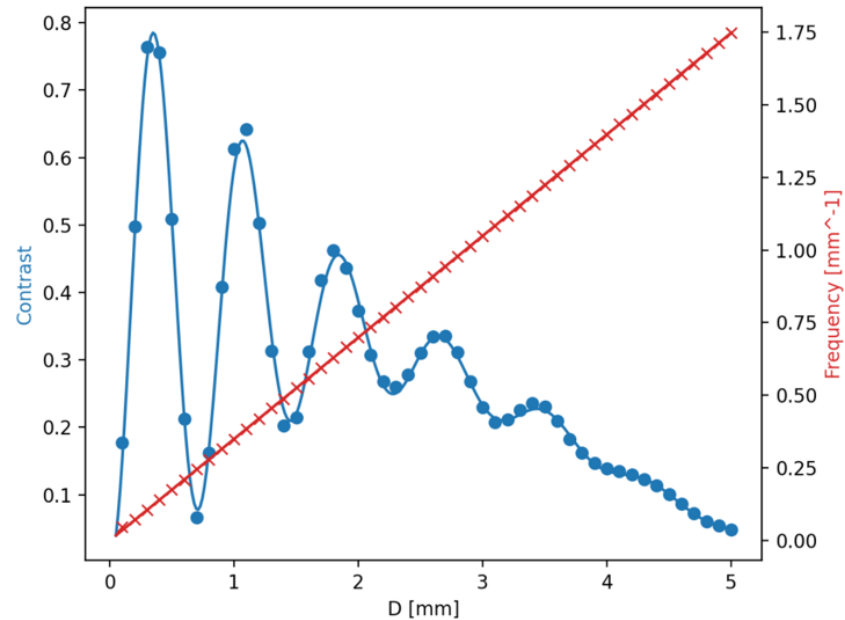


**Figure 4.10:** Contrast and frequency results for the simulation of the 2PGMI with respect to the grating separation, for an incoherent and polychromatic beam. Solid lines show the analytical results, while markers correspond to the simulation. The interferometer consists of two  $\pi/2$ -gratings with a period of  $P = 14.3 \mu\text{m}$ , illuminated by an incoherent beam coming from an extended source, whose spectrum is given by a skewed normal distribution centered around  $\lambda = 550 \text{ nm}$ .

There are a few conclusions that can be extracted for the figure above. First, we can confirm that the simulation method we present is valid and performs well for this system. Second, the phase-grating moiré interferometer provides good results with wide light, meaning that it can work with wide wavelength distributions, at least in theory (assuming that the gratings act similarly throughout the range of wavelengths). Last, the frequency of the moiré fringes increases linearly with the grating separation, which is affected by the maximum resolution of the detectors. Consequently, this design is limited only to small grating separations.

### 4.3 Three phase-grating moiré interferometer

An extension of the moiré interferometer consists in using three gratings instead of two (three phase-grating moiré interferometer, 3PGMI), which allows for larger distances between the gratings, consequently making it easier to place phase objects to image as well as increasing the sensitivity to weak phases. To explain how the system works and, more precisely, what fringes can be seen at the camera, a couple of assumptions are made regarding the second gratings. First, the distance between the first two gratings is considered to be significantly large. Second, the second grating must have a null zeroth order coefficient. A  $\pi$ -phase grating is usually used to fulfill this criterion.

The field amplitude at the observation plane obtained for the two-grating case now represents the field at the third grating. Following the derivation in ref. [24], we will consider only the phase difference between the  $A_m B_1$  and  $A_{m+1} B_{-1}$  terms. The full development without excluding the rest of the terms can be found in section C.2 of the appendix. From equation 4.8, the field amplitude at the third grating can be written as

$$V(y) \propto e^{ikL/\cos\theta} \sum_m e^{i\phi_0(m,1)+i\phi_1(m,1)} [A_m B_1 + A_{m+1} B_{-1} e^{i\Delta\phi}] \quad (4.20)$$

with

$$\Delta\phi = \phi_0(m+1, -1) - \phi_0(m, 1) + \phi_1(m+1, -1) - \phi_1(m, 1) \quad (4.21)$$

The expressions for  $\phi_0$  and  $\phi_1$  can be found in equation 4.9. In particular, consider the plane after the second grating given by

$$L_2 = D_1 \frac{f_1}{2f_2 - f_1}$$

One can show that at this “echo” plane the relative phase  $\Delta\phi$  is independent of wavelength and the diffraction order  $m$ . The complex amplitude of the field then becomes

$$V(y) \propto e^{ikL/\cos\theta} \sum_m e^{i[\phi_0(m,1)+\phi_1(m,1)]} [A_m B_1 + A_{m+1} B_{-1} e^{i2\pi(f_1-2f_2)y}] \quad (4.22)$$

Each pair in brackets, together with the global phase, represents an achromatic interference pattern superimposed onto a spherical wave. These are sometimes referred to in the literature as Fourier images from  $G_1$ . It is also common in literature to refer to the pattern at the “echo” plane as a virtual image from the first grating. However, this term can be misleading. If it were a virtual grating, the field after this plane should generate a pattern resembling a Talbot carpet, which is not the case. Furthermore, the individual pairs are affected by a certain phase. On the one hand, the frequency of each term in the summation is not actually  $2f_2 - f_1$  due to the phase term  $\phi_0$ . On the other hand, for a polychromatic source the pairs are mutually incoherent because of the dependence of the phase term  $\phi_1$  on the wavelength.

In any case, if a third grating  $G_3$  is placed in the “echo” plane or near from it, and its frequency is near  $2f_2 - f_1$ , each of the “Fourier images” will form a moiré pattern together with the grating at the image plane. The overall moiré pattern is the incoherent sum of these individual patterns.

The contrast of the fringes at the observation plane is calculated similarly to the two grating interferometer, that is, it is given by the normalized amplitude of the fringes:

$$C = 2 \frac{|\chi_1(\delta_1 P_1, f_1)|}{\langle T_1 T_1^* \rangle} \cdot |B_1 B_{-1}^*| \cdot \frac{|\chi_3(\delta_3 P_3, f_3)|}{\langle T_3 T_3^* \rangle} \quad (4.23)$$

where the autocorrelation distances  $\delta_j$  are

$$\delta_1(\lambda) = \lambda \frac{f_1 L_1}{L} [(f_1 - f_2)(L - L_1) + (f_3 - f_2)L_3 - f_2(D_3 - D_1)] \quad (4.24)$$

$$\delta_3(\lambda) = \lambda \frac{f_3 L_3}{L} [(f_3 - f_2)(L - L_3) + (f_1 - f_2)L_1 - f_2(D_1 - D_3)] \quad (4.25)$$

Also similarly to the two-grating case, the period of the moiré fringes and the source period are independent of the wavelength:

$$P_d = L / [(f_3 - f_2)(L - L_3) + (f_1 - f_2)L_1 - f_2(D_1 - D_3)] \quad (4.26)$$

$$P_s = L / [(f_1 - f_2)(L - L_1) + (f_3 - f_2)L_3 - f_2(D_3 - D_1)] \quad (4.27)$$

In practice, the  $n = \pm 1$  approximation used to derive the contrast formula is generally assumed to be true. However, we have found that it greatly depends on the conditions of the experiment. Despite its validity not being formally studied in this thesis, we will discuss it briefly in section 5.4.2, together with the simulation results for the 3PGMI with neutron matter waves.

The available results we found in the literature mostly make use of X-rays or matter waves. Such waves would cause sampling issues due to their small wavelengths if the simulation is not adapted properly, similarly to what happens for neutrons (see section 5.3). Moreover, the grating misalignment issues in the NIR setup we build in the lab were accentuated, and the resources needed to fix them were not available. For these reasons, the simulations of the 3PGMI will be presented in the next chapter using neutrons.

# Chapter 5

## Neutron matter waves

Throughout this thesis we have focused on the simulation of optical waves and its application to demonstrate the phase-grating moiré interferometer. Larger particles are governed by Schrödinger's equation, whose solution in free-space (when no potential is applied) is similar to the solution of the optical wave equation. Therefore, matter waves suffer from similar effects as their optical counterpart, and the methods we described can be extended to simulate them.

Interferometer designs have been demonstrated for neutrons [1, 57, 58], atoms [2, 59] and even larger molecules [60, 61]. In the two latter cases, however, diffraction effects are affected by short-range interactions related to the electronic structure of the elements, in the same way that charged particles interact with the electron cloud of nuclei. This does not happen with neutrons, since they are electrically neutral particles and therefore they essentially interact with nuclei themselves. This interaction can then be explained as a delta-type effective potential called the Fermi pseudopotential. What is more, at low energies neutrons have relatively large wavelengths (tenths of Bohr radii), or large coherent lengths, which allows to substitute the effect of single collisions by effective potential functions, thus simplifying their study.

In this chapter we present the equations that determine propagation of neutrons in free-space, the effect of phase objects on these matter waves and the sampling conditions required for their simulation. We then apply the conventional scalar diffraction methods to simulate a moiré grating interferometer for neutrons that used the same design as one we presented in the previous section. Finally, the application of this interferometer for precision measurement of phase gradients is discussed, in the particular case of a gravitational potential.

### 5.1 Free-space propagation

According to the theory of quantum mechanics, the behaviour of any particle (in our case, a neutron) is given by the well-known time-dependent Schrödinger Equation:

$$i\hbar \frac{\partial \Psi(\mathbf{r}, t)}{\partial t} = -\frac{\hbar^2}{2m} \nabla^2 \Psi(\mathbf{r}, t) + V(\mathbf{r}) \Psi(\mathbf{r}, t) \quad (5.1)$$

where  $V(\mathbf{r})$  is the potential that describes the action of the elements (slits, gratings, prisms, etc.) that the neutron goes through. The wavefunction  $\Psi(\mathbf{r}, t)$  is related to

the probability of finding a particle at the location  $\mathbf{r}_0$  at time  $t_0$ , as determined by Born's rule [58]:

$$I(\mathbf{r}_0, t_0) = |\Psi(\mathbf{r}_0, t_0)|^2 \quad (5.2)$$

Based on ref. [62], one can proceed to solve the equation above by making the consideration that neutrons propagate much faster longitudinally than in the transverse direction. This means that the distance they will have travelled in a given amount of time will be much larger than the increase in the span of their central diffraction peak. As a result, the time that a neutron spends inside a slit or grating can be neglected, and so the action of such elements on the wave is assumed to be instantaneous. This implies that one can substitute the potential of the element by a suitable initial condition.

Furthermore, the setup of the experiments we will be trying to reproduce consists (in a simplified manner) of a waveguide that carries the neutrons from the source, at the end of which is a slit. This slit's aperture is much wider in the vertical direction than in the horizontal one. Also, the optical elements (e.g. gratings) under consideration are vertically uniform. For these reasons we can ignore diffraction in the  $y$  coordinate. Then, Schrödinger's equation is reduced to:

$$i\hbar \frac{\partial \Psi(x, z, t)}{\partial t} = -\frac{\hbar^2}{2m} \left( \frac{\partial^2}{\partial x^2} + \frac{\partial^2}{\partial z^2} \right) \Psi(x, z, t) \quad (5.3)$$

Another consequence of the aforementioned phenomena is that one can apply the paraxial approximation. If the wave vector fulfills the relation  $k^2 = k_x^2 + k_z^2$ , with  $k = 2\pi/\lambda$ , then it can be assumed that  $k_z \gg k_x$  and  $k \approx k_z$ . As a result, the wavefunction can be written as a product state:

$$\Psi(x, z, t) \approx \Psi(x, t) e^{ik_z z - iE_z t/\hbar} \quad (5.4)$$

The longitudinal component is found to be a plane wave with momentum  $p_z = \hbar k_z$  and energy  $E_z = p_z^2/2m = \hbar^2 k_z^2 / 2m$ . Plugging this expression into equation 5.3, one reaches the equation that must fulfilled by the transverse component:

$$i\hbar \frac{\partial \Psi(x, t)}{\partial t} = -\frac{\hbar^2}{2m} \cdot \frac{\partial^2 \Psi(x, t)}{\partial x^2} \quad (5.5)$$

with initial condition  $\Psi(x, 0)$ . In order to find the solution to this equation one can make use of the (inverse) Fourier transform of  $\Psi(x, t)$ :

$$\Psi(x, t) = \frac{1}{\sqrt{2\pi}} \int \tilde{\Psi}(k_x, t) e^{ik_x x} dk_x \quad (5.6)$$

The purpose of this transformation is to write the wavefunction as a superposition of plane wave with different weights. The equation satisfied by the weight function in momentum space is given by:

$$i\hbar \frac{\partial \tilde{\Psi}(k_x, t)}{\partial t} = \frac{\hbar^2 k_x^2}{2m} \tilde{\Psi}(k_x, t) \quad (5.7)$$

which can be solved with a simple integration:

$$\tilde{\Psi}(k_x, t) = \tilde{\Psi}(k_x, 0)e^{-i\frac{\hbar k_x^2}{2m}t} \quad (5.8)$$

This solution is analogous to the Angular Spectrum formula (or Fresnel in frequency space) for optical waves. The initial condition  $\tilde{\Psi}(k_x, 0)$  corresponds to the Fourier transform of the initial wavefunction  $\Psi(x, 0)$ :

$$\tilde{\Psi}(k_x, 0) = \frac{1}{\sqrt{2\pi}} \int \Psi(x, 0) e^{-ik_x x} dx \quad (5.9)$$

With this we can readily find the solution for the transverse wavefunction in regular space:

$$\Psi(x, t) = \frac{1}{\sqrt{2\pi}} \int \tilde{\Psi}(k_x, 0) e^{ik_x x - i\frac{\hbar k_x^2}{2m}t} dk_x = \frac{1}{2\pi} \iint \Psi(x', 0) e^{ik_x(x-x') - i\frac{\hbar k_x^2}{2m}t} dk_x dx' \quad (5.10)$$

which, after performing the integral on  $k_x$ , results in:

$$\Psi(x, t) = \sqrt{\frac{m}{2\pi i \hbar t}} \int \Psi(x', 0) e^{i\frac{m(x-x')^2}{2\hbar t}} dx' \quad (5.11)$$

Notice that, as in the optical wave case, the solution in regular space is actually the convolution of the initial wavefunction with a certain kernel, which in this case is given by:

$$\mathcal{K}(x) \equiv \sqrt{\frac{m}{2\pi i \hbar t}} e^{i\frac{mx^2}{2\hbar t}} \quad (5.12)$$

According to these results, the simulation methods used for optical waves could also be applied to neutron waves, both in regular and momentum space, just by changing the kernel function. Furthermore, the dependence on time can be converted to a dependence on the propagation distance  $z$ . This is done by considering that the longitudinal component is a plane wave that propagates with velocity  $v = \hbar k_z / m \approx \hbar k / m$ , and therefore  $z = vt \approx (\hbar k / m)t$ . The wavefunction then reads as:

$$\Psi(x, z) \approx \sqrt{\frac{k}{2\pi iz}} \int \Psi(x', 0) e^{i\frac{k}{2z}(x-x')^2} dx' \quad (5.13)$$

This formula is convenient because it is mass independent, and so it can be used both for massive particles and by light. In particular, notice that we have recovered the Fresnel equation for optical waves (see equation 2.22).

Regarding the initial condition, it is common to assume a solution to the wave equation in the form of a Gaussian wave packet:

$$\Psi(x, 0) = \left( \frac{1}{2\pi\sigma_x^2} \right)^{1/4} e^{-\frac{x^2}{4\sigma_x^2}} \quad (5.14)$$

where  $\sigma_x$  is the transverse coherence length. The coherence length acquired by the neutron after exiting the source slit and propagating in free space is given by [58]

$$\sigma_x(L) \sim \frac{\lambda L}{s_w} \quad (5.15)$$

where  $\lambda$  is the de Broglie wavelength of the neutrons,  $s_w$  the width of the slit and  $L$  the distance between the slit and the point of interest. This relation holds when the source of the neutrons (i.e. the reactor core) is far from the slit.

## 5.2 Quantum phase

When neutrons propagate inside a material they suffer the action of nuclear interaction in the form of a Fermi pseudopotential with the nuclei at positions  $\mathbf{R}_j$ . The mean interaction potential, or optical potential, is given by [58]:

$$V = \langle V(\mathbf{r}) \rangle = \left\langle \frac{2\pi\hbar^2}{m} \sum_j b_j \delta(\mathbf{r} - \mathbf{R}_j) \right\rangle = \frac{2\pi\hbar^2}{m} N b_c \quad (5.16)$$

where  $b_c$  is the coherent scattering length of the material. The number density  $N$  is defined as  $N = \rho A_v / M$ , with  $\rho$  the density of the material,  $M$  its molar mass, and  $A_v = 6.02214 \times 10^{23}$  Avogadro's number.

After passing through the material, the neutron accumulates a phase given by the integral over the Lagrangian:

$$\phi = \frac{1}{\hbar} \int_{t_0}^t \mathcal{L} dt' = \frac{1}{\hbar} \int_{t_0}^t (p \cdot v - H) dt' = \int_{x_0}^x k \cdot ds - \int_{t_0}^t \omega dt' \quad (5.17)$$

where  $p$  is the momentum of the neutron,  $v$  its group velocity,  $H = p^2/2m + V(\mathbf{r}, t)$  is its Hamiltonian, and  $\omega = E/\hbar$  is the frequency related to the total energy of the wave at any point along the trajectories [1].

Since the potential under consideration is time-independent, the energy is preserved. For this reason the second term will result in a global phase, and thus it can be ignored. On the other hand, for small perturbations:

$$\frac{(p + \delta p)^2}{2m} + V = E \rightarrow v \cdot \delta p \approx -V \quad (5.18)$$

We are interested in the relative phase  $\Delta\phi$  that neutron gains from the potential action as compared to the phase shift in free space. Using the previous approximation:

$$\Delta\phi = \frac{1}{\hbar} \int_{t_0}^t \delta p \cdot v dt' \approx -\frac{1}{\hbar} \int_{t_0}^t V dt' = -\frac{1}{\hbar v} \int_{z_0}^z V dz \quad (5.19)$$

In conclusion, if a neutron with wavefunction  $\Psi_{in}$  is normally incident on a uniform slab of material whose width is  $D$ , the wavefunction at the end of the slab is given by  $\Psi_{out} = \Psi_{in} \exp(i\Delta\phi)$ , where the relative phase is:

$$\Delta\phi = -Nb_c\lambda D \quad (5.20)$$

Based on this formula, a transparent material can be used to create phase-gratings, in which the height difference between the high and low half-periods determines the relative phase acquired by the neutrons. Moreover, this effect is not exclusive to the optical potential. The phase shift caused by other potentials, including magnetic and gravitational, can be found in ref. [1].

### 5.3 Sampling conditions

For the simulation of neutron propagation, it is convenient to use the diffraction formula in momentum space. One reason for this is that it provides a faster calculation than the diffraction formula in regular space, needing only two Fourier Transforms (implemented with the FFT algorithm) instead of three. To make this argument we are not considering direct integration methods, which can be implemented with only one FFT but at the undesired expense of having to change the sampling space.

A second, more important reason has to do with the sampling conditions required for the implementation of the diffraction formulas. Using the relation  $z = vt$ , the transfer function in momentum space for free-space propagation of neutrons is:

$$H(k_x) = e^{-i\frac{\hbar}{2m}t} \approx e^{-i\frac{z}{2m}k_x^2} \quad (5.21)$$

Since this is exactly the Fresnel formula, with only the minor change that we are now using  $k_x = 2\pi u$ , the sampling condition will be the same that we found for optical waves (see section 2.2.2):

$$N \leq \frac{L^2}{\lambda z} \quad (5.22)$$

In this thesis we have dealt mainly with optical waves in the near-infrared (NIR) region, which correspond to wavelengths of the order of 1  $\mu\text{m}$ . Neutron waves, and in particular the thermal neutrons that we will consider in the simulations, have wavelengths of the order of a few Angstroms ( $1 \text{\AA} = 10^{-10} \text{ m}$ ).

A rough estimation of the maximum propagation distance that allows proper sampling of the transfer function can be done taking into account the period of the optical elements and the width of the sampling space. As we will see later, the period of the phase gratings is of the order of 1  $\mu\text{m}$ , so we can assume that a good sampling of the gratings would be obtained with a sampling period at least an order of magnitude lower ( $\delta_x = 10^{-7} \text{ m}$ ). As for the sampling width, let us assume  $L = 1 \text{ cm}$ , which would correspond to  $N = 10^5$  sampling points. This number is chosen arbitrarily considering time and memory cost of the simulation. With these values the maximum distance is of the order of:

$$z \leq \frac{L\delta_x}{\lambda} \sim 10 \text{ m} \quad (5.23)$$

As a result, even though the gratings have a smaller period than the ones used in the NIR optical wave simulations, the much smaller wavelength allows to simulate larger distances. Furthermore, the total distances of the interferometers that we will consider are of the order of a few meters, hence falling into the range for proper sampling.

Even if the case occurred that a distance were to be larger, or different parameters were used where this condition might not hold, one could apply the same argument as in optical waves to limit the frequency (or momentum) used in the calculation of the transfer function. Following the procedure described in section 2.3.3, the local frequency of the neutron propagator in the paraxial region is given by:

$$f_k = \frac{1}{2\pi} \cdot \frac{\partial \phi}{\partial k_x} = \frac{-zk_x}{2\pi k} \quad (5.24)$$

where  $\phi$  is the phase of the transfer function. From the Nyquist theorem, the sampling period of the momentum space has to satisfy the relation  $\delta_k^{-1} \geq 2|f_k|$ . From this we can extract the maximum momentum to be used:

$$|k_x| \leq \frac{\pi k}{z\delta_k} \equiv k_{x,lim} \quad (5.25)$$

The resulting transfer function is then:

$$H'(k_x) = H(k_x) \cdot \text{rect}\left(\frac{k_x}{2k_{x,lim}}\right) \quad (5.26)$$

The above formula can be applied for any distance regardless of the parameters of the simulation. On the contrary, the diffraction formula in the regular space cannot be forced to meet the sampling conditions in the near field, which is often times the region we are interested in when dealing with neutrons, and therefore is generally not suitable.

On a side note, here we are only considering diffraction in the paraxial approximation. Due to the small wavelengths of neutrons, this approximation is even more reasonable than in the NIR optical case, and so in most cases we do not need to consider a more general approach.

The transfer function is not the only element that has to be properly sampled. One must also take into account the sampling of the field, which is usually given in the regular space and has to be Fourier-transformed before applying the transfer function to it. A potential issue might arise when a neutron propagated at an angle with respect to the  $z$  axis:

$$\Psi = A e^{ikx \sin(\theta)} \quad (5.27)$$

A plane wave, with constant amplitude  $A$ , is considered for simplicity, but the argument also applies for other possible wavefunctions. The phase term accounts for the direction of propagation. To find the sampling requirements, we can proceed in the same way as we did for the optical impulse responses, that is, we can make

the argument that the Nyquist theorem is met if there are at least two sampling points in every  $2\pi$  phase change of the wavefunction:

$$\left| \frac{\partial}{\partial x} \left( \frac{2\pi}{\lambda} x \sin(\theta) \right) \right| \times \delta_x \leq \pi \quad (5.28)$$

In this case the phase is linear so the requirement is the same no matter which values  $x$  can take. The minimum sampling period required is:

$$\delta_x \leq \frac{\lambda}{2 \sin(\theta)} \quad (5.29)$$

The maximum angle of a beam in the kind of systems that we are considering in this project is small. In spite of this, the condition above is easily satisfied when working at NIR wavelengths, but with wavelengths in the range of cold neutrons it becomes an important limitation. For example, if we consider a beam with a maximum divergence angle  $\theta_{max} = 0.5^\circ$  and a sampling space width of  $L = 1\text{ cm}$ , then a NIR wave with  $\lambda = 1\text{ }\mu\text{m}$  would require  $N \approx 200$  sampling points, but an X-ray or neutron wave with  $\lambda = 1\text{ \AA}$  would need  $N \approx 2 \times 10^6$  sampling points. We must take into account that this applies to a single beam or wavefunction. In an actual simulation the calculation has to be repeated for a large number of neutrons, and possibly in a higher sampling space, so it quickly becomes unfeasible.

In order to find a solution to this issue consider a neutron with an initial wavefunction of the form:

$$\Psi(x, 0) = f(x) e^{ik_{0x}x} \quad (5.30)$$

with  $k_{0x} = k \sin(\theta)$ . The subscript is used to differentiate this value from the  $k_x$  coordinate in momentum space. Recall also the propagation kernel in momentum space, without approximating  $k_z$ :

$$U_t = e^{-i \frac{\hbar k_x^2}{2m} t} = e^{-i \frac{z}{2k_z} k_x^2} \quad (5.31)$$

where we have made use of the relations  $z = vt$  and  $v = \hbar k_z / m$ , with  $k_z = k \cos(\theta)$ . Then, the wavefunction after a propagation in free-space of a distance  $d$  is given by

$$\Psi(x, d) = P[\Psi(x, 0)](x) = \mathcal{F}^{-1} [\mathcal{F}[\Psi(x, 0)](k_x) \cdot U_t](x) \quad (5.32)$$

where  $\mathcal{F}[\dots]$  denotes the Fourier Transform and  $P[\dots]$  the propagation operator. Here, it is convenient that the output coordinates of each operator are explicitly stated. Substituting the expression of the initial wavefunction and the propagator:

$$\Psi(x, d) = P[f(x) e^{ik_{0x}x}](x) = \mathcal{F}^{-1} \left[ \mathcal{F} [f(x) e^{ik_{0x}x}] (k_x) \cdot e^{-i \frac{d}{2k_z} k_x^2} \right] (x) \quad (5.33)$$

We can apply the frequency shifting property to take the phase term out of the inner Fourier Transform:

$$\Psi(x, d) = \mathcal{F}^{-1} \left[ \mathcal{F}[f(x)](k_x - k_{0x}) \cdot e^{-i \frac{d}{2k_z} k_x^2} \right] (x) \quad (5.34)$$

The exponential term can be expanded using that

$$k_x^2 = (k_x - k_{0x})^2 + 2k_x k_{0x} - k_{0x}^2 \quad (5.35)$$

and the expression above then becomes:

$$\Psi(x, d) = \mathcal{F}^{-1} \left[ \mathcal{F}[f(x)](k_x - k_{0x}) \cdot e^{-i \frac{d}{2k_z} (k_x - k_{0x})^2} \cdot e^{-i \frac{d}{2k_z} 2k_x k_{0x}} \cdot e^{i \frac{d}{2k_z} k_{0x}^2} \right] (x) \quad (5.36)$$

The last term just adds a constant phase, so it can be ignored. As for the second-to-last term, we can apply the time-shifting property and take it out of the inverse Fourier Transform:

$$\Psi(x, d) = \mathcal{F}^{-1} \left[ \mathcal{F}[f(x)](k_x - k_{0x}) \cdot e^{-i \frac{d}{2k_z} (k_x - k_{0x})^2} \right] \left( x - k_{0x} \frac{d}{k_z} \right) \quad (5.37)$$

Now we can use the frequency-shifting property again, which results in a global phase term:

$$\Psi(x, d) = \mathcal{F}^{-1} \left[ \mathcal{F}[f(x)](k_x) \cdot e^{-i \frac{d}{2k_z} k_x^2} \right] \left( x - k_{0x} \frac{d}{k_z} \right) \cdot e^{ik_{0x}x} \quad (5.38)$$

Again, an additional constant phase term been ignored. Finally, using  $k_{0x} = k \sin(\theta)$  and  $k_z = k \cos(\theta)$ , we reach

$$\Psi(x, d) = \mathcal{F}^{-1} \left[ \mathcal{F}[f(x)](k_x) \cdot e^{-i \frac{d}{2k_z} k_x^2} \right] (x - d \tan(\theta)) \cdot e^{ik_{0x}x} \quad (5.39)$$

Notice that this expression matches with the definition of the propagation operator  $P$ , thus achieving the following relation:

$$\Psi(x, d) = P[\Psi(x, 0)](x) = P[f(x)](x - d \tan(\theta)) e^{ik_{0x}x} \quad (5.40)$$

According to this result, we can propagate the initial wavefunction without the phase term that causes the sampling issues, and perform a simple change of coordinates to the result. Notice that this coordinate change is just a shift, so it does not actually modify the sampling of the field. Furthermore, even if we perform multiple propagations, the phase term will be carried to the final result only to vanish when the intensity is calculated, so it can be ignored altogether. This method also provides the additional advantage that, since each neutron needs its own output space, the required sampling width only depends on the width of its individual wavefunction and not on the total extension of the field comprised of all the possible neutrons' wavefunctions. As a result the sampling space is smaller and propagation is faster.

## 5.4 Phase-grating moiré interferometer

We have seen that neutrons suffer from diffraction effect just like photons, and that phase gratings can be fabricated. Therefore, it is possible to build interferometers such as the ones we presented previously employing neutron matter waves, in particular the moiré interferometer. In this section we present the simulations for both the two-grating and three-grating designs and compare them to recently published experimental results.

The simulations are build in the following way. For a single neutron, the wavefunction is initialized at the plane of the first object, assuming that it is given by a Gaussian wavepacket with the proper coherence length. Each object acts on it as a mask, and the neutron is propagated between objects with the Fresnel method, sampling the transfer function directly in momentum space. At the detector plane, the wavefunction is squared to obtain the corresponding probability density function. To simulate the entire neutron beam, the calculation is run for a number of neutrons, each with a random initial position inside the slit source (following a uniform distribution) and a random initial propagation angle. Their squared wavefunctions are summed up in the end, thus obtaining a pattern that resembles the one that a large number of neutrons would end up forming. Due to the randomized behaviour of the initial conditions, the more neutrons are simulated the more reliable the final results ought to be.

### 5.4.1 Two phase-grating interferometer

A neutron 2PGMI was demonstrated by Pushin *et al.* in 2017 [25]. They provide contrast results for the fringes observed with monochromatic and bichromatic beams, as well as a polychromatic source following approximately a Maxwell distribution. We focus on the monochromatic case because we believe that the results are the most reliable, mainly regarding the exact experimental conditions. The system consists of a slit source, with a width of  $s_w = 200 \mu\text{m}$  that emits neutrons at  $\lambda = 0.44 \text{ nm}$  (we can ignore the fact that the source had another important component at  $0.22 \text{ nm}$  since it was filtered out with almost perfect efficiency). A first grating is placed at a distance of  $L_1 = 1.2 \text{ m}$  from the slit, while a movable second grating is set at a distance  $D$  from it. Both gratings have a period of  $P = 2.4 \mu\text{m}$  and provide a phase change of  $0.27\pi \text{ rad}$ . We will use this gratings to match the experiment conditions, although ideally  $\pi/2$ -gratings would offer the maximum contrast. The total distance from the slit to the camera is  $L = 2.99 \text{ m}$ .

Since the beam is (partially) incoherent, the patterns at the camera should resemble almost perfect sinusoidals, as we found in the optical 2PGMI. Due to the randomized nature of the simulation, this is the case if the number of neutrons is large enough. The contrast and frequency results for different intergrating distances, obtained by fitting a sine to the data, are shown in figure 5.1. The results match with the ones provided in the reference. It should be mentioned, in order to match the units of frequency, that the values given in figure 4 of the reference were divided by a factor of  $\pi$ .

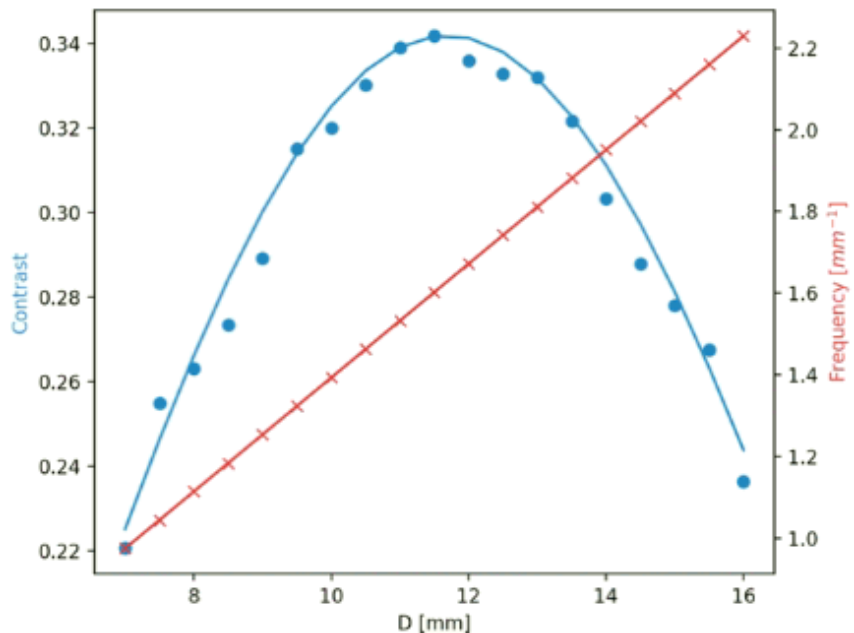


**Figure 5.1:** Contrast and frequency results for the neutron 2PGMI with a monochromatic beam. The dots/crosses show the simulation results, as compared to the analytical expected values (solid lines). The neutron wavelength is  $\lambda = 0.44 \text{ nm}$ , and the slit source has a width of  $s_w = 200 \mu\text{m}$ . The gratings have a period of  $P = 2.4 \mu\text{m}$  and a  $0.27\pi$  phase shift at that wavelength. The first grating is placed at a distance of  $L_1 = 1.2 \text{ m}$  from the slit source, while the total distance from source to camera is  $L = 2.99 \text{ m}$ . The second grating is movable, being  $D$  its separation from the first one. The simulation at each distance step has been performed with  $N_n = 25\,000$  neutrons.

### 5.4.2 Three phase-grating interferometer

The previous experiment was extended to the three-grating design by Sarenac *et al.* in 2018 [26]. In the new setup, the slit width is  $s_w = 500 \mu\text{m}$ . Three gratings are placed in front of it, all with a period of  $P = 2.4 \mu\text{m}$ . At the mean wavelength of  $\lambda_c = 0.5 \text{ nm}$ , the gratings correspond approximately to  $\pi/2$ ,  $\pi$  and  $\pi/2$  phase changes, respectively. The second grating is fixed at  $L_{s2} = 4.75 \text{ m}$  from the source, while the total distance from source to camera is  $L = 8.8 \text{ m}$ . The first grating is set at a distance of  $D_1 = 4.6 \text{ cm}$  before the second, and the third one will be translated along the longitudinal axis. To follow the notation introduced in section 4.3, we will denote by  $D_3$  the separation between the second and third gratings.

Before considering the polychromatic source used in the experiment, let us discuss first the monochromatic case. Consider a neutron source emitting only at a wavelength of  $0.5 \text{ nm}$ . As the reference mentions, from the autocorrelation distances of the first and third gratings one reaches the conclusion that a maximum in the contrast should be found when the third grating is placed at around  $D_3 - D_1 = 1.2 \text{ cm}$  from the “echo” plane. The simulations, however, show the exact opposite: an almost null contrast at that distance. In fact, with the given parameters the analytical expression of the contrast that one obtains by using the  $n = \pm 1$  approximation (see section 4.3) differs greatly from the result considering the whole summation over  $n$  (provided in section C.2 of the appendix). This is clearly seen in figure 5.2. Furthermore, the simulations agree with the non-approximate expression.

The issue exposed above does not seem to have been discussed in literature, nor do the conditions that are assumed to make the approximation. In any case, the source used for the experiment presented in the reference was not actually monochromatic, but rather its spectrum was approximately given, in terms of the velocity distribution of the output neutrons, by a Maxwell-Boltzmann distribution:

$$f(v) = \left( \frac{m}{2\pi k_B T} \right)^{3/2} 4\pi v^2 e^{-\frac{mv^2}{2k_B T}} \quad (5.41)$$

Here,  $k_B$  is the Boltzmann constant and  $T$  is the thermodynamic temperature, which in the reference is said to be  $T = 40 \text{ K}$ . This distribution can also be written in terms of the wavelength, using that  $v = 2\pi\hbar/m\lambda$  and  $f(v)dv = f(\lambda)d\lambda$ . Ignoring a negative sign coming from the differential (which would otherwise disappear when reversing the integration limits):

$$f(\lambda) = \left( \frac{m}{2\pi k_B T} \right)^{3/2} \left( \frac{2\pi\hbar}{m} \right)^2 \frac{4\pi}{\lambda^4} e^{-\frac{m}{2k_B T} \left( \frac{2\pi\hbar}{m\lambda} \right)^2} \quad (5.42)$$

The simulation results obtained with this spectrum are shown in figure 5.3. Opposite to the monochromatic case, the approximation in the contrast calculation now seems to give accurate results, as compared to both the simulations and the full analytical expression. The magnitude of the contrast is around 7 times larger than the actual contrast measured in the reference, although the shape of both plots is practically the same. This disagreement is most certainly due to experimental reasons, including the alignment of the gratings and their imperfect profile.

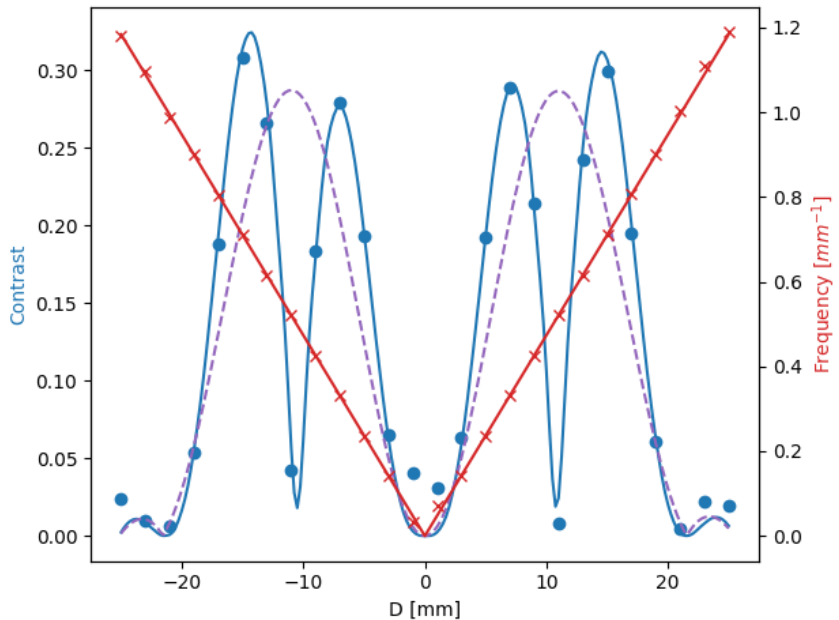


**Figure 5.2:** Contrast and frequency results for the simulation of the neutron 3PGMI with a monochromatic source. Solid lines show the analytical results. The purple dashed line corresponds to the contrast calculated using the  $n = \pm 1$  approximation, in comparison to the contrast calculated using the full expression (blue solid line). The system consists of two  $\pi/2$ -phase gratings with a period of  $P = 2.4 \mu\text{m}$  and an additional  $\pi$ -phase grating, of the same period, placed in between them. The distance from the slit source to this middle grating is  $L_{s2} = 4.75 \text{ m}$ , while the total distance from the source to the observation plane is  $L = 8.8 \text{ m}$ . The first grating is fixed at a separation  $D_1 = 4.6 \text{ cm}$  from the middle grating, while the third one is translated along the longitudinal axis. The horizontal axis shows  $D = D_3 - D_1$ . The simulation at each distance step has been performed with  $N_n = 10\,000$  neutrons.

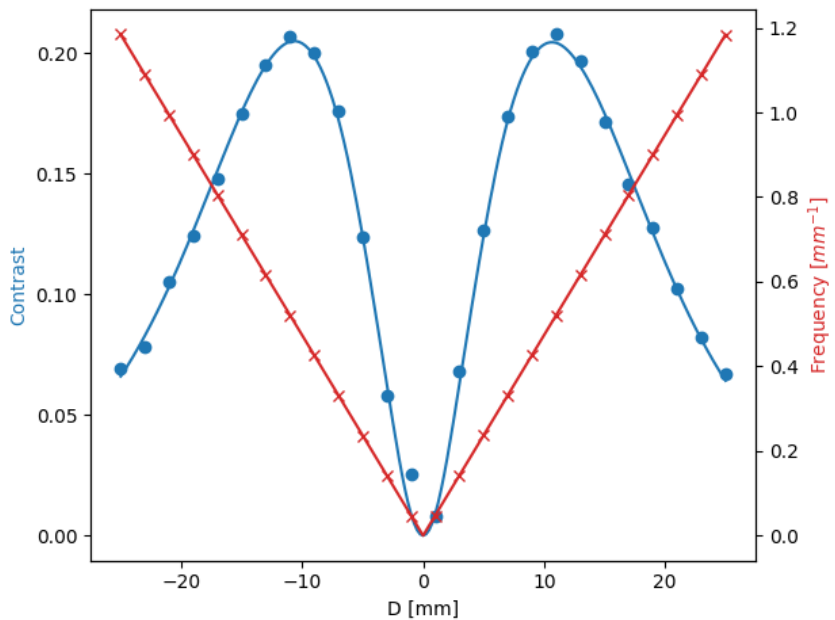


**Figure 5.3:** Contrast and frequency results for the simulation of the neutron 3PGMI with a polychromatic source. Solid lines show the analytical results, while dots/crosses correspond to the simulations. The source's spectrum is given by a Maxwell-Boltzmann distribution with  $T = 40\text{ K}$ . The system configuration is the following. A  $\pi$ -phase grating is fixed at a distance of  $L_{s2} = 4.75\text{ m}$  from the slit source. At each side of it, a  $\pi/2$ -phase grating is placed. The one on the source side is placed at  $D_1 = 4.6\text{ cm}$  from the  $\pi$  grating, while the other one is movable. All three gratings have the same period  $P = 2.4\text{ }\mu\text{m}$ . The distance  $D$  in the plot corresponds to the displacement of this last grating with respect to the “echo” plane, that is,  $D = D_3 - D_1$ . The observation plane is set at  $L = 8.8\text{ m}$  from the source. The simulation at each distance step has been performed with  $N_n = 25\,000$  neutrons, each of which with a random wavelength according to the spectrum distribution.

## 5.5 Gravitational potential

One of the most promising applications of neutron moiré interferometry is its usage for precision measurements. More specifically, it is believed that the neutron 3PGMI is a good candidate to determine the value of the universal gravitational constant  $G$  with a higher precision than the current standards [58]. With this in mind, in this section we present a method for the simulation of neutron propagation through a linear potential, and afterwards discuss its application for the particular case of gravity.

In general, when an arbitrary potential is acting on the particle, the corresponding Schrödinger Equation must be solved numerically, usually employing costly grid methods [63]. Nonetheless, certain potentials allow to be approached using operator techniques [64]. For the particular case of a linear potential of the form  $V(x) = Fx$ , the solution obtained with such procedure (see appendix D) can be written as:

$$\Psi(x, t) = \exp\left(-i\frac{tF}{\hbar}x\right) \sqrt{\frac{m}{i2\pi\hbar t}} \int_{-\infty}^{\infty} \Psi(x', 0) \exp\left[i\frac{m}{2\hbar t}\left(x - x' + \frac{Ft^2}{2m}\right)^2\right] dx' \quad (5.43)$$

This expression is extremely similar to the solution of the Schrodinger Equation in free space (eq. 5.11), with the exception of a couple of modifications. On the one hand, the propagation kernel is the same but shifted in  $x$  by an amount of  $Ft^2/2m$ . Since it is a convolution, we can still apply the same methods to perform the calculation. That is to say, we can calculate the integral with either two or three FFTs, depending on whether we consider the kernel in position or momentum space. However, as an alternative we can also apply the free-space (Fresnel) kernel directly and simply change the output coordinates according to

$$x \rightarrow x + d^2 \frac{Fm}{2\hbar^2 k_z^2} \quad (5.44)$$

where  $d = vt$  is the propagation distance and  $v = \hbar k_z/m$ , with  $k_z = k \cos(\theta)$ . This has the advantage that the sampling requirements remain the same regardless of the potential coefficient.

On the other hand, according to the results in section 5.3, the linear phase term in front corresponds to an output propagation angle with respect to the  $z$  axis. As a result, we can just update the propagation angle in order to apply the proper coordinate change in subsequent propagations. The new propagation angle is then given by:

$$\theta' = \arctan\left[\tan(\theta) - \frac{dFm}{\hbar^2 k^2 \cos^2(\theta)}\right] \quad (5.45)$$

For the particular case of the gravity, which in the linear approximation corresponds to  $F = mg$ , with  $m$  the neutron's mass and  $g$  the standard gravitational acceleration, the phase acquired by the neutron due to the effect of the potential is:

$$\phi = \frac{mgtx}{\hbar} \approx \frac{m^2 g x z}{k \hbar^2} = \frac{m^2 g \lambda x z}{2\pi \hbar^2} \quad (5.46)$$

Notice that if we are referring to the Earth's gravitational potential,  $x$  denote the vertical coordinate. This expression agrees with the results provided by Colella, Overhauser and Werner [65], who demonstrated gravitational effects on a quantum particle for the first time using a perfect crystal interferometer. The basic idea of their experiment (commonly named COW, in relation to the authors) is that two neutrons that follow different paths inside an interferometer will acquire a certain phase according to the expression above. If the interferometer is rotated around its axis, the relative phase between the neutrons will change progressively, thus revealing the effect of the potential.

The main disadvantages of their design resided in the small area of the interferometer and the very low neutron acceptance. Furthermore, the own weight of the interferometer also added an additional phase to the neutrons that could not be neglected. In contrast, the 3PGMI overcomes this obstacles, allowing large interferometer areas and a broadband neutron acceptance [26]. The gratings have the same function as the perfect crystals, with the paths now being described by their main orders of diffraction, as shown in figure 5.4. The relative phase between paths 1-3 and 2-4 due to the linear potential can be calculated as:

$$\Delta\phi = \frac{k_0 m g \sin(\alpha)}{2E_0} \left( \frac{\sin \theta}{2 \cos^2 \theta} (D_3^2 - D_1^2) - D_1 D_3 \tan \theta \right) \quad (5.47)$$

with  $k_0 = 2\pi/\lambda$  and  $E_0 = (\hbar k_0)^2/2m$ . The angles correspond to the angle of diffraction from the gratings  $\theta = \lambda/P$  and the rotation of the interferometer  $\alpha$ , which is achieved simply by a rotation of its elements (i.e. gratings and source slit) around their longitudinal axis. It is straightforward to check that when  $D_1 = D_3$  the formula from the original COW experiment is recovered. In this case, the phase change in paths 2 and 3 is the same, but the one in paths 1 and 4 is not due to the effect of the potential. Furthermore, if the third grating is displaced, paths 3 and 4 do not reach the grating at the same point (and they become a different length than 2 and 1, respectively), causing an additional relative phase that must be accounted for. The equation above is valid as long as the coherence length of the neutron at the third grating is larger than the path separation at that same plane in order to have interference. Despite this condition imposing a limitation on the length of the interferometer, it is not very restrictive in practice.

In order to test check this effect, we will simulate the experiment for the 3PGMI. More specifically, we will try to recover the value of  $g$  from the relative phase of the pattern after the interferometer. The configuration of the system is the same that was detailed in section 5.4.2, except that the first grating is now placed at a distance  $D_1 = 1\text{ m}$  from the second. For practical reasons, we will consider a monochromatic beam with  $\lambda = 0.5\text{ nm}$ . To maximize contrast, the third grating is placed at  $D_3 = 1.01\text{ m}$ , that is, it is displaced  $D = 1\text{ cm}$  from the "echo" plane.

For simplicity, we consider that the no potential is present between the slit source and the first grating. In the region from the first grating to the camera, a linear potential  $F = mg \sin(\alpha)$  is applied, where the  $\alpha$  accounts for the rotation of the

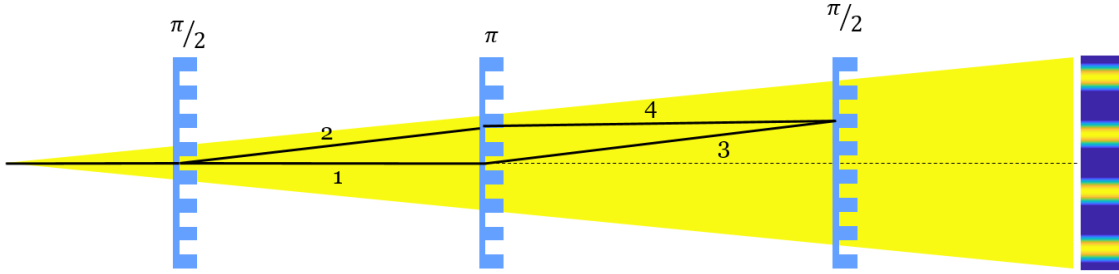


**Figure 5.4:** Schematic of the paths inside the 3PGMI. The first grating separates the beam mainly into its zeroth and first orders of diffraction. Each of these diffracts again in the first order of the second grating, to recombine at the “echo” plane. The third grating is shown at this plane, although in reality it would be displaced in order to produce moiré fringes in the far field.

interferometer around its longitudinal axis. When  $\alpha = 0$ , the gratings are placed such that they have their periodicity in the  $x$  direction. The simulation is performed, using the method described earlier in this section, for a number of different angles of rotation. For each one, the pattern at the observation plane is fitted to a sine function. The period and contrast of the fringes are the same regardless of the rotation, apart from statistical fluctuations ( $P_d = 2.112$  mm and  $C \approx 34\%$ ).

The phase is plotted against the angle of rotation in figure 5.5, and fitted to a function of the form  $f(x) = A + B \sin(\alpha)$ . We then get that  $B = (-41.244 \pm 0.006)$  rad. Relating this term to equation 5.47, we find a gravitational acceleration of  $g = 9.863$  m/s<sup>2</sup>, which corresponds to a discrepancy of 0.567% with respect to the nominal value ( $g_0 = 9.806\,65$  m/s<sup>2</sup>).

There are two possible sources of error. First, the uncertainty in the fit of each pattern, that in turn propagates to an uncertainty in the fit of the phase, which is the one given for  $B$  above. Second, the statistical uncertainty caused by the randomization of the initial position and angle of incidence of the neutrons forming the beam. This has not been quantified.

In any case, a third factor contributes to the error, which is the effect of the potential in the last propagation (after the third grating). Notice that equation 5.47 only accounts for the relative phase of the paths between the first and third grating. However, as we saw earlier in this section, the linear potential causes a shift to the beam, which represents an additional phase on the final pattern. In our simulation, the correction due to this fact is found to be  $\Delta B = 0.5$  rad, and therefore the measured phase coefficient inside the interferometer is  $B' = B - \Delta B = -41.744$  rad. As a comparison, we can repeat the simulation without including a potential in the last propagation, that is, propagating in free space from the third grating to the camera. Then, inside this region the neutrons propagate at an angle given by equation 5.45. In this case, assuming a null average angle of incidence on the first grating, we obtain a relative phase at the camera of  $B_{np} = (-41.462 \pm 0.006)$  rad and a shift of  $\Delta B_{np} = 0.285$  rad, which gives a phase coefficient inside the interferometer of  $B'_{np} = -41.747$  rad. Both corrected terms match given the numerical uncertainty, which proves that the simulation is consistent. However, they do not agree with the expected value given by equation 5.47,  $B_{th} = -41.010$  rad, exposing that this formula might not be correct. Its further study is outside of the scope of this thesis.

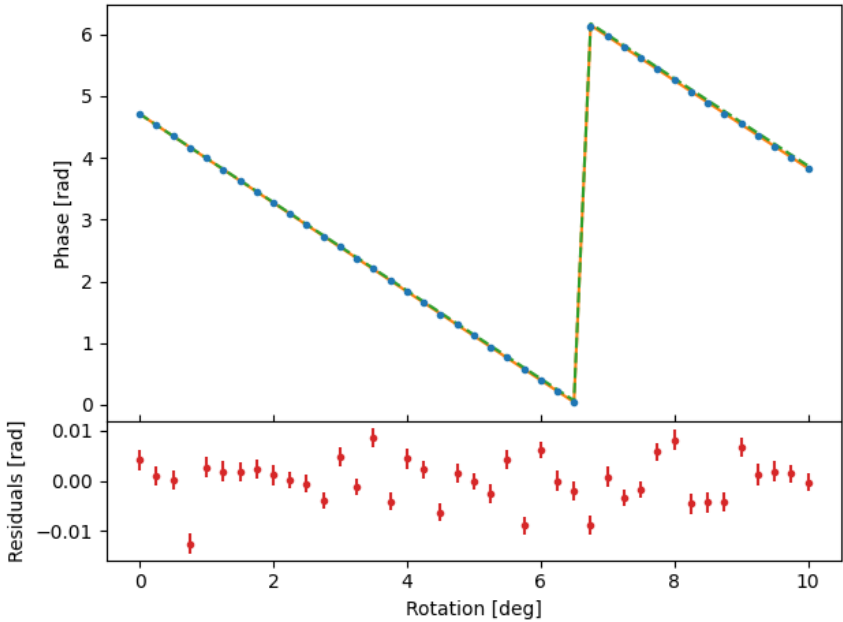


**Figure 5.5:** Phase of the pattern from the neutron 3PGMI when a gravitational potential is applied, as a function of the interferometer rotation. Each point is obtained as follows. The pattern after the three phase-grating interferometer is obtained considering a single neutron wavelength of  $\lambda = 0.5 \text{ nm}$  and a grating period of  $P = 2.4 \mu\text{m}$ . The first and second gratings are separated by a distance of  $D_1 = 1 \text{ m}$ , while the separation between the second and third gratings is  $D_3 = 1.01 \text{ m}$ . The central grating is fixed at  $L_{s2} = 4.75 \text{ m}$  from the source, and the total distance from source to camera is  $L = 8.8 \text{ m}$ . A linear potential  $V = mg \sin(\alpha)$ , is applied to the neutrons in the region from the first grating to the camera (that is, the propagation to the first grating is performed without any potential). The  $\alpha$  factor accounts reproduces the rotation of the interferometer. The intensity at the detector is then fit to a sine, whose phase corresponds to the blue dots. Their numerical uncertainty is smaller than the dot size. This points are, in turn, fitted to a function of the form  $A + B \sin(\alpha)$ , where  $B$  is the phase slope caused by the potential. The result from this fit is the orange line, while the dashed green is obtained using the same value of  $A$  but the theoretical value for  $B$  according to equation 5.47. This line is slightly above than the orange one. The residuals show below correspond to the difference between the points from the simulation and the fit (orange line), and the error bars show the numerical uncertainty in the phase calculation.

# Chapter 6

## Conclusion

During the course of this thesis we have presented a numerical model for the simulation of optical systems that make use optical waves as well as neutron waves. This method has been proven to describe correctly published experimental results, as well as some experiments built purposely for the occasion. The simulation was also extended to include propagation inside a linear potential. The code is available on demand<sup>1</sup>.

First, we have presented the most commonly used formulas from the scalar diffraction theory of optical waves. From these, we have chosen the Angular Spectrum formula for most of the light simulations in this thesis. The reason for that is that it provides a general - not approximated - method to calculate diffraction with only two FFTs while also keeping the original sampling space. This formula relies on a convolution that must be linearized by zero-padding the input field to avoid numerical issues. Its accuracy can be improved by using a higher-order quadrature rule. Furthermore, its sampling requirements limit its usage to only short propagation distances. This condition can be overcome by limiting the transfer function to a maximum bandwidth, thus avoiding aliasing issues without compromising the correctness of the calculation.

Next, we have introduced the Talbot self-imaging effect, according to which an image of a binary amplitude grating is repeated at specific distances when it is illuminated by a monochromatic plane wave. Similar effects have also been presented for phase gratings, which create intensity patterns resembling the grating structure called Lohmann images, and incoherent beams (Lau effect). The intricate, periodic pattern created by the field after the grating has been shown for all three cases. The Talbot effect has also been extended to the case of Gaussian beam illumination, which produces magnified images of the grating. To emphasize this magnification and obtain a cone beam, we have added a lens to the system and, using a NIR laser, we have obtained experimental images matching the simulation.

The previous effects constitute the basis for various interferometer designs. In particular, we have studied two different designs, the first one being the Talbot interferometer. It consists in two amplitude gratings separated by half a Talbot distance, in such a way that the field from the first grating is (almost) completely blocked by the second. When a phase object is placed in between the gratings, it produces a

---

<sup>1</sup>Please contact the author at [rogerserrat11@gmail.com](mailto:rogerserrat11@gmail.com)

displacement in the field and a grating-like pattern is seen at the detector. We have checked this with a linear-phase object, which produces a constant beam displacement. This design is widely used in imaging applications, but its sensitivity is too low for precision measurements.

An alternative design makes use of the universal moiré effect for phase gratings. Two of such gratings are placed close together and illuminated by a cone beam. The magnification of the beam causes the two gratings to have an effectively different period, and thus they act as a beat grating, producing fringes in the far field. We have compared the contrast and frequency of the fringes obtained with the simulations with their analytical expected values, as well as experimental results for a coherent beam. For the case of an incoherent beam, we have reproduced the results in ref. [24]. We have also presented an extension of this design that is built by adding a third grating. The properties of the fringes then depend on the relative position of the third grating with respect to the first, which allows for a much larger interferometer length.

Finally, we have described a modification of the model to simulate neutron matter waves. We have derived the corresponding diffraction formula and discussed its sampling requirements. These conditions become prohibitive when the neutrons are propagated at an angle. For that matter, we have presented a solution that consists in propagating each neutron in its own local space, and updating the space coordinates appropriately. We have then been able to reproduce the results in ref. [25] for the two-grating moiré neutron interferometer with a monochromatic beam, as well as the ones in [26] for the three-grating system with a polychromatic beam. Regarding this last design, we have also discussed the case of the monochromatic beam, and we have found that the approximated expression that is commonly used to determine the contrast of the moiré fringes is not always correct.

In addition, we have shown that the model can also be used to simulate propagation of neutrons inside a linear potential. The properly modified model has been employed to extract a value of  $g$  that differs by 0.5 % from the value used in the simulation itself. Possible sources of error, not quantified, are numerical uncertainties (for example, due to the discrete sampling), statistical uncertainties caused by the randomized neutron initialization and the non-negligible effect that the potential has on the last propagation after the interferometer. Moreover, if a real experiment were to be simulated other effects might have to be taken into account, such as the bending of the interferometer, the Sagnac effect, etc.

The model used throughout this thesis treats independently the initial fields, propagation methods and the optical elements. As a result, it can be easily adapted for further investigations and studies of new materials. For example, it could be extended to non-ideal gratings with custom profiles. Furthermore, its capability of simulating propagation under a linear potential allows for more complex potentials to be simulated. This can be done by approximating the potential as a sequence of linear potentials, and then propagating in discrete steps.

# APPENDICES

# Appendix A

## Diffracton of a Gaussian beam from a periodic object

The aim of this section is to provide detail on some calculations that one encounters when studying diffraction of a Gaussian beam. In particular, the diffraction pattern from a periodic object under Gaussian beam illumination is obtained using the Fresnel formula, as well as the self-imaging conditions that appear as a consequence of this result. The analysis presented here is based on ref. [66], although the notation is adapted to the one used in this document. Last, the one-dimensional expression for a Gaussian beam is included.

The following notation will be used throughout this section:

- $(x', y')$ : coordinates in the object plane
- $(x, y)$ : coordinates in the observation plane
- $R$ : wavefront curvature.  $R > 0$  when the beam is divergent.
- $\mathcal{R}$ : distance from point  $(x', y')$  in the object plane to point  $(x, y)$  in the observation plane
- $T(x')$ : distribution of light in the object (i.e. transmission function), assumed to be one-dimensional and periodic
- $P$ : spatial period of the object
- $a_n$ : amplitude of the  $n$ th harmonic when  $T(x)$  is expressed as a Fourier series
- $\omega$ : Gaussian beam radius at an arbitrary plane, taken to be the object plane, at a distance  $\gamma$  from the beam waist
- $\omega_z$ : Gaussian beam radius at a distance  $z$  from the object plane
- $\omega_0$ : Gaussian beam radius at beam waist
- $U_G$ : diffraction amplitude on a plane at a distance  $z$  from the object plane

Using this notation, the complex amplitude of a 2-dimensional Gaussian beam at the object plane  $\gamma$  is given by:

$$U_G(x', y', \gamma) = A \frac{\omega_0}{\omega} e^{-\frac{x'^2+y'^2}{\omega^2}} e^{i\left(\frac{k(x'^2+y'^2)}{2R}-\varphi(\gamma)\right)} e^{ik\gamma} \quad (\text{A.1})$$

where  $A$  is a constant that determines the maximum amplitude at the beam waist and  $\varphi$  is the so-called Gouy phase.

## A.1 Fresnel integral

In the following pages the calculation of the Fresnel diffraction integral is presented for the mentioned case, putting the focus on the terms that contribute to the formation of self-images of the object.

### A.1.1 Integral solution

Consider an object with a periodicity in the horizontal coordinate, whose transmission function can be represented with a Fourier series:

$$T(x') = \sum_{n=-\infty}^{\infty} a_n e^{i \frac{2\pi n}{P} x'} \quad (\text{A.2})$$

The diffracted field, under the paraxial approximation, when the object is illuminated with a Gaussian beam is obtained with Fresnel's formula:

$$U_G(x, y, z) \propto \frac{1}{i\lambda z} \iint_{-\infty}^{\infty} e^{-\frac{x'^2+y'^2}{\omega^2}} T(x') e^{\frac{k(x'^2+y'^2)}{2R}} e^{ik\mathcal{R}} dx' dy' \quad (\text{A.3})$$

where

$$e^{ik\mathcal{R}} = e^{ik \left[ z + \frac{x^2+y^2}{2z} - \frac{1}{z}(xx'+yy') + \frac{x'^2+y'^2}{2z} \right]} \quad (\text{A.4})$$

For convenience, this integral can be rewritten as

$$U_G(x, y, z) \propto \frac{1}{i\lambda z} C I_1 I_2 \quad (\text{A.5})$$

with

$$C = e^{ik \left( z + \frac{x^2+y^2}{2z} \right)} \quad (\text{A.6})$$

$$I_1 = \int_{-\infty}^{\infty} e^{-\alpha x'^2 - i\beta_x x'} T(x') dx' \quad (\text{A.7})$$

$$I_2 = \int_{-\infty}^{\infty} e^{-\alpha y'^2 - i\beta_y y'} dy' \quad (\text{A.8})$$

Here,  $\alpha$  and  $\beta$  are defined as

$$\alpha = \frac{1}{\omega^2} - i \frac{k}{2} \left( \frac{1}{R} + \frac{1}{z} \right) \quad (\text{A.9})$$

and

$$\beta_x = \frac{kx}{z}, \quad \beta_y = \frac{ky}{z} \quad (\text{A.10})$$

Recall now the solution to the well-known Gaussian integral:

$$\int_{-\infty}^{\infty} e^{-\alpha\rho^2 - i\beta\rho} d\rho = \sqrt{\frac{\pi}{\alpha}} e^{-\frac{\beta^2}{4\alpha}} \quad (\text{A.11})$$

Applying this formula directly, the integral  $I_2$  gives

$$I_2 = \sqrt{\frac{\pi}{\alpha}} e^{-\frac{\beta_y^2}{4\alpha}} \quad (\text{A.12})$$

On the other hand, to calculate  $I_1$  one can define

$$\hat{\beta}_x = \beta_x - \frac{2\pi n}{P} \quad (\text{A.13})$$

Then, the integral  $I_1$  results in

$$I_1 = \sum_n a_n \int_{-\infty}^{\infty} e^{-\alpha x'^2 - i\hat{\beta}_x x'} dx' = \sum_n a_n \sqrt{\frac{\pi}{\alpha}} e^{-\frac{\hat{\beta}_x^2}{4\alpha}} \quad (\text{A.14})$$

This expression can be rewritten by expanding the  $\hat{\beta}_x$  term:

$$I_1 = \sqrt{\frac{\pi}{\alpha}} e^{-\frac{\beta_x^2}{4\alpha}} \sum_n a_n e^{\left[2\beta_x \left(\frac{2\pi n}{P}\right) / 4\alpha\right]} e^{\left[-\left(\frac{4\pi^2 n^2}{P^2}\right) / 4\alpha\right]} \quad (\text{A.15})$$

Putting these results together, one obtains the solution for the field at the observation plane:

$$U_G(x, y, z) \propto \frac{C}{i\lambda z} \cdot \frac{\pi}{\alpha} e^{-\frac{\beta_x^2 + \beta_y^2}{4\alpha}} \sum_n a_n e^{-\frac{\pi^2 n^2}{\alpha P^2}} e^{\frac{\pi n \beta_x}{\alpha P}} \quad (\text{A.16})$$

The terms before the summation describe free-space propagation of the Gaussian beam, and do not contribute to image formation so they will not be discussed. The terms inside the summation are a consequence of the presence of the periodic object and describe its Fresnel diffraction pattern. For further expansion of the expression, the following relation can be used:

$$|\alpha|^2 = \left(\frac{\omega_z}{\omega}\right)^2 \left(\frac{k}{2z}\right)^2 \quad (\text{A.17})$$

This relation is not trivial to derive, so proof is provided later in this appendix. Applying it to the terms in the summations results in

$$\sum_n a_n e^{-\frac{\pi^2 n^2}{\alpha P^2}} e^{\frac{\pi n \beta_x}{\alpha P}} = \sum_n a_n e^{-\frac{e\pi^2 n^2}{k^2 P^2} \cdot \frac{z^2}{\omega_z^2}} e^{\frac{4\pi n}{kP} \cdot \frac{zx}{\omega_z^2}} e^{-i\pi \lambda \frac{n^2}{P^2} M_u z \frac{\omega_z^2}{\omega_z^2}} e^{i \frac{2\pi n x}{P} M_u \frac{\omega_z^2}{\omega_z^2}} \quad (\text{A.18})$$

This is the full expanded form of the diffracted field from a periodic object, along with the Gaussian envelope given by the free-space propagation term. Here,  $M_u = (R+z)/R$  is called the shadow magnification of the object and is well-known in self-imaging theory with uniform beams, as will become apparent later in this appendix.

### A.1.2 Intermediate relations

The following relation, used during the resolution of the Fresnel integral, will now be proven:

$$|\alpha|^2 = \left(\frac{\omega_z}{\omega}\right)^2 \left(\frac{k}{2z}\right)^2 \quad (\text{A.17 revisited})$$

with

$$\alpha = \frac{1}{\omega^2} - i \frac{k}{2} \left( \frac{1}{R} + \frac{1}{z} \right) \quad (\text{A.9 revisited})$$

The second squared term is straightforward to find. From the definition of  $\alpha$ , its modulus squared is:

$$|\alpha|^2 = \frac{1}{\omega^4} + \frac{k^2}{4} \left( \frac{1}{R} + \frac{1}{z} \right)^2 = \frac{1}{\omega^4} + \frac{k^2}{4} \cdot \frac{(R+z)^2}{R^2 z^2} = \frac{k^2}{4z^2} \left( \frac{4z^2}{\omega^4 k^2} + \frac{(R+z)^2}{R^2} \right) \quad (\text{A.19})$$

The common factor is found to be  $(k/2z)^2$ , and therefore it now suffices to prove that

$$\left( \frac{4z^2}{\omega^4 k^2} + \frac{(R+z)^2}{R^2} \right) = \left( \frac{\omega_z}{\omega} \right)^2 \quad (\text{A.20})$$

In order to do that, consider that the beam waist is located at a position  $d = 0$  in the propagation axis<sup>1</sup>, the object is placed at an arbitrary plane  $d = \gamma$  and the observation plane is located at a distance  $z$  from the object, that is, at  $d = z + \gamma$ . According to the well-known relations for a Gaussian beam, the beam radii at the object and observation planes satisfy

$$\omega^2 = \omega_0^2 \left[ 1 + \left( \frac{\gamma}{z_R} \right)^2 \right] \quad (\text{A.21})$$

$$\omega_z^2 = \omega_0^2 \left[ 1 + \left( \frac{\gamma + z}{z_R} \right)^2 \right] \quad (\text{A.22})$$

---

<sup>1</sup>To avoid confusion, here  $d$  denotes the position in the propagation axis  $z$ , since the symbol  $z$  is used as the distance from the object to the observation plane.

and the wavefront curvature at the object plane is

$$R = \gamma \left[ 1 + \left( \frac{z_R}{\gamma} \right)^2 \right] \quad (\text{A.23})$$

Substituting the values of  $\omega$  and  $\omega_z$  into equation A.20 and then multiplying both sides by  $\omega^2/\omega_0^2$ , one reaches

$$\frac{4z^2}{\omega_0^4 [1 + (\gamma/z_R)^2]} + [1 + (\gamma/z_R)^2] \frac{(R+z)^2}{R^2} = \left[ 1 + \left( \frac{\gamma+z}{z_R} \right)^2 \right] \quad (\text{A.24})$$

The right-hand side of this expression (RHS) can be expanded as follows:

$$RHS = \left[ 1 + \left( \frac{\gamma+z}{z_R} \right)^2 \right] = \left( 1 + \frac{\gamma^2}{z_R^2} \right) + \frac{2\gamma z}{z_R^2} + \frac{z^2}{z_R^2} \quad (\text{A.25})$$

On the other hand, taking the left-hand side (LHS) and substituting  $R$  for its value, as well as  $k = 2\pi/\lambda$  and  $\omega_0^2 = z_R\lambda/\pi$ , one gets

$$LHS = \frac{z^2}{z_R^2 [1 + (\gamma/z_R)^2]} + [1 + (\gamma/z_R)^2] \frac{(\gamma [1 + (z_R/\gamma)^2] + z)^2}{\gamma^2 [1 + (z_R/\gamma)^2]^2} \quad (\text{A.26})$$

The denominator on the second term can be rewritten as

$$\gamma^2 [1 + (z_R/\gamma)^2]^2 = z_R^2 [1 + (\gamma/z_R)^2] [1 + (z_R/\gamma)^2] \quad (\text{A.27})$$

which results in

$$LHS = \frac{z^2}{z_R^2 [1 + (\gamma/z_R)^2]} + \frac{\gamma^2 [1 + (z_R/\gamma)^2]^2 + 2\gamma z [1 + (z_R/\gamma)^2] + z^2}{z_R^2 [1 + (z_R/\gamma)^2]} \quad (\text{A.28})$$

It is convenient to proceed by separating the terms in the sum according to their order in  $z$ . The zeroth and first orders consist of just one term, so they can be solved directly:

$$\frac{\gamma^2 [1 + (z_R/\gamma)^2]^2}{z_R^2 [1 + (z_R/\gamma)^2]} = \frac{\gamma^2}{z_R^2} [1 + (z_R/\gamma)^2] = 1 + \frac{\gamma^2}{z_R^2} \quad (\text{A.29})$$

$$\frac{2z\gamma [1 + (z_R/\gamma)^2]}{z_R^2 [1 + (z_R/\gamma)^2]} = \frac{2\gamma z}{z_R^2} \quad (\text{A.30})$$

The second order term requires a slightly longer, but equally easy calculation:

$$\frac{z^2}{z_R^2 [1 + (\gamma/z_R)^2]} + \frac{z^2}{z_R^2 [1 + (z_R/\gamma)^2]} = \frac{z^2}{z_R^2} \left( \frac{z_R^2}{z_R^2 + \gamma^2} + \frac{\gamma^2}{z_R^2 + \gamma^2} \right) = \frac{z^2}{z_R^2} \quad (\text{A.31})$$

Putting it all together it is found that

$$LHS = \left(1 + \frac{\gamma^2}{z_R^2}\right) + \frac{2\gamma z}{z_R^2} + \frac{z^2}{z_R^2} = RHS \quad (\text{A.32})$$

and the relation is proven.

## A.2 Localization and magnification of images

The last two exponentials in the solution to the Fresnel diffraction integral (eq. A.18) are the most important terms as far as image formation is concerned, since they account for the localization and magnification of the images, respectively.

From the localization term one can see that all diffraction orders are in phase (meaning that the phase of the exponential is a multiple of either  $\pi$  or  $2\pi$ , following the argument given in section 3.1.1) whenever the distance  $z$  satisfies the following relation:

$$\nu \frac{P^2}{\lambda} = z M_u \left(\frac{\omega}{\omega_z}\right)^2 = z \frac{R+z}{R} \left(\frac{\omega}{\omega_z}\right)^2 \quad (\text{A.33})$$

where  $\nu$  is a positive integer. This expression accounts both for images shifted by half the object period as well as direct images. The images are not shifted whenever  $\nu$  is even.

Regarding the lateral magnification  $M_G$  of the diffraction patterns caused by the Gaussian beam illumination, it can be obtained from the last exponential term in the integral solution:

$$M_G = \left(\frac{\omega_z}{\omega}\right)^2 M_u^{-1} = \left(\frac{\omega_z}{\omega}\right)^2 \frac{R}{R+z} \quad (\text{A.34})$$

The localization condition and magnification obtained above apply for the general case of a Gaussian beam. These expressions simplify for some specific cases [48] that are introduced below.

### A.2.1 Object placed at beam waist

A special case when dealing with Gaussian beam illumination occurs when the object is place in the beam waist plane. Then,  $R \rightarrow \infty$  (plane wavefront illumination at the object plane) and therefore the magnification becomes

$$M_{G0} = \left(\frac{\omega_z}{\omega_0}\right)^2 \quad (\text{A.35})$$

This change in lateral magnification with the propagation distance has the hyperbolic character inherent to Gaussian beam propagation. Similarly, the localization of images satisfies the relation

$$z = \nu \frac{P^2}{\lambda} \left(\frac{\omega_z}{\omega_0}\right)^2 \quad (\text{A.36})$$

### A.2.2 Spherical wavefront illumination

For uniform illumination (e.g. a spherical wavefront),  $\omega \rightarrow \infty$  and  $(\omega/\omega_z)^2 = M_u^{-2}$ . Under these conditions the solution to the Fresnel integral becomes

$$U_u(x, y, z) = \sum_n a_n e^{-i\pi\lambda \frac{n^2}{P^2} \cdot \frac{Rz}{R+z}} e^{i\frac{2\pi n x}{P} \cdot \frac{R}{R+z}} \quad (\text{A.37})$$

From this expression, the relation for axial localization of self-images, after isolating the position  $z$ , is found to be:

$$z = \frac{\nu P^2 R}{\lambda R - \nu P^2} \quad (\text{A.38})$$

Moreover, the lateral magnification is found to be equal to  $M_u = (R + z)/z$ , thus explaining the definition of this factor presented earlier in this appendix.

### A.2.3 Plane-wave illumination

Plane wave illumination represents a special case of uniform illumination, and is the most common type of illumination used in self-imaging applications. It can be obtained from the spherical wavefront case by setting  $R \rightarrow \infty$ , which results in

$$U_{u'}(x, y, z) = \sum_n a_n e^{-i\pi\lambda \frac{n^2}{P^2} z} e^{i\frac{2\pi n x}{P}} \quad (\text{A.39})$$

This way the expression found for the Talbot effect in section 3.1.1 is recovered. It follows that the self-images appear at  $z = \nu P^2 / \lambda$  with a magnification of  $M_{u'} = 1$ .

## A.3 Beam expression in 1D

The usual definition of a Gaussian beam, as used in this appendix, is obtained by considering diffraction of the beam in two dimensions. However, the simulations in this project are performed only in one dimension. For this reason, the formula for the Gaussian beam must be adapted in order for it to be consisted with the 1D diffraction formulas.

To do this, consider a one-dimensional field with a Gaussian shape at the initial plane (which is, in fact, the beam waist plane):

$$U_G(x, 0) = A e^{-\frac{x^2}{\omega_0^2}} \quad (\text{A.40})$$

where  $A$  accounts for the maximum amplitude of the field and  $\omega_0$  the beam waist.

The general expression for the beam is obtained by propagating the field to an arbitrary distance  $z$  (in the paraxial approximation). If the 2D Fresnel formula is used, one recovers the conventional expression. Instead, one can assume that the field is constant in the  $y$  direction and perform the integral over this coordinate. This results in the one-dimensional Fresnel diffraction formula:

$$U(x, z) = \frac{e^{ikz}}{\sqrt{i\lambda z}} \int_{-\infty}^{\infty} U(x, 0) e^{i\frac{k}{2z}(x-x')^2} dx' \quad (\text{A.41})$$

Substituting the proposed initial field one finds the integral to be solved:

$$U_G(x, z) = A \frac{e^{ikz}}{\sqrt{i\lambda z}} e^{i\frac{k}{2z}x^2} \int_{-\infty}^{\infty} e^{-x'^2\sigma} e^{-i2\pi\frac{x}{\lambda z}x'} dx' \quad (\text{A.42})$$

where  $\sigma = \frac{1}{\omega_0^2} - i\frac{k}{2z}$  has been defined for convenience. Also, it has been used that  $k = 2\pi/\lambda$ . Notice that the integral is actually the Fourier transform of a Gaussian function, evaluated at  $f_x = \frac{x}{\lambda z}$ . The result of this transform is well-known, so one obtains:

$$U_G(x, z) = A \frac{e^{ikz}}{\sqrt{i\lambda z}} e^{i\frac{k}{2z}x^2} \sqrt{\frac{\pi}{\sigma}} e^{-\frac{\pi^2 x^2}{\lambda^2 z^2 \sigma}} \quad (\text{A.43})$$

The goal now is to expand this expression into the conventional shape for a Gaussian beam. For that purpose, one can rewrite it as

$$U_G(x, z) = A e^{ikz} B e^\phi \quad (\text{A.44})$$

where

$$B = \sqrt{\frac{\pi}{i\lambda z \sigma}} = \frac{1}{\sqrt{i\frac{2z}{k}\sigma}} \quad (\text{A.45})$$

and

$$\phi = i\frac{k}{2z}x^2 - \frac{\pi^2 x^2}{\lambda^2 z^2 \sigma} \quad (\text{A.46})$$

On the one hand, B is straightforward to obtain by expanding  $\sigma$ :

$$B = \frac{1}{\sqrt{i\frac{2z}{k\omega_0^2} + 1}} = \sqrt{\frac{\omega_0}{\omega_z}} e^{-\frac{i}{2} \arctan\left(\frac{z}{z_R}\right)} \quad (\text{A.47})$$

On the other hand, recall that  $|\sigma|^2 = \left(\frac{k}{2z}\right)^2 \left(\frac{\omega_z}{\omega_0}\right)^2$ . This is the same relation that has been demonstrated in section A.1.2 of this appendix, for the particular case that  $\gamma = 0$  ( $R \rightarrow \infty$  and  $\omega = \omega_0$ ). Applying this to equation A.46:

$$\phi = -\frac{\pi^2 x^2}{\lambda^2 z^2} \cdot \frac{1/\omega_0^2}{\left(\frac{k}{2z}\right)^2 \left(\frac{\omega_z}{\omega_0}\right)^2} + ix^2 \left( \frac{k}{2z} - \frac{\pi^2}{\lambda^2 z^2} \cdot \frac{k/2z}{\left(\frac{k}{2z}\right)^2 \left(\frac{\omega_z}{\omega_0}\right)^2} \right) \quad (\text{A.48})$$

After applying the expression for  $\omega_z$  in the imaginary term and performing some basic algebra, one reaches

$$\phi = -\frac{x^2}{\omega_z^2} + ix^2 \frac{k}{2} \cdot \frac{1}{z \left[ \left( \frac{z_R}{z} \right)^2 + 1 \right]} = -\frac{x^2}{\omega_0^2} + ix^2 \frac{k}{2R_z} \quad (\text{A.49})$$

where  $R_z$  is the radius of curvature at  $z$ . Putting it all together again the field is written as desired:

$$U_G(x, z) = A \sqrt{\frac{\omega_0}{\omega_z}} e^{-\frac{x^2}{\omega_z^2}} e^{i \frac{kx^2}{2R_z}} e^{i(kz - \frac{1}{2} \arctan(z/z_R))} \quad (\text{A.50})$$

It is quickly seen that the difference between this expression and the conventional two-dimensional Gaussian beam is that the beam waist radius contribution to the amplitude is square-rooted, as well as the Gouy phase term.

# Appendix B

## Contrast calculation

Contrast, or visibility, is an important figure when it comes to evaluating intensity patterns with a periodic behaviour. Its most standard definition [67] is the following:

$$C = \frac{I_{max} - I_{min}}{I_{max} + I_{min}} \quad (\text{B.1})$$

In practice, however, direct application of this formula can often lead to unwanted results. In this section some alternative approaches for the measurement of contrast are presented, depending on the context where it is used.

The first approach can be applied when dealing with self-images from a binary grating with a 50% duty cycle [68], no matter whether they are transmission or phase gratings. The contrast can be measured with a periodic mask with the same period ( $P$ ) as the grating, for instance another binary transmission grating. The maximum intensity is taken to be the integration of the intensity between  $x = -P/4$  and  $x = P/4$ , whereas the minimum intensity is the integration between  $x = P/4$  and  $x = 3P/4$ . Then, the standard formula can be used with this new parameters. This method has the advantage that the contrast is easily measured and experimental fluctuations are avoided. In the particular case of a  $\pi$ -phase grating the analyzer grating should have half the period, since the frequency of the intensity patterns it produces is double (see section 3.1.3).

The second approach comes useful when the pattern has the shape of a sinusoid:

$$I_s(x) = A + B \sin\left(\frac{2\pi x}{P} + \phi\right) \quad (\text{B.2})$$

where  $A$ ,  $B$  and  $\phi$  are the mean, amplitude and phase of the sinusoidal function. Applying the definition of contrast, one finds that

$$C_s = \frac{B}{A} \quad (\text{B.3})$$

As a result, the contrast is readily found by simply fitting a sine to the data. Often times the pattern that one encounters is not directly a sinusoid, but instead it is modulated by another function:

$$I(x) = I_{ref}(x)I_s(x) \quad (\text{B.4})$$

For instance, this occurs in the two-phase grating moiré interferometer, where the periodic pattern is modulated by a Gaussian shape. In this case, one can assume that the modulation function is the beam at the camera when the object (or objects) that causes the fringes is removed (e.g. the gratings). Then, dividing  $I/I_{ref}$  leaves only the periodic contribution.

Instead of performing a fit, the contrast of a periodic pattern of frequency  $f$  can be computed as follows. Considering that the signal has a mean, periodic noise  $N$  and a periodic component:

$$U(x) = A + B\sin(2\pi fx + \phi) + N(x) \quad (\text{B.5})$$

On the one hand, the mean amplitude  $A$  can be extracted from the zeroth order term in a Fourier Series:

$$a_0 = \frac{f}{2} \int_{-1/f}^{1/f} U(x) dx = \frac{A}{2} \quad (\text{B.6})$$

On the other hand, the amplitude of the fringes is obtained from the first order coefficients of the series:

$$a_1 = \frac{f}{2} \int_{-1/f}^{1/f} U(x)\cos(2\pi fx) dx = B \frac{\sin(\phi)}{2} \quad (\text{B.7})$$

$$b_1 = \frac{f}{2} \int_{-1/f}^{1/f} U(x)\sin(2\pi fx) dx = B \frac{\cos(\phi)}{2} \quad (\text{B.8})$$

$$\therefore B = 2\sqrt{a_n^2 + b_n^2} \quad (\text{B.9})$$

Therefore, if the noise and signal are of different frequencies one can measure the contrast by computing these Fourier coefficients, regardless of the phase of the signal. This method can be extended to the case of the continuous Fourier Transform. Using the same function, its Fourier transform is given by:

$$\mathcal{F}[U](f_x) = A\delta(f_x) + \frac{B}{2} [e^{i\phi}\delta(f_x - f) + e^{-i\phi}\delta(f_x + f)] + \mathcal{F}[N(x)] \quad (\text{B.10})$$

Assuming that the noise is periodic with frequency  $f_N$  and has null mean, its Fourier Transform can be regarded as  $\delta(f_x \pm f_N)$ . Then, the coefficients  $A$  and  $B$  are obtained by evaluating the Fourier Transform at the proper frequency. One advantage of this method is that it allows calculation of contrast even if the fringes are not very clear because of the contribution of other frequency terms. Another advantage is that it can be used to calculate the actual frequency of the fringes, a task at which the fitting method often fails. The downside is that its accuracy is limited by the resolution of the FFT, which is related to the size of the sampling space.

# Appendix C

## Theoretical considerations of the moiré interferometer

In this appendix the full theoretical developments for the 2-grating and 3-grating moiré interferometers is presented, along with the conclusions that can be obtained from it. This calculations are an extension of the results in the *Methods* section of ref. [24]. At all times it is assumed that the wavelength is much smaller than the period of the gratings, and that the gratings act as a multiplicative transmission function on the complex amplitude of the field.

The following notation will be used throughout this section:

- $(x_s, y_s)$ : coordinates in the source plane
- $(x_1, y_1)$ : coordinates in the first grating plane
- $(x_2, y_2)$ : coordinates in the second grating plane
- $(x_3, y_3)$ : coordinates in the third grating plane
- $(x, y)$ : coordinates in the observation plane
- $L_1$ : distance from the source to the first grating
- $D$ : distance between the two gratings in the two-grating system
- $D_1$ : distance between the first two gratings in the three-grating system
- $L_2$ : distance from the second grating to the observation plane in the two-grating system; distance from the second grating to the virtual-image plane in the three-grating system
- $D_3$ : distance from the second grating to the third grating in the three-grating system
- $L_3$ : distance from the third grating to the observation plane in the three-grating system
- $L'$ : distance from the source to the third grating in the three-grating system
- $L$ : total distance from the source to the detection plane
- $f_1$ : spatial frequency of the first grating
- $f_2$ : spatial frequency of the second grating
- $f_3$ : spatial frequency of the third grating

## C.1 Two-grating system

### C.1.1 Field at the observation plane

Consider a system consisting of four planes of interest: a source, two gratings and an arbitrary observation plane. The field at the end of this system is related to the field at the source  $V_0$  by:

$$V(x, y) \propto \iiint \frac{1}{r_0 r_1 r_2} V_0(x_s, y_s) T_1(x_1, y_1) T_2(x_2, y_2) e^{ik(r_0+r_1+r_2)} dS_0 dS_1 dS_2 \quad (\text{C.1})$$

where  $r_j$  denote the distances between any two points in adjacent planes:

$$r_0 = \sqrt{(x_1 - x_s)^2 + (y_1 - y_s)^2 + L_1^2} \quad (\text{C.2})$$

$$r_1 = \sqrt{(x_2 - x_1)^2 + (y_2 - y_1)^2 + D^2} \quad (\text{C.3})$$

$$r_2 = \sqrt{(x - x_2)^2 + (y - y_2)^2 + L_2^2} \quad (\text{C.4})$$

The differentials  $dS_0$ ,  $dS_1$  and  $dS_2$  indicate that the integral is performed over the area of the source, first grating and second grating, respectively. The expression above is reached by successive application of the Rayleigh-Sommerfeld formula between consecutive planes. It has been assumed that, in each steps, the propagation distance  $z$  is much larger than the lateral extension of the field, and so  $z \approx r_j$ . Furthermore,  $r_j \gg \lambda$ .

One can ignore the integral over  $S_0$  by considering that the initial field is a point source. If that were not the case, the final expression may be integrated over this coordinate. Similarly, the source is assumed to be monochromatic; for polychromatic beams the solution should be averaged over their spectrum.

Next, consider the gratings to have their fringes along the  $y$  direction but to be constant in  $x$ . Consequently, the  $x$ -coordinate can be ignored altogether since it will become a constant when the paraxial approximation is applied and thus will fall under the proportionality sign. Since the gratings are assumed to be infinite and periodic, their transmission functions take the form of a Fourier Series:

$$T_1(y_1) = \sum_m A_m e^{i2\pi m f_1 y_1} \quad (\text{C.5})$$

$$T_2(y_2) = \sum_n B_n e^{i2\pi n f_2 y_2} \quad (\text{C.6})$$

To apply the paraxial approximation, each propagation is treated independently. That is to say, each  $r_j = r(y - y')$  is approximated separately. The Taylor expansion up to second order of the square root around  $y'$  is given by:

$$r(y - y') = r(y') + \frac{\partial r}{\partial y} \Big|_{y'} (y - y') + \frac{1}{2} \cdot \frac{\partial^2 r}{\partial y^2} \Big|_{y'} (y - y')^2 \quad (\text{C.7})$$

To ensure that this approximation holds, the results in ref. [69] were reproduced successfully. Essentially, it means that each propagation from one plane to the next is done practically along the direction of the z axis, with only a small deviation. The series for each  $r_j$  term is:

$$r_0 \approx L_1 + \frac{1}{2L_1}(y_1 - y_s)^2 \quad (\text{C.8})$$

$$r_1 \approx D + \frac{1}{2D}(y_2 - y_1)^2 \quad (\text{C.9})$$

$$r_2 \approx L_2 + \frac{1}{2L_2}(y - y_2)^2 \quad (\text{C.10})$$

Using this, and conveniently rearranging terms so that the integral over  $y_1$  is made easier, the sum of the three distances becomes:

$$\begin{aligned} r_0 + r_1 + r_2 &\approx (L_1 + D + L_2) + \frac{1}{2} \left( \frac{1}{L_1} + \frac{1}{D} \right) y_1^2 - \left( \frac{y_s}{L_1} + \frac{y_2}{D} \right) y_1 \\ &\quad + \frac{1}{2} \left( \frac{y_s^2}{L_1} + \frac{y_2^2}{D} \right) + \frac{1}{2L_2}(y - y_2)^2 \end{aligned} \quad (\text{C.11})$$

As is usual in the paraxial approximation and unlike the phase terms, the amplitude factors are only taken up first order, so  $1/(r_0 r_1 r_2) \approx 1/(L_1 D L_2)$  and it can be taken out of the integral to fall under the proportionality sign. Taking everything into account, equation C.1 is reduced to:

$$\begin{aligned} V &\propto \sum_{m,n} A_m B_n e^{ik(L_1+D+L_2)} \\ &\times \int dy_2 e^{i2\pi n f_2 y_2} \exp \left( \frac{ik}{2} \left( \frac{y_s^2}{L_1} + \frac{y_2^2}{D} \right) \right) \exp \left( \frac{ik}{2L_2}(y - y_2)^2 \right) \\ &\times \int dy_1 e^{i2\pi m f_1 y_1} \exp \left( \frac{ik}{2} \left( \frac{1}{L_1} + \frac{1}{D} \right) \right) \exp \left( -ik \left( \frac{y_s}{L_1} + \frac{y_2}{D} \right) y_1 \right) \end{aligned} \quad (\text{C.12})$$

Notice that the second integral is inside the first one and they cannot be separated. Recall now the Gaussian integral formula:

$$\int_{-\infty}^{\infty} e^{-ax^2+bx} = \sqrt{\frac{\pi}{a}} e^{\frac{b^2}{4a}} \quad (\text{C.13})$$

To solve the integral for  $y_1$ , take:

$$a = -ik \frac{1}{2} \left[ \frac{1}{L_1} + \frac{1}{D} \right] \quad (\text{C.14})$$

$$b = i2\pi m f_1 - ik \left[ \frac{y_s}{L_1} + \frac{y_2}{D} \right] \quad (\text{C.15})$$

$$b^2 = (i2\pi m f_1)^2 + (ik)^2 \left[ \frac{y_s}{L_1} + \frac{y_2}{D} \right]^2 - 2(i2\pi m f_1) \left( ik \left[ \frac{y_s}{L_1} + \frac{y_2}{D} \right] \right) \quad (\text{C.16})$$

Expanding the terms and operating, one reaches:

$$b^2/4a = -\frac{(i2\pi mf_1)^2}{i2k[1/L_1 + 1/D]} + \frac{(i2\pi mf_1)y_s/L_1}{[1/L_1 + 1/D]} + \frac{(i2\pi mf_1)y_2/D}{[1/L_1 + 1/D]} - \frac{ik(y_s/L_1)^2}{2[1/L_1 + 1/D]} - \frac{ik(y_2/D)^2}{2[1/L_1 + 1/D]} - \frac{ik(y_s/L_1)(y_2/D)}{[1/L_1 + 1/D]} \quad (\text{C.17})$$

Then, ignoring the constant amplitude term, the field becomes:

$$\begin{aligned} V \propto & e^{ik(L_1+D+L_2)} \exp\left(\frac{iky_s^2}{2L_1}\right) \exp\left(\frac{iky^2}{2L_2}\right) \exp\left(-\frac{ik(y_s/L_1)^2}{2[1/L_1 + 1/D]}\right) \\ & \times \sum_{m,n} A_m B_n \exp\left(-\frac{(i2\pi mf_1)^2}{i2k[1/L_1 + 1/D]}\right) \exp\left(\frac{(i2\pi mf_1)(y_s/L_1)}{[1/L_1 + 1/D]}\right) \\ & \times \int dy_2 e^{i2\pi n f_2 y_2} \exp\left(ik\frac{y_2^2}{2D}\right) \exp\left(ik\frac{yy_2}{L_2}\right) \exp\left(ik\frac{y_2^2}{2L_2}\right) \\ & \times \exp\left(\frac{(i2\pi mf_1)(y_2/D)}{[1/L_1 + 1/D]}\right) \exp\left(-\frac{ik(y_2/D)^2}{2[1/L_1 + 1/D]}\right) \\ & \times \exp\left(-\frac{ik(y_s/L_1)(y_2/D)}{[1/L_1 + 1/D]}\right) \end{aligned} \quad (\text{C.18})$$

The integral for  $y_2$  now also has a Gaussian shape, so it can be solved using the same formula. The coefficients are now slightly more complex:

$$a' = -\frac{ik}{2} \left[ \frac{1}{D} + \frac{1}{L_2} \right] + \frac{ik}{2D^2[1/L_1 + 1/D]} \quad (\text{C.19})$$

$$b' = i2\pi n f_2 + \frac{i2\pi mf_1}{D/L_1 + 1} - ik\frac{y}{L_2} - ik\frac{y_s}{D + L_1} \quad (\text{C.20})$$

$$\begin{aligned} b'^2 = & \left( i2\pi n f_2 + \frac{i2\pi mf_1}{D/L_1 + 1} \right)^2 + (ik)^2 \left( \frac{y}{L_2} + \frac{y_s}{D + L_1} \right)^2 \\ & - 2ik \left( i2\pi n f_2 + \frac{i2\pi mf_1}{D/L_1 + 1} \right) \left( \frac{y}{L_2} + \frac{y_s}{D + L_1} \right) \end{aligned} \quad (\text{C.21})$$

The expression for  $a'$  can be reduced to:

$$a' = -\frac{ik}{2} \left[ \frac{1}{D} + \frac{1}{L_2} - \frac{L_1}{(D + L_1)D} \right] \quad (\text{C.22})$$

Then, the phase of the integral solution is given by:

$$\begin{aligned} b^2/4a = & -\frac{\left( i2\pi n f_2 + \frac{i2\pi mf_1}{D/L_1 + 1} \right)^2}{i2k \left[ \frac{1}{D} + \frac{1}{L_2} - \frac{L_1}{(D + L_1)D} \right]} - \frac{ik \left( \frac{y}{L_2} + \frac{y_s}{D + L_1} \right)^2}{2 \left[ \frac{1}{D} + \frac{1}{L_2} - \frac{L_1}{(D + L_1)D} \right]} \\ & + \frac{\left( i2\pi n f_2 + \frac{i2\pi mf_1}{D/L_1 + 1} \right) \left( \frac{y}{L_2} + \frac{y_s}{D + L_1} \right)}{\left[ \frac{1}{D} + \frac{1}{L_2} - \frac{L_1}{(D + L_1)D} \right]} \end{aligned} \quad (\text{C.23})$$

Finally, the whole integral from equation C.12 is solved:

$$\begin{aligned}
V \propto & e^{ik(L_1+D+L_2)} \exp\left(\frac{iky_s^2}{2L_1}\right) \exp\left(\frac{iky^2}{2L_2}\right) \exp\left(-\frac{ik(y_s/L_1)^2}{2[1/L_1 + 1/D]}\right) \\
& \times \exp\left(-\frac{ik\left(\frac{y}{L_2} + \frac{y_s}{D+L_1}\right)^2}{2\left[\frac{1}{D} + \frac{1}{L_2} - \frac{L_1}{(D+L_1)D}\right]}\right) \\
& \times \sum_{m,n} A_m B_n \\
& \times \exp\left(\frac{i2\pi m f_1 (y_s/L_1)}{[1/L_1 + 1/D]}\right) \exp\left(\frac{\left(i2\pi n f_2 + \frac{i2\pi m f_1}{D/L_1 + 1}\right)\left(\frac{y}{L_2} + \frac{y_s}{D+L_1}\right)}{\left[\frac{1}{D} + \frac{1}{L_2} - \frac{L_1}{(D+L_1)D}\right]}\right) \\
& \times \exp\left(-\frac{(i2\pi m f_1)^2}{i2k[1/L_1 + 1/D]}\right) \exp\left(-\frac{\left(i2\pi n f_2 + \frac{i2\pi m f_1}{D/L_1 + 1}\right)^2}{i2k\left[\frac{1}{D} + \frac{1}{L_2} - \frac{L_1}{(D+L_1)D}\right]}\right)
\end{aligned} \tag{C.24}$$

The terms in the expression above have been conveniently written in the form

$$V \propto e^{ikL/\cos\theta} \sum_{m,n} A_m B_n e^{i\phi_0(m,n) + i\phi_1(m,n)} \tag{C.25}$$

Notice that the terms in front of the summation depend proportionally on  $k$ , the terms that determine  $\phi_0$  do not depend on  $k$ , and the terms that determine  $\phi_1$  depend inversely on  $k$ . In pursuit of recovering the expression in ref. [24], each of these three parts of the expression will be analyzed separately.

First, take the terms in front of the summation, which are directly proportional to  $k$ . Denoting by  $\phi$  the phase of these terms:

$$\phi = kL + \frac{k}{2} \cdot \frac{y_s^2}{L_1} + \frac{k}{2} \cdot \frac{y^2}{L_2} - \frac{k}{2} \cdot \frac{y_s^2/L_1^2}{[1/L_1 + 1/D]} - \frac{k}{2} \frac{\left(\frac{y}{L_2} + \frac{y_s}{D+L_1}\right)^2}{\left[\frac{1}{D} + \frac{1}{L_2} - \frac{L_1}{D(D+L_1)}\right]} \tag{C.26}$$

In the first term it has been used that  $L = L_1 + D + L_2$ . Focusing on the quadratic phase terms, they can be expanded (ignoring the  $k/2$  factor) into

$$\phi' = \frac{y^2}{L_2} + \frac{y_s^2}{L_1} - \frac{y_s^2/L_1^2}{[1/L_1 + 1/D]} - \frac{\left(\frac{y}{L_2}\right)^2 + 2\left(\frac{y}{L_2}\right)\left(\frac{y_s}{D+L_1}\right) + \left(\frac{y_s}{D+L_1}\right)^2}{\left[\frac{1}{D} + \frac{1}{L_2} - \frac{L_1}{D(D+L_1)}\right]} \tag{C.27}$$

From here, the terms depending on  $y^2$ ,  $y_s^2$  and  $yy_s$  can be reduced separately. Skipping intermediate steps, one reaches:

$$[y_s^2] = 1/L \quad (C.28)$$

$$[y^2] = 1/L \quad (C.29)$$

$$[yy_s] = -2/L \quad (C.30)$$

Therefore,

$$\phi' = \frac{y_s^2}{L} + \frac{y^2}{L} - \frac{2yy_s}{L} = \frac{(y - y_s)^2}{L} \quad (C.31)$$

Now, one has to notice the following:

$$\frac{L}{\cos\theta} = \sqrt{L^2 + (y - y_s)^2} \approx L + \frac{1}{2L}(y - y_s)^2 \quad (C.32)$$

Putting back the simplified expression for  $\phi'$  into equation C.26, and applying the relation above, one gets that the phase of the term before the summation in equation C.24 is:

$$\phi = k \left[ L + \frac{1}{2L}(y - y_s)^2 \right] \approx kL/\cos\theta \quad (C.33)$$

Next,  $\phi_0$  must be determined from the terms that do not depend on  $k$ . From equation C.24:

$$\phi_0 = \frac{(2\pi m f_1)(y_s/L_1)}{[1/L_1 + 1/D]} + \frac{\left(2\pi n f_2 + \frac{2\pi m f_1}{D/L_1+1}\right) \left(\frac{y}{L_2} + \frac{y_s}{D+L_1}\right)}{\left[\frac{1}{D} + \frac{1}{L_2} - \frac{L_1}{(D+L_1)D}\right]} \quad (C.34)$$

The calculation is performed here by separating the terms that depend on  $m$  and those that depend on  $n$ . Inside of each of those cases, the terms depending on  $y$  and  $y_s$  are also treated independently. After simplifying, the following expression is reached:

$$\phi_0 = 2\pi m f_1 \left( y_s \frac{D+L_2}{L} + y \frac{L_1}{L} \right) + 2\pi n f_2 \left( y_s \frac{L_2}{L} + y \frac{D+L_1}{L} \right) \quad (C.35)$$

Last, the remaining terms in equation C.24 are the ones that are inversely proportional to  $k$ . Therefore,  $\phi_1$  is

$$\phi_1 = -\frac{(2\pi m f_1)^2}{2k[1/L_1 + 1/D]} - \frac{\left(2\pi n f_2 + \frac{2\pi m f_1}{D/L_1+1}\right)^2}{2k \left[\frac{1}{D} + \frac{1}{L_2} - \frac{L_1}{(D+L_1)D}\right]} \quad (C.36)$$

Following the same strategy, one can analyze separately the terms depending on  $m^2$ ,  $n^2$  and  $mn$ , which resolve to the following:

$$[m^2] = -\frac{1}{2k}(2\pi m f_1)^2 \left( L_1 - \frac{L_1^2}{L} \right) \quad (\text{C.37})$$

$$[n^2] = -\frac{1}{2k}(2\pi n f_2)^2 \left( L_2 - \frac{L_2^2}{L} \right) \quad (\text{C.38})$$

$$[mn] = -\frac{2}{2k}(2\pi m f_1)(2\pi n f_2) \frac{L_1 L_2}{L} \quad (\text{C.39})$$

Adding them and rearranging, one gets that

$$\phi_1 = -\frac{L}{2k} \left[ (2\pi m f_1)^2 \frac{L_1}{L} + (2\pi n f_2)^2 \frac{L_2}{L} - \left( 2\pi m f_1 \cdot \frac{L_1}{L} - 2\pi n f_2 \cdot \frac{L_2}{L} \right)^2 \right] \quad (\text{C.40})$$

In summary, the field amplitude after the two-grating system (eq. C.24) is found to be:

$$V \propto e^{ikL/\cos\theta} \sum_{m,n} A_m B_n e^{i\phi_0(m,n) + i\phi_1(m,n)} \quad (\text{C.25 revisited})$$

with

$$\phi_0 = 2\pi m f_1 \left( y_s \frac{D + L_2}{L} + y \frac{L_1}{L} \right) + 2\pi n f_2 \left( y_s \frac{L_2}{L} + y \frac{D + L_1}{L} \right) \quad (\text{C.35 revisited})$$

$$\phi_1 = -\frac{L}{2k} \left[ (2\pi m f_1)^2 \frac{L_1}{L} + (2\pi n f_2)^2 \frac{L_2}{L} - \left( 2\pi m f_1 \cdot \frac{L_1}{L} - 2\pi n f_2 \cdot \frac{L_2}{L} \right)^2 \right] \quad (\text{C.40 revisited})$$

### C.1.2 moiré fringes

Once the complex amplitude of the field is known its intensity must be obtained, since it is the magnitude that can be measured directly by means of a camera. From the expression given above, the intensity pattern at the observation plane is:

$$H(\lambda) = |V(y)|^2 \propto \sum_{\substack{m,n \\ m',n'}} A_m B_n A_{m'}^* B_{n'}^* e^{i(\phi_0(m,n) + \phi_1(m,n) - \phi_0(m',n') - \phi_1(m',n'))} \quad (\text{C.41})$$

To analyze this expression, one can start by studying the dependence of the pattern on the spatial coordinate  $y$ . Notice that it only appears in  $\phi_0$ , and not in  $\phi_1$ . Then, using  $m' = m + r$  and  $n' = n - s$ , one has that

$$\begin{aligned} \phi_0(m, n) - \phi_0(m + r, n - s) &= -2\pi r f_1 \left( \frac{L_1}{L} y + \frac{D + L_2}{L} y_s \right) \\ &\quad + 2\pi s f_2 \left( \frac{L_1 + D}{L} y + \frac{L_2}{L} y_s \right) \end{aligned} \quad (\text{C.42})$$

According to this, the intensity can be expressed as a summation over all possible values of the integers  $r$  and  $s$ , each term of which forms a pattern with a certain wavelength-independent frequency given by:

$$f_y = -rf_1 \frac{L_1}{L} + sf_2 \frac{L_1 + D}{L} \quad (\text{C.43})$$

In particular, the moiré effect arises from the term  $r = s = 1$  (and also  $r = s = -1$ , which will be accounted for later on). In this case, the phase difference between the  $A_m B_n$  and  $A_{m+1} B_{n-1}$  terms in equation C.41 is comprised of an achromatic part, coming from  $\phi_0$ , and a wavelength-dependent part, coming from  $\phi_1$ :

$$\begin{aligned} \phi_0(m, n) - \phi_0(m+1, n-1) &= 2\pi \left( f_2 \frac{L_1 + D}{L} - f_1 \frac{L_1}{L} \right) y \\ &\quad + 2\pi \left( f_2 \frac{L_2}{L} - f_1 \frac{D + L_2}{L} \right) y_s \end{aligned} \quad (\text{C.44})$$

$$\phi_1(m, n) - \phi_1(m+1, n-1) = 2\pi \left( m + \frac{1}{2} \right) \delta_1(\lambda) - 2\pi \left( n - \frac{1}{2} \right) \delta_2(\lambda) \quad (\text{C.45})$$

where  $\delta_j$  have been defined as:

$$\delta_1(\lambda) = \frac{\lambda}{L} f_1 L_1 [(f_1 - f_2)L_2 + f_1 D] \quad (\text{C.46})$$

$$\delta_2(\lambda) = \frac{\lambda}{L} f_2 L_2 [(f_2 - f_1)L_1 + f_2 D] \quad (\text{C.47})$$

The contribution of the considered terms to the intensity at the detector is

$$H_1(\lambda) = e^{i\left(\frac{2\pi y}{P_d} - \frac{2\pi y_s}{P_s}\right)} \sum_m A_m A_{m+1}^* e^{i2\pi(m+1/2)\delta_1} \sum_n B_n B_{n-1}^* e^{-2\pi(n-1/2)\delta_2} \quad (\text{C.48})$$

The exponential term in front has some interesting implications. One of them is that the pattern has a cyclic dependence on the source position, with a period (called the source period) of

$$P_s = \frac{L}{(f_1 - f_2)L_2 + f_1 D} \quad (\text{C.49})$$

Most importantly, the dependence in  $y$  confirms that the pattern is indeed periodic at the moiré frequency, as was expected from the previous discussion. Equivalently, its period is equal to:

$$P_d = \frac{L}{(f_2 - f_1)L_1 + f_2 D} \quad (\text{C.50})$$

The summations in equation C.48 are actually the result of evaluating what is known in waveform analysis as the ambiguity function (or cyclic autocorrelation function in signal processing) of the gratings' transmission profiles:

$$\begin{aligned}\chi_1(\delta_1 P_1, f_1) &= \sum_m A_m A_{m+1}^* e^{i2\pi(m+1/2)\delta_1} \\ &= \frac{1}{P_1} \int_0^{P_1} T_1(\xi + \delta_1 P_1/2) T_1^*(\xi - \delta_1 P_1/2) e^{i2\pi\xi f_1} d\xi\end{aligned}\quad (\text{C.51})$$

$$\begin{aligned}\chi_2^*(\delta_2 P_2, f_2) &= \sum_n B_n B_{n-1}^* e^{-i2\pi(n-1/2)\delta_2} \\ &= \left[ \frac{1}{P_2} \int_0^{P_2} T_2(\xi + \delta_2 P_2/2) T_2^*(\xi - \delta_2 P_2/2) e^{i2\pi\xi f_2} d\xi \right]^*\end{aligned}\quad (\text{C.52})$$

It is also found from this relation that each of the coefficients  $\delta_j$  corresponds to the autocorrelation distance of the  $j$ th grating.

Now, from equation C.43 it is clear that when the sign of both  $r$  and  $s$  is inverted, the resulting frequency is the same except that it has the opposite sign. In particular, as was mentioned earlier, the term for  $r = s = -1$  also contributes to the pattern at the moiré frequency. Then, the full intensity pattern can be written as

$$H = H_0 + H_1 + H_{-1} + [...] \quad (\text{C.53})$$

where  $H_0$  is the term with  $r = s = 0$  (null frequency),  $H_{-1}$  is the one with  $r = s = -1$  and [...] denotes the rest of the terms, which have a different frequency. It is straightforward to check that  $H_{-1} = H_1^*$ . Then, writing the ambiguity functions as  $\chi_j = |\chi_j| \exp(i\varphi_j)$ , the intensity is:

$$H \sim H_0 + 2|\chi_1||\chi_2| \cos \left( \frac{2\pi y}{P_d} + \frac{2\pi y_s}{P_s} + \varphi_1 - \varphi_2 \right) \quad (\text{C.54})$$

The sinusoidal shape of the pattern is now apparent. The contrast of the fringes is defined as their amplitude normalized with the mean intensity (see appendix B), and therefore it is given by:

$$C = \frac{2|H_1(\lambda)|}{H_0} = \frac{|\chi_1(\delta_1 P_1, f_1)|}{\langle T_1 T_1^* \rangle} \cdot \frac{|\chi_2(\delta_2 P_2, f_2)|}{\langle T_2 T_2^* \rangle} \quad (\text{C.55})$$

where  $\langle T_j T_j^* \rangle$  denotes the intensity transmission through the  $j$ th grating.

These results can be applied to the case of an extended source by integrating equation C.48 over the source distribution along  $y_s$ . A particular case of interest is that of a slit source, in which each point inside the slit acts as its own point source. Denoting the slit width by  $a$ , the intensity term corresponding to the moiré frequency is:

$$H'_1(\lambda) = \frac{1}{a} \int_{-a/2}^{a/2} H_1(\lambda) dy_s = \chi_1 \chi_2^* \exp \left( i \frac{2\pi y}{P_d} \right) \cdot \frac{P_s}{\pi a} \sin \left( \frac{\pi a}{P_s} \right) \quad (\text{C.56})$$

Therefore, assuming two pure phase gratings for which the intensity transmission is 1, the contrast is now:

$$C = \frac{2P_s}{\pi a} \left| \sin \left( \frac{\pi a}{P_s} \right) \right| |\chi_1||\chi_2| \quad (\text{C.57})$$

In a similar argument, the expected contrast for a polychromatic source is obtained from averaging  $H_1$  (equation C.48) over its spectrum. Alternatively, one can average the contrast expression directly but taking into account the phase of  $\chi_1$  and  $\chi_2^*$  (in the case of a slit source, the sine function will have the same value since  $P_s$  does not depend on the wavelength). This is explained by the fact that, for two different wavelengths, these two terms could have a different relative phase, and thus the oscillations from one of the patterns would be shifted with respect to the other.

There are several conclusions that can be extracted from the results obtained in this section, a full discussion of which can be found in ref. [24]. Of special relevance to this project is the extreme case when both gratings are pure phase objects. Then, the moiré fringes appear in the far-field from the second grating, with their period being inversely proportional to the inter-grating distance. The contrast of this fringes is maximized when  $\delta_1 = \delta_2 = 0.5$  [25]. It must be noted that the moiré term is not always the dominant one, specially when using monochromatic beams. For this reason, the actual pattern can vary according to the contribution of other frequency terms (e.g. oscillations at the effective Talbot frequency from the first grating modulated by the moiré sinusoidal). Oddly enough, their effects seem to vanish when using an extended polychromatic source, while the moiré fringes become clearer. However, when using a extended beam its width should be smaller than half the source period. This condition can also be written in terms of the lateral coherence  $l_c$  of the source at the first grating:

$$l_c = \frac{\lambda L_1}{s_w} \geq 2\delta_1 P_1 \quad (\text{C.58})$$

## C.2 Three-grating system

A possible extension for the system discussed previously is to add a third grating, which offers some advantages. Following a similar procedure to the previous section, the pattern at the camera after this modification is obtained. The derivation will be performed without taking into account the assumptions made in the reference, which will only be mentioned briefly at the end.

Since this is just an extension of the case derived previously, the third grating is placed at the former observation plane. Therefore, the field amplitude is given by equation C.25:

$$V_2(y) \propto e^{ikL'} \exp \left( i \frac{k}{2L'} (y_3 - y_s)^2 \right) \sum_{m,n} A_m B_n e^{i\phi_0(m,n) + i\phi_1(m,n)} \quad (\text{C.59})$$

Here the notation has been adapted to the new system, and the cosine has been written again as its approximation to second order.

Also, consider the Fourier Series of the third grating:

$$T_3(y_3) = \sum_q C_q e^{i2\pi q f_3 y_3} \quad (\text{C.60})$$

The field at the observation plane, assuming Fresnel diffraction, is then given by:

$$V(y) \propto \int V_2(y) T_3(y) e^{ikL_3} \exp\left(i \frac{k}{2L_3} (y - y_3)^2\right) dy_3 \quad (\text{C.61})$$

This integral can be solved similarly to the integrals of the two-grating system. Applying the Gaussian integral formula, and ignoring the amplitude constant, the field at the camera results in:

$$\begin{aligned} V(y) &\propto e^{ikL/\cos\theta} \sum_{m,n,q} A_m B_n C_q \\ &\times \exp\left(i \frac{2\pi y}{L} (mf_1 L_1 + nf_2(L_1 + D_1) + qf_3(L_1 + D_1 + D_3))\right) \\ &\times \exp\left(i \frac{2\pi y_s}{L} (mf_1(D_1 + D_3 + L_3) + nf_2(D_2 + L_3) + qf_3 L_3)\right) \\ &\times \exp\left(-i \frac{L'}{2k} \left[ (2\pi m f_1)^2 \frac{L_1}{L'} + (2\pi n f_2)^2 \frac{D_3}{L'} - \left(2\pi m f_1 \frac{L_1}{L'} - 2\pi n f_2 \frac{D_3}{L'}\right)^2 \right]\right) \\ &\times \exp\left(-i \frac{4\pi^2 L_3 L'}{2kL} \left(m f_1 \frac{L_1}{L'} + n f_2 \frac{L_1 + D_1}{L'} + q f_3\right)^2\right) \end{aligned} \quad (\text{C.62})$$

The intensity pattern at the camera is given by the squared modulus of the previous expression. As it occurred for the two-grating system, it takes the form of a summation over all possible values of  $m$ ,  $n$ ,  $q$ ,  $m'$ ,  $n'$  and  $q'$ . From there it can be rewritten as a summation over  $\Delta m = m - m'$ ,  $\Delta n = n - n'$  and  $\Delta q = q - q'$ . Inside each term, the dependence on  $y$  is restricted to a phase, and thus its contribution consists of an oscillation pattern with a unique frequency given by:

$$f_y = \frac{1}{L} [\Delta m f_1 L_1 + \Delta n f_2 (L_1 + D_1) + \Delta q f_3 (L_1 + D_1 + D_3)] \quad (\text{C.63})$$

Of course, each possible frequency (except zero) is represented by two terms corresponding to its positive and negative value, which are defined by the same coefficients  $\Delta m$ ,  $\Delta n$  and  $\Delta q$  but of opposite sign. The moiré fringes now come from  $\Delta m = 1$ ,  $\Delta n = -2$  and  $\Delta q = 1$  (and the opposite). After a lengthy calculation, the intensity can be reduced to:

$$H_1 = \exp\left(i \frac{2\pi y}{P_d} + i \frac{2\pi y_s}{P_s}\right) \chi_1^* \chi_2' \chi_3^* \quad (\text{C.64})$$

On the one hand, the exponential at the front shows the expected cyclic dependence on both  $y$  and  $y_s$ , with the period of the fringes and the source period being, respectively,

$$P_d = \frac{L}{f_1 L_1 - 2f_2(L_1 + D_1) + f_3(L_1 + D_1 + D_3)} \quad (\text{C.65})$$

$$P_s = \frac{L}{f_1(D_1 + D_3 + L_3) - 2f_2(D_3 + L_3) + f_3 L_3} \quad (\text{C.66})$$

On the other hand, the coefficients  $\chi_j$  are defined as follows:

$$\chi_1^* = \sum_m A_{m+1} A_m^* e^{-i2\pi(m+1/2)\delta_1} \quad (\text{C.67})$$

$$\chi'_2 = \sum_n B_{n-2} B_n^* e^{-i2\pi(n-1)\delta_2} \quad (\text{C.68})$$

$$\chi_3^* = \sum_q C_{q+1} C_q^* e^{-i2\pi(q+1/2)\delta_3} \quad (\text{C.69})$$

Notice that the summation for the first and third gratings denote the complex conjugate of the ambiguity functions of the corresponding grating. However, the definition for the second grating is only given for convenience and it is not directly its ambiguity function (hence the prime symbol). Furthermore, the autocorrelation distances are:

$$\delta_1 = \frac{\lambda}{L} f_1 [f_1 L_1 (D_1 + D_3 + L_3) - 2f_2 L_1 (D_3 + L_3) + f_3 L_1 L_3] \quad (\text{C.70})$$

$$\delta_2 = \frac{\lambda}{L} f_2 [f_1 L_1 (D_3 + L_3) - 2f_2 (L_1 + D_1)(D_3 + L_3) + f_3 (L_1 + D_1)L_3] \quad (\text{C.71})$$

$$\delta_3 = \frac{\lambda}{L} f_3 [f_1 L_1 L_3 - 2f_2 (L_1 + D_1)L_3 + f_3 (L_1 + D_1 + D_3)L_3] \quad (\text{C.72})$$

A closed expression of the contrast can be obtained from  $H_1$  in the same way it was obtained in the two-grating system:

$$C = 2 \frac{|H_1|}{|H_0|} = 2 \frac{|\chi_1|}{\langle T_1 T_1^* \rangle} \frac{|\chi'_2|}{\langle T_2 T_2^* \rangle} \frac{|\chi_3|}{\langle T_3 T_3^* \rangle} \quad (\text{C.73})$$

If the second grating is a  $\pi$ -phase grating, hence its zeroth order is suppressed, and the gratings are far enough from one another (so that only the  $\pm 1$  orders play an important role in the field at the third plane), the formula above is reduced

$$C = 2 \frac{|H_1|}{|H_0|} = 2 \frac{|\chi_1|}{\langle T_1 T_1^* \rangle} |B_1| |B_{-1}| \frac{|\chi_3|}{\langle T_3 T_3^* \rangle} \quad (\text{C.74})$$

which is the expression given in ref. [24].

Several consequences can be extracted from this formulae by mere comparison with the two-grating case. For an extended or polychromatic sources one should simply average  $H_1$  (or the contrast, but accounting for the relative phase between the terms) over the proper distribution. In that case, the coherence conditions when the first grating is a pure phase one remains the same (eq. C.58). Moreover, the fact that the given expressions only take into account the contribution of the moiré frequency to the intensity also make it possible (and actually more likely) that other frequency terms play an important role in the actual intensity pattern.

The most significant difference from the two-grating system is that the period of the fringes is now proportional to the difference between the integrating distances ( $D_3 - D_1$ ), and so the gratings can be separated without affecting the fringe contrast. As a result, while two-grating interferometers are limited to small grating separations due to the minimum period resolvable by cameras, the three-grating design allows for larger interferometers that are much more useful for a variety of practical applications.

Finally, even though the approximation has been used in literature [24, 26], it is unclear under what conditions it is valid. From the experiments in the references and the results in this paper (section 5.4.2) it seems to hold when the source is polychromatic, but not for the monochromatic case (even if an incoherent source is considered). This is a sensible issue because the results can change drastically. Furthermore, if it is true the contrast is maximized when both  $\delta_1$  and  $\delta_3$  are closer to 0.5.

# Appendix D

## Schrödinger Equation for a linear potential

In this section a full derivation of the solution to Schrödinger's equation is provided for the case of a single particle that travels under the action of a linear potential. This development is taken from ref. [64].

Consider a potential that depends linearly in the transversal coordinate  $x$ :

$$V(x) = Fx \quad (\text{D.1})$$

with  $F$  a constant. Following the arguments presented in section 5.1 of the main document, Schrödinger's Equation can be reduced to:

$$i\hbar \frac{\partial \Psi(x, t)}{\partial t} = \left( \frac{\hat{p}^2}{2m} + F\hat{x} \right) \Psi(x, t) \quad (\text{D.2})$$

where  $m$  is the mass of the particle,  $\hbar$  is the reduced Planck constant, and  $\hat{x}$  and  $\hat{p} = -i\hbar \frac{\partial}{\partial x}$  are the position and momentum operators satisfying the canonical commutation relation

$$[\hat{x}, \hat{p}] = i\hbar \quad (\text{D.3})$$

The formal solution to this equation can be found by simply integrating over time:

$$\Psi(x, t) = \exp \left( -i \frac{t}{\hbar} \left[ \frac{\hat{p}^2}{2m} + F\hat{x} \right] \right) \Psi(x, 0) \quad (\text{D.4})$$

Now, since the  $\hat{p}$  and  $\hat{x}$  operators do not commute, further expansion of the exponential must be done according to the Zassenhaus formula:

$$e^{\lambda(\hat{X}+\hat{Y})} = e^{\lambda\hat{X}} e^{\lambda\hat{Y}} e^{\lambda^2 C_2(\hat{X}, \hat{Y})} e^{\lambda^3 C_3(\hat{X}, \hat{Y})} e^{\lambda^4 C_4(\hat{X}, \hat{Y})} \dots \quad (\text{D.5})$$

with  $\hat{X}$  and  $\hat{Y}$  two operators, and  $\lambda$  a scalar. The coefficients  $C_j$  are given by

$$C_2(\hat{X}, \hat{Y}) = -\frac{1}{2}[\hat{X}, \hat{Y}] \quad (\text{D.6})$$

$$C_3(\hat{X}, \hat{Y}) = \frac{1}{3}[\hat{Y}, [\hat{X}, \hat{Y}]] + \frac{1}{6}[\hat{X}, [\hat{X}, \hat{Y}]] \quad (\text{D.7})$$

$$C_4(\hat{X}, \hat{Y}) = -\frac{1}{8}([\hat{Y}, [\hat{Y}, [\hat{X}, \hat{Y}]]] + [\hat{Y}, [\hat{X}, [\hat{X}, \hat{Y}]]]) - \frac{1}{24}[\hat{X}, [\hat{X}, [\hat{X}, \hat{Y}]]] \quad (\text{D.8})$$

and so on. In the present case it is convenient to choose  $\lambda = -it/\hbar$ ,  $\hat{X} = F\hat{x}$  and  $\hat{Y} = \hat{p}^2/2m$ . Then, the first commutators are given by

$$[\hat{X}, \hat{Y}] = i\frac{F\hbar}{m}\hat{p} \quad (\text{D.9})$$

$$[\hat{Y}, [\hat{X}, \hat{Y}]] = 0 \quad (\text{D.10})$$

$$[\hat{X}, [\hat{X}, \hat{Y}]] = -\frac{F^2\hbar^2}{m} \quad (\text{D.11})$$

The remaining commutators are zero, and therefore  $C_4$  and all subsequent coefficients are also null. Applying the Zassenhaus formula, equation D.4 can be written as:

$$\Psi(x, t) = \exp\left(-i\frac{Ft}{\hbar}\hat{x}\right) \exp\left(-i\frac{t}{2\hbar m}\hat{p}^2\right) \exp\left(i\frac{Ft^2}{2\hbar m}\hat{p}\right) \exp\left(i\frac{F^2t^3}{6\hbar m}\right) \Psi(x, 0) \quad (\text{D.12})$$

Notice that the last term is a scalar, and so it can be moved in front of the expression. The second-to-last term is actually a translation operator, and thus satisfies

$$\exp\left(i\frac{Ft^2}{2\hbar m}\hat{p}\right) \Psi(x, 0) = \Psi\left(x + \frac{Ft^2}{2m}, 0\right) \quad (\text{D.13})$$

This is a well-known fact in quantum mechanics and it is easily proven, for instance, by considering the Taylor expansion of the exponential of an operator. According to the reference, the following also holds:

$$\exp\left(-i\frac{t}{2\hbar m}\hat{p}^2\right) \Psi(x, 0) = \Psi\left(\hat{x} - \frac{t}{m}\hat{p}, 0\right) 1 \quad (\text{D.14})$$

Applying both relations,

$$\Psi(x, t) = \exp\left(i\frac{F^2t^3}{6\hbar m}\right) \exp\left(-i\frac{Ft}{\hbar}\hat{x}\right) \Psi\left(\hat{x} + \frac{Ft^2}{2m} - \frac{t}{m}\hat{p}, 0\right) 1 \quad (\text{D.15})$$

Now, one can assume that the initial condition accepts a Fourier Transform. This means that it can be written as:

$$\Psi(x, 0) = \int_{-\infty}^{\infty} d\nu Y(\nu) \exp(i2\pi\nu x) \quad (\text{D.16})$$

Substituting in the previous expression,

$$\Psi(x, t) = \exp\left(i\frac{F^2t^3}{6\hbar m}\right) \exp\left(-i\frac{Ft}{\hbar}\hat{x}\right) \int_{-\infty}^{\infty} d\nu Y(\nu) \exp\left[i2\pi\nu\left(\hat{x} + \frac{Ft^2}{2m} - \frac{t}{m}\hat{p}\right)\right] 1$$

Notice that the second term in the exponential is a scalar, and thus can be written in its own exponential. As for the first and third term, they have non-commuting operators, so the Zassenhaus formula must be applied. Choosing  $\lambda = i2\pi\nu$ ,  $\hat{X} = \hat{x}$  and  $\hat{Y} = -tp/m$ , one gets that

$$e^{i2\pi\nu(\hat{x} - \frac{t}{m}\hat{p})} 1 = e^{i2\pi\nu\hat{x}} e^{-i2\pi\nu\frac{t}{m}\hat{p}} e^{-i2\pi^2\nu^2\frac{\hbar t}{m}} 1 = e^{i2\pi\nu\hat{x}} e^{-i2\pi^2\nu^2\frac{\hbar t}{m}} 1 \quad (\text{D.17})$$

where it has been used that the last term is a scalar and so it commutes with the momentum exponential. Then, the momentum term can be removed since  $\exp(\alpha\hat{p})1 = 1$  [70]. This leads to the final solution:

$$\Psi(x, t) = \exp\left(i\frac{F^2t^3}{6\hbar m}\right) \exp\left(-i\frac{Ft}{\hbar}x\right) \int_{-\infty}^{\infty} d\nu Y(\nu) \exp\left[i2\pi\nu\left(x + \frac{Ft^2}{2m} - \frac{\pi\hbar t}{m}\nu\right)\right] \quad (\text{D.18})$$

where

$$Y(\nu) = \int_{-\infty}^{\infty} dx' \Psi(x', 0) \exp(-i2\pi\nu x') \quad (\text{D.19})$$

is the Fourier Transform of the initial wavefunction. An important detail of this result is that the integral actually corresponds to the convolution of the initial condition with a certain function. To make the convolution more explicit, one can perform the integral over  $\nu$ , which gives

$$\begin{aligned} \Psi(x, t) &= \exp\left(i\frac{F^2t^3}{6\hbar m}\right) \exp\left(-i\frac{Ft}{\hbar}x\right) \sqrt{\frac{m}{i2\pi\hbar t}} \\ &\times \int_{-\infty}^{\infty} \Psi(x', 0) \exp\left[i\frac{m}{2\hbar t}\left(x - x' + \frac{Ft^2}{2m}\right)^2\right] dx' \end{aligned} \quad (\text{D.20})$$

As a last note, the first term in this expression is a constant phase, and therefore it can be safely ignored for most practical purposes.

# References

- [1] Helmut Rauch and Samuel A Werner. *Neutron Interferometry: Lessons in Experimental Quantum Mechanics, Wave-Particle Duality, and Entanglement*, volume 12. Oxford University Press, USA, 2015.
- [2] Alexander D Cronin, Jörg Schmiedmayer, and David E Pritchard. Optics and interferometry with atoms and molecules. *Reviews of Modern Physics*, 81(3):1051, 2009.
- [3] H Maier-Leibnitz and T Springer. Ein interferometer für langsame neutronen. *Zeitschrift für Physik*, 167(4):386–402, 1962.
- [4] Helmut Rauch, Wolfgang Treimer, and Ulrich Bonse. Test of a single crystal neutron interferometer. *Physics Letters A*, 47(5):369–371, 1974.
- [5] Helmut Rauch, Anton Zeilinger, Gerald Badurek, A Wilfing, W Bauspiess, and U Bonse. Verification of coherent spinor rotation of fermions. *Physics Letters A*, 54(6):425–427, 1975.
- [6] SA Werner, H Kaiser, M Arif, and R Clothier. Neutron interference induced by gravity: new results and interpretations. *Physica B + C*, 151(1-2):22–35, 1988.
- [7] Charles W Clark, Roman Barankov, Michael G Huber, Muhammad Arif, David G Cory, and Dmitry A Pushin. Controlling neutron orbital angular momentum. *Nature*, 525(7570):504–506, 2015.
- [8] Ke Li, Muhammad Arif, David G Cory, Robert Haun, Benjamin Heacock, Michael G Huber, Joachim Nsofini, Dmitry A Pushin, Parminder Sagg, Dusan Sarenac, et al. Neutron limit on the strongly-coupled chameleon field. *Physical Review D*, 93(6):062001, 2016.
- [9] Dusan Sarenac, Michael G Huber, Benjamin Heacock, Muhammad Arif, Charles W Clark, David G Cory, Chandra B Shahi, and Dmitry A Pushin. Holography with a neutron interferometer. *Optics express*, 24(20):22528–22535, 2016.
- [10] Tobias Denkmayr, Hermann Geppert, Stephan Sponar, Hartmut Lemmel, Alexandre Matzkin, Jeff Tollaksen, and Yuji Hasegawa. Observation of a quantum cheshire cat in a matter-wave interferometer experiment. *Nature communications*, 5(1):1–7, 2014.
- [11] Muhammad Arif, Dennis Eugene Brown, Geoffrey L Greene, R Clothier, and K Littrell. Multistage position-stabilized vibration isolation system for neutron interferometry. In *Vibration Monitoring and Control*, volume 2264, pages 20–26. International Society for Optics and Photonics, 1994.

- [12] Parminder Saggi, Taisiya Mineeva, Muhammad Arif, David G Cory, Robert Haun, Ben Heacock, Michael G Huber, Ke Li, Joachim Nsofini, Dusan Sarenac, et al. Decoupling of a neutron interferometer from temperature gradients. *Review of Scientific Instruments*, 87(12):123507, 2016.
- [13] Dmitry A Pushin, Michael G Huber, Muhammad Arif, Chandra B Shahi, Joachim Nsofini, Christopher J Wood, Dusan Sarenac, and David G Cory. Neutron interferometry at the national institute of standards and technology. *Advances in High Energy Physics*, 2015, 2015.
- [14] CB Shahi, M Arif, DG Cory, T Mineeva, J Nsofini, D Sarenac, CJ Williams, MG Huber, and DA Pushin. A new polarized neutron interferometry facility at the ncnr. *Nuclear Instruments and Methods in Physics Research Section A: Accelerators, Spectrometers, Detectors and Associated Equipment*, 813:111–122, 2016.
- [15] M Zawisky, J Springer, R Farthofer, and U Kuetgens. A large-area perfect crystal neutron interferometer optimized for coherent beam-deflection experiments: Preparation and performance. *Nuclear Instruments and Methods in Physics Research Section A: Accelerators, Spectrometers, Detectors and Associated Equipment*, 612(2):338–344, 2010.
- [16] AI Ioffe, VS Zabiyakin, and GM Drabkin. Test of a diffraction grating neutron interferometer. *Physics Letters A*, 111(7):373–375, 1985.
- [17] Manfred Gruber, Kurt Eder, Anton Zeilinger, Roland Gähler, and Walter Mampe. A phase-grating interferometer for very cold neutrons. *Physics Letters A*, 140(7-8):363–367, 1989.
- [18] G Van der Zouw, M Weber, J Felber, R Gähler, P Geltenbort, and A Zeilinger. Aharonov–Bohm and gravity experiments with the very-cold-neutron interferometer. *Nuclear Instruments and Methods in Physics Research Section A: Accelerators, Spectrometers, Detectors and Associated Equipment*, 440(3):568–574, 2000.
- [19] Uwe Schellhorn, Romano A Rupp, Stefan Breer, and Roland P May. The first neutron interferometer built of holographic gratings. *Physica B: Condensed Matter*, 234:1068–1070, 1997.
- [20] J Klepp, Christian Pruner, Y Tomita, C Plonka-Spehr, P Geltenbort, S Ivanov, G Manzin, KH Andersen, J Kohlbrecher, MA Ellabban, et al. Diffraction of slow neutrons by holographic SiO<sub>2</sub> nanoparticle-polymer composite gratings. *Physical Review A*, 84(1):013621, 2011.
- [21] Henry Fox Talbot. Lxxvi. facts relating to optical science. no. iv. *The London, Edinburgh, and Dublin Philosophical Magazine and Journal of Science*, 9(56):401–407, 1836.
- [22] John F Clauser and Shifang Li. Talbot-vonLau atom interferometry with cold slow potassium. *Physical Review A*, 49(4):R2213, 1994.
- [23] F Pfeiffer, C Grünzweig, O Bunk, G Frei, E Lehmann, and C David. Neutron phase imaging and tomography. *Physical review letters*, 96(21):215505, 2006.
- [24] Houxun Miao, Alireza Panna, Andrew A Gomella, Eric E Bennett, Sami Znati, Lei Chen, and Han Wen. A universal moiré effect and application in X-ray phase-contrast imaging. *Nature physics*, 12(9):830–834, 2016.

- [25] Dmitry A Pushin, Dusan Sarenac, Daniel S Hussey, Haixing Miao, Muhammad Arif, David G Cory, Michael G Huber, David L Jacobson, Jacob M LaManna, Joseph D Parker, et al. Far-field interference of a neutron white beam and the applications to noninvasive phase-contrast imaging. *Physical Review A*, 95(4):043637, 2017.
- [26] Dusan Sarenac, Dmitry A Pushin, Michael G Huber, Daniel S Hussey, Haixing Miao, Muhammad Arif, David G Cory, Alexander D Cronin, Benjamin Heacock, David L Jacobson, et al. Three phase-grating moiré neutron interferometer for large interferometer area applications. *Physical review letters*, 120(11):113201, 2018.
- [27] Joseph W Goodman. *Introduction to Fourier optics*. Roberts and Company Publishers, 2005.
- [28] Adrián Carbajal-Domínguez, Jorge Bernal Arroyo, Jesus E Gomez Correa, and Gabriel Martínez Niconoff. Numerical calculation of near field scalar diffraction using angular spectrum of plane waves theory and FFT. *Revista mexicana de física E*, 56(2):159–164, 2010.
- [29] Fabin Shen and Anbo Wang. Fast-Fourier-transform based numerical integration method for the Rayleigh-Sommerfeld diffraction formula. *Applied optics*, 45(6):1102–1110, 2006.
- [30] Éamon Lalor. Conditions for the validity of the angular spectrum of plane waves. *JOSA*, 58(9):1235–1237, 1968.
- [31] Hermann Weyl. Ausbreitung elektromagnetischer wellen über einem ebenen leiter. *Annalen der Physik*, 365(21):481–500, 1919.
- [32] Jason Schmidt. *Numerical simulation of optical wave propagation with examples in MATLAB*. Society of Photo-Optical Instrumentation Engineers, Bellingham, Washington, 2010.
- [33] David Mas, Javier Garcia, Carlos Ferreira, Luis M Bernardo, and Francisco Marinho. Fast algorithms for free-space diffraction patterns calculation. *Optics communications*, 164(4-6):233–245, 1999.
- [34] Junchang Li, Zujie Peng, and Yunchang Fu. Diffraction transfer function and its calculation of classic diffraction formula. *Optics communications*, 280(2):243–248, 2007.
- [35] Kyoji Matsushima and Tomoyoshi Shimobaba. Band-limited angular spectrum method for numerical simulation of free-space propagation in far and near fields. *Optics express*, 17(22):19662–19673, 2009.
- [36] Ji Qiang. A high-order fast method for computing convolution integral with smooth kernel. *Computer Physics Communications*, 181(2):313–316, 2010.
- [37] James W Eastwood and David Richard Kingsmill Brownrigg. Remarks on the solution of Poisson’s equation for isolated systems. *Journal of Computational Physics*, 32(1):24–38, 1979.
- [38] Lord Rayleigh. XXV. On copying diffraction-gratings, and on some phenomena connected therewith. *The London, Edinburgh, and Dublin Philosophical Magazine and Journal of Science*, 11(67):196–205, 1881.

- [39] Jianming Wen, Yong Zhang, and Min Xiao. The Talbot effect: recent advances in classical optics, nonlinear optics, and quantum optics. *Advances in optics and photonics*, 5(1):83–130, 2013.
- [40] Sébastien Berujon. *At-Wavelength Metrology of Hard X-ray Synchrotron Beams and Optics*. PhD thesis, ESRF, Grenoble, France, 2013.
- [41] Ernst Lau. Beugungerscheinungen an doppelrastern. *Annalen der Physik*, 437(7-8):417–423, 1948.
- [42] Jürgen Jahns and Adolf W Lohmann. The Lau effect (a diffraction experiment with incoherent illumination). *Optics communications*, 28(3):263–267, 1979.
- [43] William B Case, Mathias Tomandl, Sarayut Deachapunya, and Markus Arndt. Realization of optical carpets in the Talbot and Talbot-Lau configurations. *Optics Express*, 17(23):20966–20974, 2009.
- [44] Michael Victor Berry and Sz Klein. Integer, fractional and fractal Talbot effects. *Journal of modern optics*, 43(10):2139–2164, 1996.
- [45] GJ Swanson and EN Leith. Analysis of the Lau effect and generalized grating imaging. *JOSA A*, 2(6):789–793, 1985.
- [46] Paul Latimer. Talbot plane patterns: grating images or interference effects? *Applied optics*, 32(7):1078–1083, 1993.
- [47] Thomas J Suleski. Generation of Lohmann images from binary-phase Talbot array illuminators. *Applied optics*, 36(20):4686–4691, 1997.
- [48] Krzysztof Patorski. I The self-imaging phenomenon and its applications. *Progress in optics*, 27:1–108, 1989.
- [49] Martin Engelhardt, Christian Kottler, Oliver Bunk, Christian David, C Schroer, Joachim Baumann, Manfred Schuster, and Franz Pfeiffer. The fractional Talbot effect in differential x-ray phase-contrast imaging for extended and polychromatic x-ray sources. *Journal of microscopy*, 232(1):145–157, 2008.
- [50] S Yokozeki and T Suzuki. Shearing interferometer using the grating as the beam splitter. *Applied Optics*, 10(7):1575–1580, 1971.
- [51] Adolf W Lohmann and DE Silva. An interferometer based on the talbot effect. *Optics Communications*, 2(9):413–415, 1971.
- [52] Jorge Ibarra and Jorge Ojeda-Castañeda. Talbot interferometry: a new geometry. *Optics communications*, 96(4-6):294–301, 1993.
- [53] Franz Pfeiffer, Timm Weitkamp, Oliver Bunk, and Christian David. Phase retrieval and differential phase-contrast imaging with low-brilliance x-ray sources. *Nature physics*, 2(4):258–261, 2006.
- [54] Rainer Storn and Kenneth Price. Differential evolution – a simple and efficient heuristic for global optimization over continuous spaces. *Journal of global optimization*, 11(4):341–359, 1997.
- [55] Timm Weitkamp, Ana Diaz, Christian David, Franz Pfeiffer, Marco Stampanoni, Peter Cloetens, and Eric Ziegler. X-ray phase imaging with a grating interferometer. *Optics express*, 13(16):6296–6304, 2005.

- [56] Zhili Wang, Peiping Zhu, Wanxia Huang, Qingxi Yuan, Xiaosong Liu, Kai Zhang, Youli Hong, Huitao Zhang, Xin Ge, Kun Gao, et al. Quantitative coherence analysis with an X-ray Talbot–Lau interferometer. *Analytical and bioanalytical chemistry*, 397(6):2091–2094, 2010.
- [57] Dmitry A Pushin. *Coherent control of neutron interferometry*. PhD thesis, Massachusetts Institute of Technology, 2006.
- [58] Dusan Sarenac. *Structured Beams as Quantum Probes*. PhD thesis, University of Waterloo, 2018.
- [59] Jean-François Schaff, Tim Langen, and Jörg Schmiedmayer. Interferometry with atoms. *La Rivista del Nuovo Cimento*, 37:509–589, 2014.
- [60] Michael S Chapman, Christopher R Ekstrom, Troy D Hammond, Richard A Rubenstein, Jörg Schmiedmayer, Stefan Wehinger, and David E Pritchard. Optics and interferometry with  $\text{Na}_2$  molecules. *Physical review letters*, 74(24):4783, 1995.
- [61] Björn Brezger, Lucia Hackermüller, Stefan Uttenthaler, Julia Petschinka, Markus Arndt, and Anton Zeilinger. Matter-wave interferometer for large molecules. *Physical review letters*, 88(10):100404, 2002.
- [62] Ángel S Sanz. Neutron matter-wave diffraction: A computational perspective. *Advances in Neutron Optics: Fundamentals and Applications in Materials Science and Biomedicine*, 2019.
- [63] R Becerril, FS Guzmán, A Rendón-Romero, and S Valdez-Alvarado. Solving the time-dependent Schrödinger equation using finite difference methods. *Revista mexicana de física E*, 54(2):120–132, 2008.
- [64] Francisco Soto-Eguibar and Héctor M Moya-Cessa. Solution of the Schrödinger equation for a linear potential using the extended baker-campbell-hausdorff formula. *Appl. Math*, 9(1):1–7, 2015.
- [65] Roberto Colella, Albert W Overhauser, and Samuel A Werner. Observation of gravitationally induced quantum interference. *Physical Review Letters*, 34(23):1472, 1975.
- [66] S Szapiel and K Patorski. Fresnel diffraction images of periodic objects under Gaussian beam illumination. *Optica Acta: International Journal of Optics*, 26(4):439–446, 1979.
- [67] Albert Abraham Michelson. *Studies in optics*. Courier Corporation, 1995.
- [68] Francisco Jose Torcal-Milla, Luis Miguel Sanchez-Brea, and Francisco Javier Salgado-Remacha. Self-images location of amplitude/phase binary gratings. *Applied optics*, 48(32):6252–6258, 2009.
- [69] JM Cowley and AF Moodie. Fourier images: I – The point source. *Proceedings of the Physical Society. Section B*, 70(5):486, 1957.
- [70] Héctor Manuel Moya-Cessa and Francisco Soto-Eguibar. *Differential equations: an operational approach*. Rinton Press, Incorporated, 2011.